ON THE BROWNIAN MOTION : FROM CLASSICAL TO QUANTAL

THESIS SUBMITTED FOR THE DEGREE OF DOCTOR OF PHILOSOPHY (SCIENCE) OF THE JADAVPUR UNIVERSITY

MALAY BANDYOPADHYAY

SATYENDRANATH BOSE NATIONAL CENTRE
FOR BASIC SCIENCES
JD BLOCK, SECTOR 3, SALT LAKE CITY
KOLKATA 700 098, INDIA

2007

CERTIFICATE FROM THE SUPERVISOR

This is to certify that the thesis entitled *"On the Brownian motion : From quantal to classical"* submitted by **Malay Bandyopadhyay**, who got his name registered on **June 30, 2004** for the award of **Ph.D. (Science) degree** of **Jadavpur University**, is absolutely based upon his own work under the supervision of **Professor Sushanta Dattagupta** at **Indian Institute of Science Education & Research** and S. N. Bose National Centre for Basic Sciences and that neither this thesis nor any part of it has been submitted for any degree/diploma or any other academic award anywhere before.

PROF. SUSHANTA DATTAGUPTA
PROFESSOR and DIRECTOR,
INDIAN INSTITUTE OF SCIENCE EDUCATION & RESEARCH,
HC-VII, SECTOR-III, SALT LAKE, KOLKATA - 700106,
INDIA.
ON LIEN FROM S. N. BOSE NATIONAL CENTRE FOR BASIC SCIENCES, JD BLOCK, SECTOR-III, KOLKATA-700098. Date :

Acknowledgements

This thesis is the result of about five years of work. In this long journey I have been accompanied and supported by many people. So it is my pleasure to express my sincere gratitude and acknowledgements for all of them.

The person I would like to first thank is my supervisor Prof. Sushanta Dattagupta. His enthusiastic and integral view on research has made a deep impression on my mind. He was always there to listen and give advise. Interactions with him were always so friendly that it gave me ample opportunity to express my ideas. He showed me different ways to approach a research problem and always insisted on staying focussed and working hard. He could not even realize how much I have learned from him. He also gave me enough freedom in choosing own problems and collaborating with other colleagues which helped me to bring out my best. I owe him my sincere gratitude for having shown me this way of research. Besides being an excellent supervisor, he is as close as a relative. He is a neverending source of inspiration. I am really glad that I have come to know him in my life.

I would like to thank Dr. Surajit Sengupta for an active collaboration on "Polydispersity linked memory effect in nanoparticles". Valuable discussions with him helped me to expand my area of research. I would also like to express my sincere gratitude to Prof. Binayak Dutta-Roy for his continuous encouragement during this period. I have learned a lot from him. Valuable discussions with him helped me to grow myself as a researcher. It is a great pleasure to acknowledge Dr. P. A. Sreeram for his constant help on any computer related problems and valuable scientific discussions. I would like to thank Dr. J. L. Garca-Palacios for his helpful discussions on the numerical solution of Langevin equation and the continued fraction method.

I have enjoyed to work with Suvankar'da on the "Stochastic model of coercivity" and on the "Polydispersity linked memory effect in nanoparticles". The innumerable discussions that I had with Suvankar'da during my Ph.D program helped me to understand diverse aspects of my research problem.

It is really a wonderful experience to work with Jayee on the "Magnetic and caloric properties of nanoparticles" and on the "Phase transions and thermodynamics of 3-D nanoparticles" which have heen discussed in this thesis. I express my heartiest thanks to her for her neverending help on any problem and becoming a very good friend. During this period, I have enjoyed all the scientific and nonscientific discussions with her.

Life is always a tough task without good friends. During these five years I have been accompanied by such good friends : Mukulda, Suman, Brinta, Monodeepda, and Soumen.

I express my sincere thanks to all of them for standing beside me all the time. It is my pleasure to thank Dulal'da for his patience over the year.

Financial support from the Council of Scientific and Industrial Reasearch (CSIR), India is gratefully acknowledged.

Last but not the least, I thank my family : my parents, sisters, brothers-in-laws for the unconditional support and constant encouragements to pursue my Ph. D degree and my Nephews and Niece (Tanu, Mithu, Subho and Mouli) for all the sweet memories that I have shared with them.

List of Publications

Publications in refereed journals :

1. S. Chakraverty, **M. Bandyopadhyay**, S. Dattagupta, A. Frydman, S. Sengupta, and P. A. Sreeram.
   Memory in a magnetic nanoparticle system: Polydispersity and interaction effects.
   Phys. Rev. B 71, 054401, (2005)

2. **Malay Bandyopadhyay** and Sushanta Dattagupta.
   Dissipative Diamagnetism – A Case Study for Equilibrium and Nonequilibrium Statistical Mechanics of Mesoscopic Systems.
   Journal of Statistical Physics 123, 1273 (2006)

3. **Malay Bandyopadhyay**, Sushanta Dattagupta and Monamie sanyal.
   Diffusion Enhancement in a Periodic Potential under High-Frequency Space-Dependent Forcing
   Phys. Rev. E 73, 051108 (2006)

4. **Malay Bandyopadhyay** and Sushanta Dattagupta.
   Landau-Drude Diamagnetism: Fluctuation, Dissipation and Decoherence
   Journal of Phys. : Condensed Matter. 18, 10029 (2006).

5. **Malay Bandyopadhyay**
   Dissipative Tunneling in 2 DEG: Effect of Magnetic Field, Impurity and Temperature
   Journal of Statistical Mechanics: Theory and experiment (2006) L03001.

6. **Malay Bandyopadhyay**
   Orbital magnetism of 2DEG in crossed electromagnetic field: Effect of spin-orbit interaction, confined geometries and defects.
   Journal of Statistical Mechanics : Theory and experiment (2006) P10010.

7. **Malay Bandyopadhyay** and Sushanta Dattagupta.
   Memory in nanomagnetic systems: Superparamagnetism versus Spinglass behavior
   Phys. Rev. B *74*, 214410 (2006).

8. **Malay Bandyopadhyay** and Jayee Bhattacharya.
   Magnetic and caloric properties of superparamagnetic particles: An equilibrium study
   Journal of Phys. : Condensed Matter. *18*, 11309 (2006).

9. S. Chakraverty and **M. Bandyopadhyay**
   Coercivity of Nanomagnetic particles - A stochastic model
   Journal of Phys. : Condensed Matter *19*, 216201 (2007).

Preprints:

1. G. E. Ballentine, **Malay Bandyopadhyay**, Sushanta Dattagupta, and M. B. Knickelbein.
   Thermally-Driven Magnetic Oscillations in Cobalt Nanocluster Superspin Glasses.
   Submitted to Science.

2. **Malay Bandyopadhyay**, and Sushanta Dattagupta.
   Effective Hamiltonian for periodically driven quantum systems: A comparative study.
   To be submitted to Pramana

3. **Malay Bandyopadhyay**, and Sushanta Dattagupta.
   High frequency study of type-II superconductors : effective Hamiltonian approach.
   To be submitted to Physica C

4. **Malay Bandyopadhyay**, and Sushanta Dattagupta.
   High frequency study of Schrödinger cat state : effective Hamiltonian approach.
   To be submitted to Phys. Rev. A

5. **Malay Bandyopadhyay**, and Sushanta Dattagupta.
   High frequency study of quantum tunneling : effective Hamiltonian approach.

To be submitted to J. Phys. A

6. **Malay Bandyopadhyay** and Jayee Bhattacharya.
On the thermodynamics and phase transition of three-dimensional magnetic nanoparticles.
To be submitted to Phys. Rev. B.

Contents

1 **INTRODUCTION** **1**

1.1 Einstein's Explanation of the Brownian Movement: 2

1.2 The Langevin Method — Stochastic Differential Equation 3

1.3 Rotational Brownian Motion 4

1.4 Quantum Brownian Motion 5

1.5 Physical Application of the Theory of Brownian Motion 6

1.6 Our Study 7

2 **Magnetic and Caloric Properties of Magnetic Nanoparticles: An Equilibrium Study** **9**

2.1 Introduction 9

2.2 Effective Hamiltonian and Partition Function 11

2.3 Equilibrium Properties 12

2.3.1 Magnetization 12

2.3.2 Linear Susceptibility (χ_0) 14

2.3.3 Nonlinear Susceptibilities (χ_2, χ_4) 16

2.4 Caloric Properties 21

2.5 Summary and Conclusions 25

3 **Memory in a Magnetic Nanoparticle System - Polydispersity and Interaction Effects.** **27**

3.1 Introduction 27

3.2 Relaxation Theory 29

3.3 Polydispersity-linked Memory Effects 33

3.4 Summary and Conclusions 39

4 **Memory in Nanomagnetic Systems: Superparamagnetism Versus Spinglass Behavior** **40**

4.1 Introduction 40

4.2 Superparamagnetic Slow Dynamics 43

4.3 Spinglass Like Slow Dynamics 50
4.4 Superparamagnetism versus spinglass 52
4.5 Conclusions 54

5 **Coercivity of Magnetic Nanoparticles: A Stochastic Model.** **55**
5.1 Introduction 55
5.2 Single-domain Regime and Size Dependent Magnetic Properties 57
5.3 Effect of Anisotropic Potential 65
5.3.1 Weak Anisotropy 66
5.3.2 Strong Anisotropy 68
5.4 Multi-domain Regime 70
5.5 Summary and Conclusions 73

6 **Diffusion Enhancement in a Periodic Potential Under High-frequency Space-dependent Forcing** **76**
6.1 Introduction 76
6.2 Model 77
6.3 Effective Potential 79
6.3.1 First Order Correction 79
6.3.2 Second Order Correction 81
6.4 Numerical Scheme and Results 84
6.5 Summary and Conclusions 88

7 **Dissipative Diamagnetism : Gibbs Approach to Equilibrium Statistical Mechanics.** **91**
7.1 Introduction 91
7.2 Model, Formalism and Effective Action 92
7.3 Free Energy and Magnetization. 96
7.4 Equilibrium Position Autocorrelation Function 99
7.5 Summary and Conclusion 101

8 **Landau-Drude Diamagnetism: Fluctuation, Dissipation and Decoherence.** **104**

8.1 Introduction 104
8.2 Model, Quantum Langevin Equation and Einstein Approach 106
8.3 Generalized Susceptibility Tensor 107
8.4 Fluctuation - Dissipation Relationship & Equivalence of Einstein and Gibbs Approaches. 111
8.5 Coherence - Decoherence Transition 114
8.6 Summary and Conclusions 119

9 **Summary** **121**

List of Figures

2.1 Coordinate system showing the unit vectors $\hat{e}, \hat{b}$ and $\hat{n}$ along with the referred angles. 11

2.2 (a)Magnetization versus field curves corresponding to different temperatures for the isotropic case (red), for the Ising case (green) and for the plane-rotator case (blue); (b)Magnetization versus longitudinal field showing the non-$\frac{B}{T}$ superposition of the magnetization curves. 14

2.3 Polar plot of χ_0 versus γ for different values of σ (a) easy-axis anisotropy (b) easy-plane anisotropy. 15

2.4 (a)Plot of linear susceptibility versus σ in the longitudinal (red) and transverse (green) field cases; (b) log-log plot of χ_0 versus $\frac{1}{\sigma}$ for the isotropic case (red), Ising case (green), plane-rotator case (blue) and the randomly distributed anisotropy case (pink). 15

2.5 (a) Longitudinal and (b) transverse components of the linear susceptibility versus $1/\sigma$ with $h = 0.006$ (red), $h = 0.011$ (green) and $h = 0.016$ (blue) and these curves exhibit spinglass like maximum. 16

2.6 Polar plot of χ_2 versus γ for different values of σ (a) easy-axis anisotropy (b) easy-plane anisotropy. 17

2.7 Polar plot of χ_4 versus γ for different values of σ for the easy-axis anisotropy. 18

2.8 Polar plot of χ_4 versus γ for different values of σ for the easy-plane anisotropy. 19

2.9 (a) Plot of χ_2 versus σ in the longitudinal (red), transverse (green) field and random distribution (blue) cases; (b) log-log plot of χ_2 versus $\frac{1}{\sigma}$ for the isotropic case (red), Ising case (green), plane-rotator case (blue) and the randomly distributed anisotropy case (pink). 20

2.10 (a)Plot of χ_4 versus σ in the longitudinal (blue), transverse (black) field and random distribution (red) cases; (b)Log-log plot of χ_4 versus $\frac{1}{\sigma}$ for the isotropic case (blue), Ising case (black), plane-rotator case (red) and the randomly distributed anisotropy case (green) 21

2.11 Inverse temperature dependence of (a) u, (b) S, and (c) specific heat for the isotropic case. 22

2.12 Temperature dependence of (a) u, (b) S, and (c) specific heat for the zero field case. 22

2.13 Inverse temperature dependence of (a) u, (b) S, (c) Specific heat for the Ising case. 23

2.14 Inverse temperature dependence of (a) u, (b) S, and (c) specific heat for the plane-rotator case. 24

2.15 Temperature dependence of (a) u, (b) S and (c) specific heat for the longitudinal field case. 25

3.1 Room temperature dc M-H measurement of interacting sample A and non-interacting sample B. The solid lines are drawn through the experimental points, indicated by dots. 30

3.2 Experimental M(T) curves during cooling (∘ red) in a small magnetic field $h = 50$ Oe and zero-field heating (□ black) for the (a) interacting and (b) non-interacting samples showing prominent memory effects. A constant heating/cooling rate of 2K/min was maintained except at 60K, 40K and 20K where the cooling was arrested for 4 h duration at each temperature during which time h was switched off. 34

3.3 Simulated M (arbitrary unit) vs. T curves during cooling (solid black) and heating (dashed red) for the (a) interacting and (b) non-interacting cases: The curve (c) shows the various contributions to the total magnetization of interacting sample(A) coming from the (i) fast particles during the cooling cycle (black solid line), (ii) fast particles during the heating cycle (red filled circle), (iii) slow particles during the cooling cycle (magenta dashed line) and (iv) slow particles during the heating cycle (blue square). The theoretical curves (a) - (c) have been calculated using a double delta function distribution of particle sizes. Curve (d) shows a plot of the recovery parameter R (see text) as a function of the width(s) of a Gaussian particle size distribution. 36

3.4 Coercivity(h_c) as a function of temperature for the interacting (□ red) and non-interacting (◇ black) samples. The corresponding curves (h_c in arbitrary unit) obtained from our theory assuming a double delta function particle size distribution is shown in the inset. 38

4.1 Numerically calculated dc magnetization for the FC and ZFC processes. . . 44
4.2 Numerically calculated M Versus H curve below and above T_b. 45
4.3 Numerically simulated memory effect observed in dc magnetization curves. 46
4.4 (a) Numerically simulated ZFC relaxation curves with temporary cooling and field change; (b) the same data vs the total time spent at 30 K on a logarithmic scale. 47
4.5 (a) Numerically simulated FC relaxation curves with temporary cooling and field change; (b) the same data vs the total time spent at 30 K on a logarithmic scale. 48
4.6 Numerically simulated FC and ZFC relaxation curves with temporary heating. 49
4.7 (a) Numerically simulated results for the double memory experiment (DME) for the FC method; (b) the FCM and ZFCM vs. temperature of the interacting system are shown. 50
4.8 Numerically simulated results for the double memory experiment (DME) for the ZFC method in an interacting system (green circle) and in a non-interacting system (blue square). 51

5.1 Dependence of coercive field on the particle size of $Co_{80}Ni_{20}$ at two different temperatures (solid curves are just a guide to the eye). The inset shows the linear dependence of the coercive field on the inverse of the average particle size. C. Luna *et al*, Nanotechnology *14*, 268 (2003). 56
5.2 Coordinate system used for our calculation in the Section 5.2. 58
5.3 Variation of the potential function with polar angle θ for different values of λ. The angle ϕ is fixed at zero. 59
5.4 Simulated M versus H curve for two particle sizes (a) 7 nm and (b)18.5 nm respectively. 62
5.5 Dependence of coercive force on the particle diameter for the $Co_{80}Ni_{20}$ nanoparticles at room temperature (300K) for the single domain regime. Red filled dot denotes the experimental data (C. Luna et al [78]) and the blue filled square denotes the simulation data obtained from our model. . . 62
5.6 Dependence of coercive force on the particle diameter for the $Co_{80}Ni_{20}$ nanoparticles at $10K$. Red filled dot denotes the experimental data (C. Luna et al [78]) and the blue filled square denotes the simulation data obtained from our model. 63

5.7 Dependence of saturation magnetization (M_s) on the particle diameter for the $Co_{80}Ni_{20}$ nanoparticles at (a) $10K$ and (b) $300K$. Red filled dot denotes the experimental data (C. Luna et al [78]) and the blue filled square denotes the simulation data obtained from our model. 64

5.8 Dependence of the ratio of remanence to saturation magnetization ($\frac{M_r}{M_s}$) on the particle diameter for the $Co_{80}Ni_{20}$ nanoparticles at $10K$ and $300K$. Red filled dot solid line denotes the experimental data (C. Luna et al [78]) and the blue filled square solid line denotes the simulation data obtained from our model at $10K$. Black filled upward triangles dashed line denote the experimental data (C. Luna et al [78]) and green filled downward triangles dashed line denote the simulation data obtained from our model at $300K$. . 64

5.9 Coordinate system used for our calculation in the Section 5.3. 66

5.10 (a) Variation of magnetization with longitudinal field $\xi = \frac{mB}{k_BT}$ for different cases with easy axis anisotropy (b) Variation of anisotropy-induced contribution with longitudinal field for the same. 68

5.11 (a) Variation of magnetization with longitudinal field $\xi = \frac{mB}{k_BT}$ for different cases with easy plane anisotropy (b) Variation of anisotropy-induced contribution with longitudinal field for the same. 69

5.12 Variation of magnetization with longitudinal field $\xi = \frac{mB}{k_BT}$ for different values of σ (a) Weak-anisotropy case (b) Strong-anisotropy case. 70

5.13 Spin distribution near 180^o domain wall (a) in real space (b) in probability space. 71

6.1 The periodic potential V(x). 83

6.2 The effective potential $V_{eff}(x)$ when external force is space independent. . 84

6.3 The effective potential $V_{eff}(x)$ when external force is space dependent. . . 84

6.4 The effective diffusion coefficient for original and effective dynamics for two cases (a) space dependent (b) space independent external periodic force. The parameters which we use for this numerical calculation are $b = 0.1, \omega = 5.0, D_0 = 0.025, m = 1.0$ and $\gamma = 0.1$. 85

6.5 The current J of the inertial rocked Brownian motor when external force is space dependent. The parameters which we use for this numerical calculation are $b = 0.1, \omega = 5.0, D_0 = 0.025, m = 1.0$ and $\gamma = 0.1$. 87

6.6 The current J of the inertial rocked Brownian motor when external force is space independent. The parameters which we use for this numerical calculation are $b = 0.1, \omega = 5.0, D_0 = 0.025, m = 1.0$ and $\gamma = 0.1$. 88

7.1 Plot of $\frac{2k_BT}{B}\left(\frac{Mc}{e\hbar}\right)^2 \mathcal{M}_z$ versus the damping parameter ζ for the both ohmic ($\mathrm{J}(\omega) \sim \omega$) and nonohmic ($\mathrm{J}(\omega) \sim \omega^3$) cases. 98

7.2 Plot of equilibrium position dispersion $< x^2 >$ in unit of $\frac{\hbar^2}{4Mk_BT}$ for both ohmic ($\mathrm{J}(\omega) \sim \omega$) and nonohmic ($\mathrm{J}(\omega) \sim \omega^3$) dissipation cases. 99

7.3 The analytic continuation of the imaginary time correlation function to real times by using the contours depicted in (a) and (b) to obtain Eq. (7.34). . 101

8.1 The imaginary part of susceptibility χ_{xx} (a) ohmic dissipation case ($J(\omega) \sim \omega$) for two ω_c values. (b) ohmic dissipation case for two γ values. (c) Non-ohmic dissipation case ($J(\omega) \sim \omega^3$) for two ω_c values. (d) Non-ohmic dissipation case for two γ values. 110

8.2 The real part of susceptibility χ_{xx} (a) ohmic dissipation case ($J(\omega) \sim \omega$) for two ω_c values. (b) ohmic dissipation case for two γ values. (c) Non-ohmic dissipation case ($J(\omega) \sim \omega^3$) for two ω_c values. (d) Non-ohmic dissipation case for two γ values. 111

8.3 Spectral function $S_{osc}(\omega)$ vs. ω with Ohmic dissipation for dissipative Landau diamagnetism for different parameter values. 115

8.4 Spectral function $S_{osc}(\omega)$ vs. ω with Ohmic dissipation for a damped harmonic oscillator for different parameter values. 116

Chapter 1

INTRODUCTION

The theory of Brownian motion is one of the simplest models to treat the dynamics of non-equilibrium systems. The botanist Robert Brown gave the first detailed account of Brownian motion in 1827. He examined aqueous suspensions of pollen grains of several species and found that in all cases the pollen grains were in *rapid zigzag motion*. Initially, he thought that the movement was not "vital", but peculiar to the male sexual cells of plants. Brown investigated whether the motion was limited to organic bodies. He finally described the motion as [1]:
"Matter is composed of small particles (*active molecules*) which exhibit a rapid irregular motion having its origin in the particles themselves and not in the surrounding fluid".
According to Nelson [1], the first investigator to express a notion close to the modern theory of Brownian motion was Guoy. We mention the very detailed experimental investigation made by Gouy in the following seven points

- The motion is very irregular, composed of translations and rotations, and the trajectory appears to have no tangent.
- Two particles appear to move independently, even when they approach one another to within a distance less than their diameter.
- The smaller the particles, the more active the motion.
- The composition and density of the particles have no effect.
- The less viscous the fluid, the more active the motion.

- The higher the temperature, the more active the motion.
- The motion never ceases.

An early attempt to explain Brownian movement in terms of collisions was made by von Nägeli [2]. Following Brown's work there were many years of speculation [1, 3] as to the cause of the phenomena before Einstein made conclusive mathematical predictions of a diffusive effect arising from the random thermal motions of particles in suspension.

1.1 Einstein's Explanation of the Brownian Movement:

It was Einstein in 1905 who explained Brownian movement essentially by combining the elementary stochastic process known as the random walk with the Maxwell-Boltzmann distribution [4]. His ideas may be summarized as follows. If a particle moves in a frictionless fluid, it receives a blow due to collision with a molecule and the velocity of the particle changes. However if the fluid is viscous, then the change in velocity is quickly dissipated and the net result is the change in displacement of the particle. Einstein then assumed that the cumulative effect of collisions is to produce random jumps in the position of a Brownian particle,i.e., the particle performs a random walk. Finally he obtained a partial differential equation for the probability distribution of the displacement in one dimension [5]. This equation is similar to that of unsteady heat conduction. Einstein obtained the solution of this equation and showed that the mean-squared displacement of a Brownian particle should increase linearly with time. Using the fact that Maxwellian distribution of velocities must hold in equilibrium he was able to express the constants in terms of temperature and viscosity of the fluid. Perrin verified experimentally this formula for the mean-square displacement in 1908 [1, 6]. He obtained a value of Avogadro's number that agreed within 19% with the present accepted value. This is one of the powerful evidences of molecular structure of matter. We quote from his 1905 paper [7]:
"According to the molecular kinetic theory of heat, bodies of microscopically visible size suspended in a liquid will perform movements of such magnitude that they can be easily observed in a microscope, on account of the molecular motions of heat...On the other hand, had the prediction of the argument proved to be incorrect a weighty argument

would be proved against the molecular-kinetic conception of heat."

1.2 The Langevin Method — Stochastic Differential Equation

The theory of the Brownian movement as formulated by Einstein [3] and Smoluchowski [2] is far removed from the Newtonian dynamics of particles. In general Langevin's method is easier to comprehend than the Fokker-Planck one as it is based directly on the concept of the time evolution of the random variable of the process rather than on the time evolution of the underlying probability distribution. According to Wang and Uhlenbeck [8] the Langevin equation is "the real basis of the theory of Brownian motion". Langevin introduced the concept of the equation of motion of a random variable (in this case the position of the Brownian particle) in 1908 [9]. He assumed that the Brownian particle experiences two forces, namely:

- A systematic force (viscous drag) - $\zeta\dot{x}(t)$ where x is the displacement of the particle and ζ is the coefficient of friction.

- A rapidly fluctuating force F(t) due to the impacts of the molecules of the liquid on the particle . This is the residual force exerted by the surroundings (heat bath).

Thus the equation of motion becomes

$$m\frac{d^2x(t)}{dt^2} = -\zeta\frac{dx(t)}{dt} + F(t), \tag{1.1}$$

where the frictional part follows Stoke's law which states that frictional force decelerating a spherical particle of radius 'a' and in a surrounding fluid of viscosity η is $\zeta\dot{x} = 6\pi\eta a\dot{x}$ and fluctuating part obeys

$$\langle F(t)\rangle = 0 \tag{1.2}$$

$$\langle F(t)F(t')\rangle = 2\pi\zeta k_B T\delta(t-t'). \tag{1.3}$$

1.3 Rotational Brownian Motion

So far we have discussed translational Brownian motion. In 1928 Debye [10, 11] introduced the Fokker-Planck equation for the rotational Brownian motion in space of a sphere in the context of dielectric relaxation. W. F. Brown extended this study for the single domain nanoparticle system in 1963. In his study he assumed that the "giant" magnetic moment undergoes a rotational Brownian motion on the surface of a sphere. The starting point of Brown's treatment of the dynamical behavior of the uniform magnetization of $\vec{M}$ for the single domain particle is

$$\frac{d\vec{M}}{dt} = \gamma\vec{M} \times \Big(- \frac{\partial V}{\partial \vec{M}} - \eta \frac{d\vec{M}}{dt}\Big), \tag{1.4}$$

where γ is the gyromagnetic ratio, η is a phenomenological damping constant and $V(\theta, \phi)$ is the energy. Now Brown proposed that in the presence of thermal agitation the dissipative "effective field" $-\eta\dot{\vec{M}}$ describes only the statistical average of the rapidly fluctuating forces and for an individual particle this is $-\eta\dot{\vec{M}} + \vec{h}(t)$ where thermal fluctuating field h(t) follows:

$$\langle h(t)\rangle = 0 \tag{1.5}$$

$$\langle h_i(t_1)h_j(t_2)\rangle = 2k_BT\eta\delta_{ij}\delta(t_1 - t_2). \tag{1.6}$$

Finally he obtained the following Fokker-Planck equation [12] for the giant magnetic moment

$$\begin{aligned}\frac{\partial W}{\partial t} = & \frac{1}{\sin\theta}\frac{\partial}{\partial\theta}\Big\{\sin\theta\Big[\Big(h'\frac{\partial V}{\partial\theta} - \frac{g'}{\sin\theta}\frac{\partial V}{\partial\phi}\Big)W + k'\frac{\partial W}{\partial\theta}\Big]\Big\} \\ & \frac{1}{\sin\theta}\frac{\partial}{\partial\phi}\Big\{\Big(g'\frac{\partial V}{\partial\theta} + \frac{h'}{\sin\theta}\frac{\partial V}{\partial\phi}\Big)W + \frac{k'}{\sin\theta}\frac{\partial W}{\partial\phi}\Big].\end{aligned} \tag{1.7}$$

$W(\theta, \phi, t)$ is the number density of magnetic moment on the surface of the sphere, g' is the processional term, h' is the alignment term. The constant k' is determined by using the fact that the stationary solution of Eq. (1.6) should be the Maxwell-Boltzmann distribution i.e. $W_0(\theta, \phi, 0) = Ae^{-\beta V(\theta,\phi)}$. For the simplest uniaxial anisotrpic single domain particle in the presence of an external magnetic field H which is assumed parallel to the polar axis, the energy par unit volume is given by

$$V(\theta) = K\sin^2\theta - M_sH\cos\theta, \tag{1.8}$$

where K is the anisotropy constant, M_s is the saturation magnetization, and θ is the angle between the anisotropy axis and the magnetic moment. If the barrier height ($V_{max} - V_{min} = K \pm M_s H$) is much larger than the thermal energy $k_B T$ then the discrete two-state orientation model is justified. In the Kramers method it is assumed that the equilibrium is attained within the regions $0 \leq \theta \leq \theta_1$ and $\theta_2 \leq \theta\pi$. Thus, when $V = V(\theta)$ with minima V_1 and V_2 at $\theta = 0$ and $\theta = \pi$ and with a maximum V_{max} at θ_m ($0 < \theta_m < \pi$), it is naturally assumed that n_1 particles of an ensemble have $\theta = 0$ (orientation 1) and n_2 have $\theta = \pi$ (orientation 2), and a particle in orientation i (= 1 or 2) has probability ν_{ij} per unit time of jumping to orientation j (=2 or 1). Then the approach to statistical equilibrium can be described by rate equations. Hence in the high barrier/low temperature limit the Fokker-Planck equation (Eq. 1.6) can be re-expressed into coupled two-state rate equations [13]:

$$\dot{n}_1 = -\dot{n}_2 = n_2\nu_{21} - n_1\nu_{12}, \tag{1.9}$$

where n_i is the number of particles in the i^{th} (i=1,2) state and ν_{12}, ν_{21} are rate constants.

1.4 Quantum Brownian Motion

In this section we describe the quantum Langevin equation of a particle coupled linearly to a quantum-mechanical heat bath and moving in an arbitrary external potential [14-16]. Consider a quantum particle of mass m moving in a one-dimensional potential V(x) and linearly coupled to a heat-bath at temperature T. The time development of the particle can be described by the equation

$$m\ddot{x} + \int_{-\infty}^{t} dt' \mu(t - t')\dot{x}(t') + V'(x) = F(t), \tag{1.10}$$

where the dot and prime denote derivatives with respect to time and x respectively. This is the Heisenberg equation of motion for the coordinate operator x. Here F(t) is the operator form of the "noise" whose spectral properties are characterized by the symmetric correlation and commutator,

$$\langle\{F_\alpha(t), F_\beta(t')\}\rangle = \delta_{\alpha\beta}\frac{2m\gamma}{\pi}\int_0^\infty d\omega\hbar\omega \coth\left(\frac{\hbar\omega}{2k_BT}\right)\cos[\omega(t - t')], \tag{1.11}$$

$$\langle[F_\alpha(t), F_\beta(t')]\rangle = \delta_{\alpha\beta}\frac{2m\gamma}{i\pi}\int_0^\infty d\omega\hbar\omega \sin[\omega(t - t')], \tag{1.12}$$

where α, β are the Cartesian indices and the angular brackets imply thermal averaging over the heat bath. This is a general macroscopic phenomenological description of the system. Here the mean force exerted by the heat bath is linear in the particle motion. The memory function $\mu(t)$ is independent of the potential V(x) and the particle mass m. It depends only upon the parameters describing the coupling to the bath.

1.5 Physical Application of the Theory of Brownian Motion

In this section we describe physical phenomena to which the Brownian motion theory can be applied. The work of Einstein on Brownian motion is a remarkable exposition of his contact with real life phenomena —- it is a description of a new method for determining the Avogadro number (N) and the size (a) of a molecule. His work on Brownian motion contains results with an extraordinary range of applications, relevant to:

- Bulk rheological properties of particle suspensions.
- Construction industry, based on granular matter.
- Dairy industry through the colloidal suspension properties.
- Ecology, involving the Brownian movement of aerosol particles in clouds.

The theory of Brownian movement in a potential that has been applied to physical phenomena are:

- The current-voltage characteristics of the Josephson tunneling junction.
- Dielectric and Kerr-effect relaxation of an assembly of dipolar molecules, including inertial effects and dipole-dipole interaction.
- The mobility of superionic conductors.
- Linewidths in nuclear magnetic resonance.
- Incoherent scattering of slow neutrons.
- Thermalization of neutrons in a heavy gas moderator.

- Escape of particles over potential barrier.
- Motion of single domain charge-density wave-systems.
- Ferrofluids.

Thus the theory of Brownian movement has wide applications in physical phenomena which has its ramifications in a variety of context.

1.6 Our Study

In the next four chapters we discuss the rotational Brownian motion of a single domain nanomagnetic particle. In chapter 2 we discuss statistical thermal equilibrium properties of noninteracting magnetically anisotropic nanoparticles in the framework of classical equilibrium statistical physics. Further we analyze the distinguishable features of the canonical spinglass phase transition and the progressive freezing of supermoments. Next three chapters are all about non-equilibrium, irreversible processes observed in the nanomagnetic single domain particles. In this context we elucidate the study of "memory effect" and "glassy dynamics" observed in single domain particles by using a simple two-state model, abstracted from an underlying Fokker-Planck equation. Then we extend our study to distinguish the slow dynamics observed in a "superparamagnetic" system and a "superspinglass" system. In chapter 5 we introduce a stochastic model to explain the variation of coercivity with particle size at low temperature as well as at high temperature. These studies of small nanomagnetic systems have wide spectrum of applications which range from magnetic recording media, magnetic fluids, magnetic imaging and magnetic refrigeration, to numerous geophysical, biological, and medical uses.
The Chapter 6 is concerned with the classical Brownian motion of a particle moving in a periodic potential and in a rapidly oscillating external periodic force. In this context we discuss a significant amount of diffusion enhancement in the presence of a space dependent rapidly oscillating force. We have also examined some transport properties like current of the same system. Amongst several practical implications of this work, we might mention separation of different species of Brownian particles by identifying minima of the effective potential, control of the diffusion rates by varying space-dependent external force and

dynamics of molecular motors like kinesin and myosin.

While the problems treated in chapters 2-6 deal with classical Brownian motion we turn our attention in chapters 7 and 8 to the analysis of the quantum Langevin equation of a charged particle moving in a magnetic field and also interacting with its environment. In the subject of dissipative Landau diamagnetism we show the unification of equilibrium and non-equilibrium statistical mechanics. Further work is reported on the validity of the fluctuation-dissipation theorem in the context of Landau-Drude diamagnetism and the zero temperature coherence to decoherence transition .

Chapter 2

Magnetic and Caloric Properties of Magnetic Nanoparticles: An Equilibrium Study

2.1 Introduction

Small, magnetically ordered particles are ubiquitous in our daily life [17-21]. The wide spectrum of applications of these systems which range from magnetic recording media, catalysts, filtering, phase separation in the mineral processing industry, magnetic imaging, magnetic refrigeration to numerous geophysical, biological and medical uses is remarkable. Not only that, these nanometric systems are considered as model systems for various basic physical phenomena [22, 23]. Hence it is necessary to develop deep understanding of the equilibrium and non-equilibrium properties of nanomagnetic particles.

The study of the dynamics of noninteracting classical magnetic moments is an interesting strand of research and seems to be far from exhausted. But before going into a detailed dynamical study of such small nanoparticles we want to analyze the thermal equilibrium properties of the same. Therefore, the purpose of this chapter is to gain a deeper insight into the thermal equilibrium properties of a collection of non-interacting single-domain nanoparticles with the help of equilibrium classical statistical mechanics.

Throughout this chapter and the next three chapters we concentrate on the study of magnetic moments of particles dispersed in a solid matrix. These magnetic moments are linked to the crystal lattice by the magnetic anisotropy. We restrict our study to systems with axially symmetric magnetic anisotropy which makes the problem easily tractable but also provides valuable insight into more complex situations.

The magnetic moment of such a nanoparticle consists of single domain structure of fer-

romagnetic spins with a large net spin (S $\sim 10^3 - 10^4$, supermoment). This spin is coupled to the environmental degrees of freedom of the host material. Due to dynamical disturbances of the surroundings, this large spin undergoes a rotational Brownian motion surmounting the magnetic anisotropy potential barrier [24, 25]. In the high barrier limit, the magnetic response of noninteracting single domain particles will follow the Neel [24] relaxation process characterized by the relaxation time

$$\tau = \tau_0 \exp\Big(\frac{\Delta E_a}{k_B T} \Big), \tag{2.1}$$

where $\tau_0 \simeq 10^{-10} - 10^{-13}$ sec and is related to intra-well motion. Here ΔE_a is the height of the energy barrier due to anisotropy which equals KV (K is the anisotropy constant, and V is the particle volume), k_B is the Boltzmann constant and T denotes absolute temperature. Now depending on the relation between the relaxation time τ and measurement time t_m, different phenomena are observed. When $\tau << t_m$, the magnetic moment exhibits the thermal equilibrium distribution as in a paramagnet. Due to the large value of S, the name superparamagnets is used. On the other hand, if $\tau >> t_m$, the reversal mechanism is blocked and the magnetic moment stays very close to the energy minima. Under intermediate condition, ($\tau \sim t_m$) there is non-equilibrium phenomena i.e. magnetic aging. Hence thermal equilibrium properties are observed when the measurement or observation time t_m is much longer than the characteristic relaxation times of the system.

The subject of spin-glass freezing of many disordered magnetic materials at low temperature is an old one [26-29]. The analogy between the macroscopic behaviour of certain magnetic "glassy" systems (e.g. Au-Fe alloy) and that of ensembles of fine nanomagnetic particles is an enigmatic subject and has received recurrent attention during the last few years [30-33]. However, it is not clear whether all the magnetic properties of fine-particle systems are the same as those of typical spin-glasses (e.g. Au-Fe alloys). The nature of spin-glass freezing is still controversial. So detailed studies of magnetic properties of fine particles are necessary in order to clarify if spin-glass freezing is indeed the progressive freezing of the super-moments.

The spin-glass transition is characterized by the critical behaviour of nonlinear magnetic susceptibilities (NLMS). Bitoh *et al* have shown from the measurement of the susceptibilities $\chi_{2n}(\omega, T)$ how to devise a suitable experimental tool to distinguish between the

spin-glass and the fine-particle attributes. The remarkable feature is the nature of fall of χ_{2n} as T increases above the peak temperature. Unfortunately, theoretical descriptions of NLMS of noninteracting fine-particles are very rare [34, 35]. The first theoretical description on NLMS was given by Jönson et al [34] and later on extended by Garcia-Palacios et al [35].

2.2 Effective Hamiltonian and Partition Function

We mainly consider systems where the magnetic anisotropy energy has the simplest axial symmetry. When an external field $\vec{B}$ is applied the total magnetic energy is

$$\mathcal{H}(\vec{m}) = -\frac{KV}{m^2}(\vec{m}.\hat{n})^2 - \vec{m}.\vec{B}, \tag{2.2}$$

where $\hat{n}$ is a unit vector along the anisotropy axis. Introducing the unit vectors $\hat{e}$ in the direction of the magnetic moment, $\vec{m}$ ($\hat{e} = \frac{\vec{m}}{m}$), $\hat{b}$ in the direction of the magnetic field ($\hat{b} = \frac{\vec{B}}{B}$) and dimensionless anisotropy and field parameters $\sigma = \frac{KV}{k_BT}$ and $\xi = \frac{mB}{k_BT}$ one can express Eq. (2.2) as

$$-\beta\mathcal{H} = \sigma\left(\hat{e}.\hat{n}\right)^2 + \xi\left(\hat{e}.\hat{b}\right) \tag{2.3}$$

We choose the anisotropy axis $\hat{n}$ as the polar axis of a spherical co-ordinate system. (θ, ϕ)

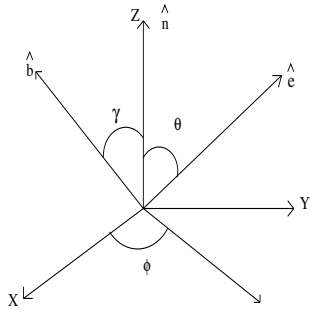

Figure 2.1: Coordinate system showing the unit vectors $\hat{e}, \hat{b}$ and $\hat{n}$ along with the referred angles.

and $(\gamma, 0)$ denote the angular co-ordinate of $\hat{e}$ and $\hat{b}$ respectively. Then the total magnetic potential is given by

$$-\beta\mathcal{H} = \sigma\cos^2\theta + \xi_{\parallel}\cos\theta + \xi_{\perp}\sin\theta\cos\phi, \tag{2.4}$$

where, $\xi_{\parallel} = \xi \cos\gamma$ and $\xi_{\perp} = \xi \sin\gamma$. The partition function associated with the Hamiltonian (cf. Eq. (2.4)) is defined as

$$\mathcal{Z} = \int_0^{\pi} d\theta \sin\theta \exp(\sigma \cos^2\theta + \xi_{\parallel} \cos\theta) I_0(\xi_{\perp} \sin\theta), \tag{2.5}$$

where $I_0(y)$ is the zeroth order modified Bessel function of the first kind [36]. After some algebra one can show

$$\mathcal{Z} = 2R(\sigma) \sum_{i=0}^{\infty} \frac{C_i(\sigma,\gamma)}{i!} \xi^{2i}, \tag{2.6}$$

where,

$$C_i(\sigma,\gamma) = i! \sum_{k=0}^{i} b_{i-k,k}(\gamma) \sum_{m=0}^{k} (-1)^m \frac{k!}{m!(k-m)!} \frac{R^{(i-k+m)}(\sigma)}{R(\sigma)}. \tag{2.7}$$

$$b_{i,k}(\gamma) = \frac{1}{(2i)! 2^{2k} (k!)^2} \cos^{2i}\gamma \sin^{2k}\gamma, \tag{2.8}$$

and

$$R^{(l)}(\sigma) = \int_0^1 dz z^{2l} \exp(\sigma z^2) \tag{2.9}$$

The partition function hence obtained helps further calculation of the equilibrium properties.

2.3 Equilibrium Properties

In this section we discuss a number of important thermodynamic quantities of non-interacting magnetic nanoparticles with axially symmetric magnetic anisotropy. In particular, we analyze the effect of magnetic anisotropy on the magnetization ($\mathcal{M}$) as well as the linear (χ_0) and nonlinear (χ_2, χ_4) susceptibilities. The differences and similarities of the linear and nonlinear susceptibilities between canonical spinglass systems, such as $Au_{96}Fe_4$ [37-39] and magnetic nanoparticle systems, such as $Cu_{97}Co_3$ [33], are presented.

2.3.1 Magnetization

The magnetization along the external field direction for classical spins with axially symmetric magnetic anisotropy is defined as follows

$$\mathcal{M}_B = \langle \vec{m}.\hat{b} \rangle_{eq} = m \frac{\partial}{\partial \xi} (\ln \mathcal{Z}). \tag{2.10}$$

Taking derivative with respect to ξ of the low-ξ expansion of $\ln \mathcal{Z}$, we obtain

$$\mathcal{M}_B = m\Big[2C_1\xi + 2(C_2 - C_1^2)\xi^3 + (C_3 - 3C_2C_1 + 2C_1^3)\xi^5 + ...\Big] \tag{2.11}$$

where the co-efficients C_i are given by Eq. (2.7). We now study Eq. (2.11) for particular cases.

(i)*Isotropic case ($\sigma = 0$)*: In this case $C_1 = \frac{1}{6}$, $C_2 = \frac{1}{60}$, $C_3 = \frac{1}{840}$..... and so on. Thus we obtain

$$\mathcal{M}_{B,Lan} = mL(\xi), \tag{2.12}$$

where $L(\xi)$ is the Langevin function.

(ii)*Ising case ($\sigma \to \infty$)*: In this regime $C_1 = \frac{\cos^2\gamma}{2}$, $C_2 = \frac{\cos^4\gamma}{12}$, $C_3 = \frac{\cos^6\gamma}{120}$ and so on. Thus the magnetization becomes

$$\mathcal{M}_{B,Ising} = m\cos\gamma\tanh\xi_{\parallel}. \tag{2.13}$$

It shows that the magnetization vanishes when $\vec{B}$ is perpendicular to the anisotropy axis $\hat{n}$.

(iii)*Plane rotator case ($\sigma \to -\infty$)*: In this case $C_1 = \frac{\sin\gamma}{4}$, $C_2 = \frac{\sin^4\gamma}{32}$, $C_3 = \frac{\sin^6\gamma}{384}$ and so on.

$$\mathcal{M}_{B,rot} = m\sin\gamma\frac{I_1(\xi_\perp)}{I_0(\perp)}. \tag{2.14}$$

In this case the magnetization vanishes when $\vec{B}$ is perpendicular to the rotator plane.

(iv)*Longitudinal field case ($\vec{B}\|\hat{n}$)*: Now we have $C_1 = \frac{R'}{2R}$; $C_2 = \frac{R''}{12R}$; $C_3 = \frac{R'''}{120R}$ and so on. Now the magnetization becomes

$$\mathcal{M}_{B,\|} \;=\; m\Big[\frac{R'}{R}\xi + \frac{1}{2}\Big(\frac{1}{3}\frac{R''}{R} - (\frac{R'}{R})^2\Big)\xi^3 + ...\Big]. \tag{2.15}$$

Here one can easily note that $\mathcal{M}_B$ depends on B and T through ξ in all the first three cases. So the magnetization versus $\frac{B}{T}(\sim \xi)$ curves corresponding to different temperatures collapse onto a single master curve as shown in Fig. 2.2(a). However outside these three limiting cases, T does not enter in $\mathcal{M}_B$ via $\frac{B}{T}$ only, but $\mathcal{M}_B$ depends on ξ as well as σ also. This is shown in Fig. 2.2(b) for the longitudinal field case. As T decreases, one can see the crossover from the high temperature isotropic regime to the low temperature Ising regime. This crossover is induced by the magnetic anisotropy.

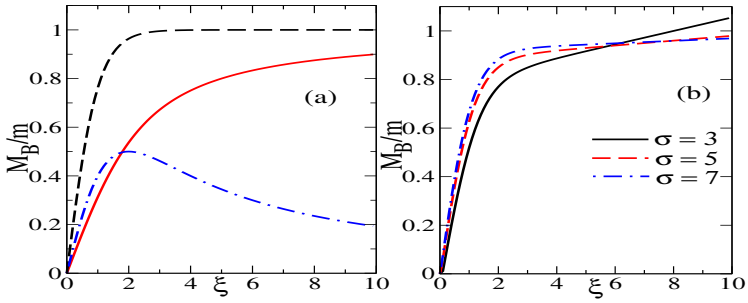

Figure 2.2: (a)Magnetization versus field curves corresponding to different temperatures for the isotropic case (red), for the Ising case (green) and for the plane-rotator case (blue); (b)Magnetization versus longitudinal field showing the non-$\frac{B}{T}$ superposition of the magnetization curves.

2.3.2 Linear Susceptibility (χ_0)

We now study the linear susceptibility of classical "superspin" with axially symmetric magnetic anisotropy. We start our discussion with the low-field expansion of the magnetization ($H = \frac{B}{\mu_0}$)

$$\mathcal{M}_B = \chi_0 H + \chi_2 H^3 + \chi_4 H^5 + ..., \tag{2.16}$$

where χ_0 is the linear susceptibility and χ_2, χ_4 are the nonlinear susceptibilities. Comparing Eqs. (2.11) and (2.16) we obtain

$$\chi_0 = 2mC_1 = \frac{\mu_0 m^2}{k_B T} 2C_1(\sigma, \gamma). \tag{2.17}$$

Thus the general expression of linear susceptibility is given by

$$\chi_0 = \chi_0^{\parallel} \cos^2\gamma + \chi_0^{\perp} \sin^2\gamma, \tag{2.18}$$

where $\chi_0^{\parallel} = \frac{\mu_0 m^2}{k_B T}\frac{R'}{R}$; $\chi_0^{\perp} = \frac{\mu_0 m^2}{k_B T}\frac{R-R'}{2R}$. Figure (2.3) shows the polar plot of linear susceptibility as a function of the angle between the anisotropy axis and the probing field for the easy-axis anisotropy and easy-plane anisotropy for various values of σ. It shows that larger the $|\sigma|$, the χ_0 curves become more anisotropic. The limiting cases of the linear susceptibility for the four regimes are $\chi_0^{Lan} = \frac{\mu_0 m^2}{3k_B T}$; $\chi_0^{Ising} = \frac{\mu_0 m^2}{k_B T}\cos^2\gamma$; $\chi_0^{Plane-Rotator} = \frac{\mu_0 m^2}{2k_B T}\sin^2\gamma$; and $\chi_0^{\parallel} = \frac{\mu_0 m^2}{k_B T}\frac{R'}{R}$. In Fig. 2.4(a) we plot the reduced linear susceptibility versus dimensionless anisotropy parameter in the longitudinal and transverse field cases. Both curves

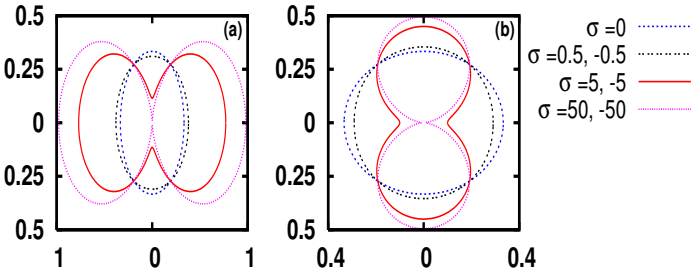

Figure 2.3: Polar plot of χ_0 versus γ for different values of σ (a) easy-axis anisotropy (b) easy-plane anisotropy.

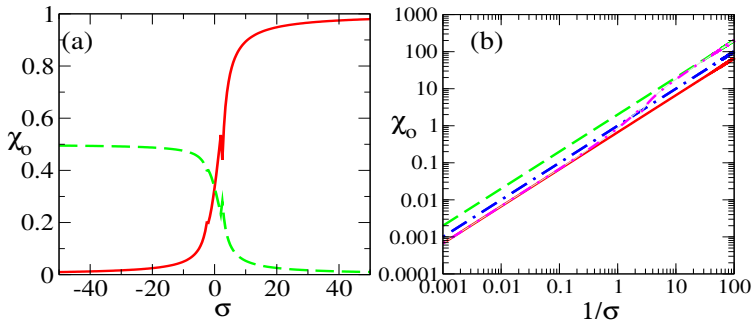

Figure 2.4: (a)Plot of linear susceptibility versus σ in the longitudinal (red) and transverse (green) field cases; (b) log-log plot of χ_0 versus $\frac{1}{\sigma}$ for the isotropic case (red), Ising case (green), plane-rotator case (blue) and the randomly distributed anisotropy case (pink).

coincide at $\sigma = 0$ taking the Langevin value of $\frac{1}{3}$. It is understood from Fig. 2.4(a) that the longitudinal and the transverse field cases interchange their roles when the sign of the anisotropy is changed. Figure 2.4(b) shows the log-log plot of the linear susceptibility versus the dimensionless temperature ($\frac{1}{\sigma}$). As the influence of the anisotropy decreases with the increase of temperature, χ_0 undergoes a smooth crossover from the low-temperature Ising regime to the high-temperature Langevin case. The slope of the curves are one which occur in the asymptotic regime (T^{-1}) dependence, but deviation from this inverse temperature dependence is sizable in the transitional region. In this transitional region the slope is less than one. The temperature dependence of the longitudinal and transverse component of the linear susceptibility seem to have broad peaks (Fig. 2.5(a), 2.5(b)).

Both $\chi_0^{\parallel}$ and $\chi_0^{\perp}$ show broad peak. Bitoh et al [33, 40] have shown temperature dependence of χ_0 in $Cu_{97}Co_3$ fine particle system and in $Au_{96}Fe_4$ spinglass system. The peak of $Cu_{97}Co_3$ is broad compared to that of $Au_{96}Fe_4$. So our theoretical results (Fig. 2.5) qualitatively reproduce the experimental results.

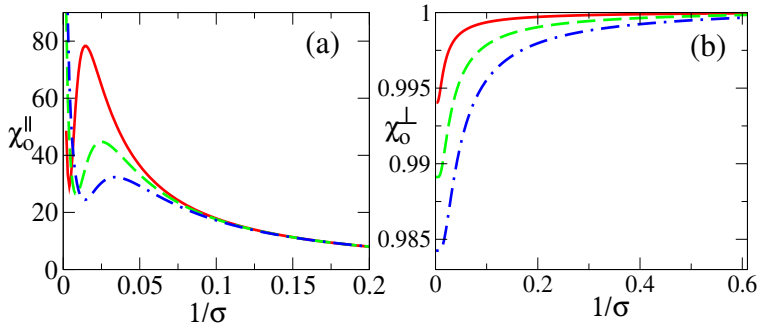

Figure 2.5: (a) Longitudinal and (b) transverse components of the linear susceptibility versus $1/\sigma$ with $h = 0.006$ (red), $h = 0.011$ (green) and $h = 0.016$ (blue) and these curves exhibit spinglass like maximum.

2.3.3 Nonlinear Susceptibilities (χ_2, χ_4)

We now study the nonlinear susceptibilities of classical spins with uniaxial magnetic anisotropy. The main goal of this study is to invoke the suitability of these quantities in the study of collective phenomena of glassy systems and also the glassy like behavior of some fine particles ($Cu_{97}Co_3$). Bitoh et al [33, 40] have shown that χ_2 gives the key to clarify the differences between the spinglass transition and the progressive freezing of the supermoments. In this subsection we present a rigorous theoretical analysis of these nonlinear magnetic susceptibilities and discuss their different properties for the classical spins as well as for the spinglass system.

The nonlinear susceptibilities are defined as the coefficients of the nonlinear terms in the expansion of the magnetization in powers of the external field. Now comparing Eqs.

(2.11) and (2.16) we obtain

$$\chi_2 = \frac{\mu_0^3 m^4}{(k_B T)^3} 2\Big(C_2 - C_1^2\Big), \tag{2.19}$$

$$\chi_4 = \frac{\mu_0^5 m^6}{(k_B T)^5}\Big(C_3 - 3C_2C_1 + 2C_1^3\Big). \tag{2.20}$$

In Fig. 2.6 we plot the angular dependence of the reduced nonlinear susceptibility χ_2 in the cases of easy-axis anisotropy and easy-plane anisotropy for various values of σ. It is seen that χ_2 curves become more anisotropic as $|\sigma|$ increases and becomes quite different from circles for $|\sigma| > 0$. The sizes of the isotropic case is different for $K > 0$ and $K < 0$ cases because the maximum values of χ_2 for $K > 0$ and $K < 0$ are quite different. Figures 2.7 and 2.8 display the angular dependence of χ_4 for the $K > 0$ and $K < 0$ cases respectively. Let us consider various particular cases for the nonlinear susceptibilities.

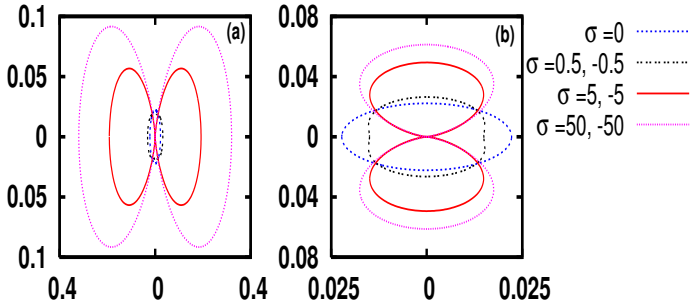

Figure 2.6: Polar plot of χ_2 versus γ for different values of σ (a) easy-axis anisotropy (b) easy-plane anisotropy.

(i)*Isotropic case ($\sigma = 0$)*:

$$\chi_2 = -\frac{\mu_0^3 m^4}{45(k_B T)^3} \tag{2.21}$$

$$\chi_4 = \frac{2}{945}\frac{\mu_0^5 m^6}{(k_B T)^5}. \tag{2.22}$$

(ii)*Ising case ($\sigma \to \infty$)*:

$$\chi_2 = -\frac{\mu_0^3 m^4}{3(k_B T)^3}\cos^4\gamma \tag{2.23}$$

$$\chi_4 = \frac{2}{15}\frac{\mu_0^5 m^6}{(k_B T)^5}\cos^6\gamma. \tag{2.24}$$

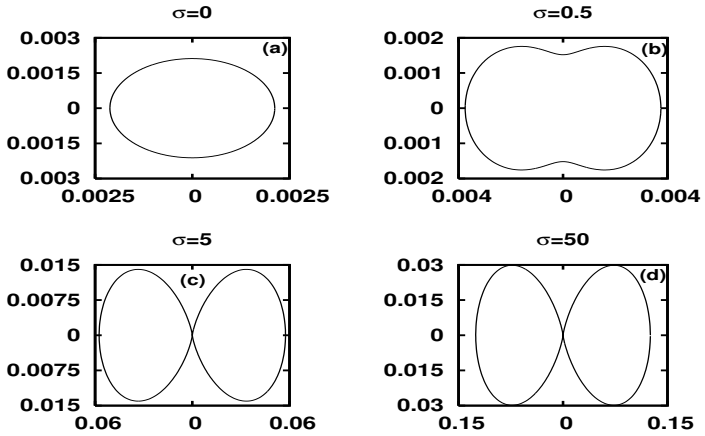

Figure 2.7: Polar plot of χ_4 versus γ for different values of σ for the easy-axis anisotropy.

(ii)*Plane rotator case ($\sigma \to -\infty$)*:

$$\chi_2 = -\frac{\mu_0^3 m^4}{16(k_B T)^3} \sin^4 \gamma \tag{2.25}$$

$$\chi_4 = \frac{1}{96} \frac{\mu_0^5 m^6}{(k_B T)^5} \sin^6 \gamma. \tag{2.26}$$

(ii)*Longitudinal field case ($\vec{b} \| \hat{n}$)*:

$$\chi_2 = \frac{\mu_0^3 m^4}{(k_B T)^3} \Big[\frac{1}{2} \Big(\frac{1}{3} \frac{R''}{R} - (\frac{R'}{R})^2 \Big) \Big] \tag{2.27}$$

$$\chi_4 = \frac{\mu_0^5 m^6}{(k_B T)^5} \Big[\frac{1}{4} \Big(\frac{R'''}{30R} - \frac{R'' R'}{2R^2} + (\frac{R'}{R})^3 \Big) \Big]. \tag{2.28}$$

Figure 2.9(a) shows χ_2 versus σ in the longitudinal and transverse field cases as well as for the anisotropy axes distributed at random. These three curves coincide at $\sigma = 0$ and take the Langevin value $-\frac{1}{45}$. The large deviation for the anisotropy is observed in the parallel field case. This deviation is dramatically reduced for the random distribution of anisotropy axes. The longitudinal and the transverse field cases interchange their roles when the sign of the anisotropy is reversed. In Fig. 2.9(b) we show the log-log plot of χ_2 versus $\frac{1}{\sigma}$ for the Ising case, plane rotator case, isotropic case and for the random distribution of anisotropy axes. We can see a smooth crossover from low temperature Ising regime to the high temperature isotropic regime. In the transitional regime the departure of $\chi_2(T)$ from an inverse temperature-cubed law is sizable. Figure 2.10(a) shows the

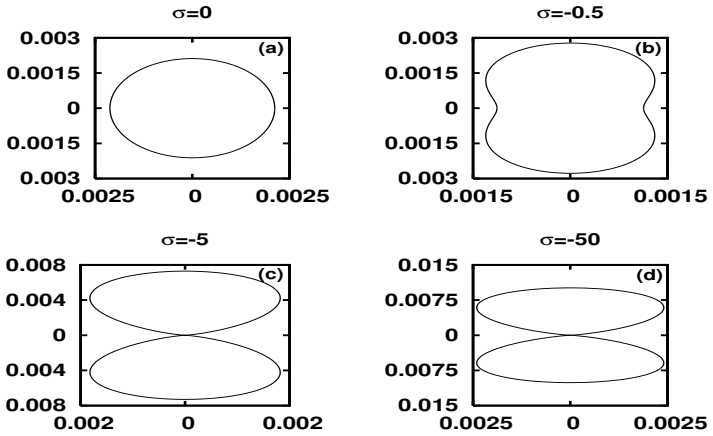

Figure 2.8: Polar plot of χ_4 versus γ for different values of σ for the easy-plane anisotropy.

log-log plot of χ_4 versus dimensionless temperature for different limiting cases like Ising, isotropic, plane rotator and the randomly oriented anisotropy axes. It is seen that as the influence of anisotropy decreases with increasing T, χ_4 goes smoothly from the high temperature isotropic regime to low temperature Ising regime. The transition region is very wide in range and in the transition region there is a significant deviation from the T^{-5} law. On the other hand, Fig. 2.10(b) shows χ_4 versus σ in the longitudinal, transverse and the random distributed anisotropy axes cases. The three curves coincide at $\sigma = 0$ and they take the Langevin value $\frac{2}{945}$. Although the large deviation from the Langenvin result is observed in the parallel field case, the deviation in the perpendicular field case is comparable to that of the parallel case. The random distribution of anisotropy axes reduces this anisotropy induced departure. One can notice that qualitatively the nature of $\chi_4^{\parallel}$ and $\chi_4^{\perp}$ are just opposite to that of the $\chi_2^{\parallel}$ and $\chi_2^{\perp}$. Again the roles of the longitudinal and the transverse field cases are interchanged when the sign of the anisotropy is reversed. We discuss the canonical spinglass phase transition based on the mean field theory. The first attempt to make the mean field theory of spinglass was done by Edwards and Anderson [26]. The Hamiltonian for the system is

$$\mathcal{H} = -\frac{1}{2}\sum_{<ij>} J_{ij}\vec{S}_i.\vec{S}_j - H\sum_i S_i^z, \tag{2.29}$$

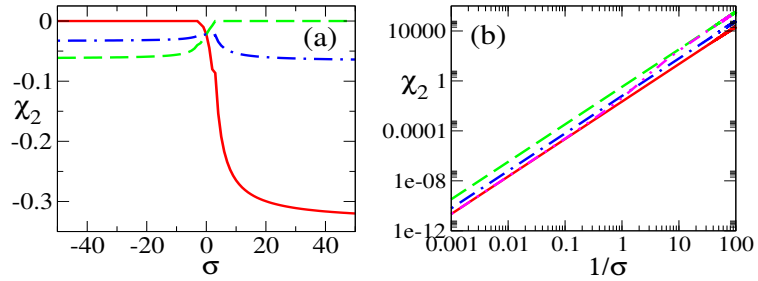

Figure 2.9: (a) Plot of χ_2 versus σ in the longitudinal (red), transverse (green) field and random distribution (blue) cases; (b) log-log plot of χ_2 versus $\frac{1}{\sigma}$ for the isotropic case (red), Ising case (green), plane-rotator case (blue) and the randomly distributed anisotropy case (pink).

where $\vec{S}_i$ is the spin vector on site i, S_i^z is the component of $\vec{S}_i$ along the applied field H. The exchange coupling constants J_{ij} are randomly chosen according to a fixed distribution

$$p(J_{ij}) = \frac{1}{\sqrt{2\pi}J_0} \exp\Big[-\frac{-(J_{ij}-J)^2}{2J_0^2}\Big], \tag{2.30}$$

where J is a mean value and J_0 is a variance of the distribution. Following Suzuki et al [41] one can show that the order parameter susceptibility is

$$\chi_{sg} \simeq \frac{1}{2k_B^2 T_g^2}\Big(\frac{T_g}{T-T_g}\Big), \tag{2.31}$$

where spinglass transition temperature T_g is $\frac{\sqrt{z}J_0}{k_B}$. z is the number of nearest neighbor spins. Now following Wada et al [42] and Sherrington et al [43] we obtain for the linear susceptibility $\chi_0 \sim (\chi_{sg})^{\frac{1}{2}}$. Thus

$$\chi_0 = \frac{1}{\sqrt{2k_B^2 T_g^2}}\Big(\frac{T_g}{T-T_g}\Big)^{\frac{1}{2}}. \tag{2.32}$$

The nonlinear susceptibilities χ_2 and χ_4 are given by

$$\chi_2 = -\frac{1}{2k_B^3 T_g^3}\Big(\frac{T_g}{T-T_g}\Big) \tag{2.33}$$

$$\chi_4 = \frac{1}{32k_B^5 T_g^5}\Big(\frac{T_g}{T-T_g}\Big)^{\frac{3}{2}} \tag{2.34}$$

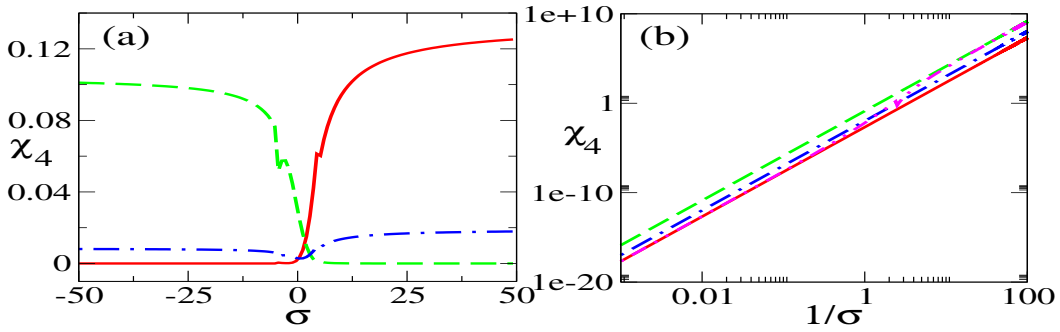

Figure 2.10: (a)Plot of χ_4 versus σ in the longitudinal (blue), transverse (black) field and random distribution (red) cases; (b)Log-log plot of χ_4 versus $\frac{1}{\sigma}$ for the isotropic case (blue), Ising case (black), plane-rotator case (red) and the randomly distributed anisotropy case (green) .

Thus both the linear and nonlinear susceptibilities of canonical spinglass systems diverge at T_g obeying Eqs. (2.32), (2.33) and (2.34) respectively. χ_0 and χ_4 diverge positively whereas χ_2 diverges negatively at T_g. On the other hand we have seen that both the linear susceptibility and χ_4 show broad positive peak and χ_2 has a negative broad peak. The temperature dependence of χ_0, χ_2 and χ_4 are quite different for the classical superspins and that of the canonical spinglass systems.

2.4 Caloric Properties

In this section we discuss the caloric quantities like energy, entropy and specific heat in a number of particular situations.

(i)*Isotropic case ($\sigma = 0$)*: In this case internal energy is

$$u_{Lan} = -m\Big(\coth\xi - \frac{1}{\xi}\Big). \tag{2.35}$$

The entropy is formulated as

$$\frac{S_{Lan}}{k_B} = \ln\Big(\frac{2\sinh\xi}{\xi}\Big) - \xi\Big(\coth\xi - \frac{1}{\xi}\Big). \tag{2.36}$$

The Langevin specific heat is given by

$$\frac{C_{B,Lan}}{k_B} = 1 - \frac{\xi^2}{\sinh^2\xi}. \tag{2.37}$$

(ii)*Zero field case*: In this case the mean energy is given by

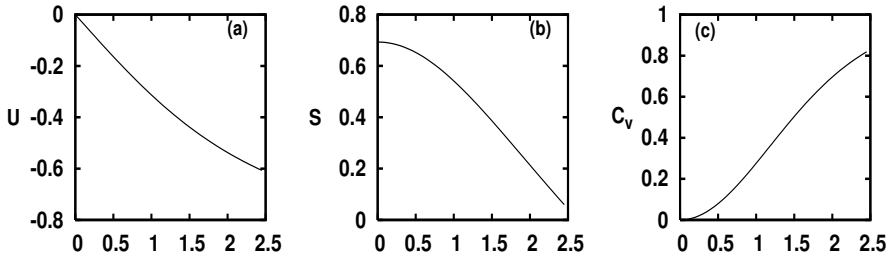

Figure 2.11: Inverse temperature dependence of (a) u, (b) S, and (c) specific heat for the isotropic case.

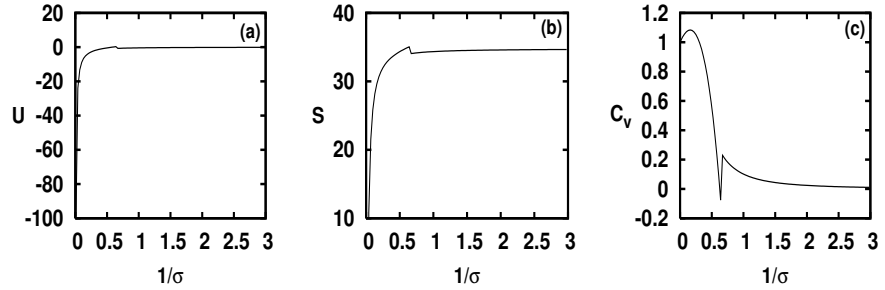

Figure 2.12: Temperature dependence of (a) u, (b) S, and (c) specific heat for the zero field case.

$$u_{unb} = -KV\frac{R'}{R}. \tag{2.38}$$

Zero field entropy and specific heat are given by

$$\frac{S_{unb}}{k_B} = \ln(2R) - \sigma\frac{R'}{R}, \tag{2.39}$$

$$\frac{c_{B,unb}}{k_B} = \sigma^2\Big[\frac{R''}{R} - (\frac{R'}{R})^2\Big]. \tag{2.40}$$

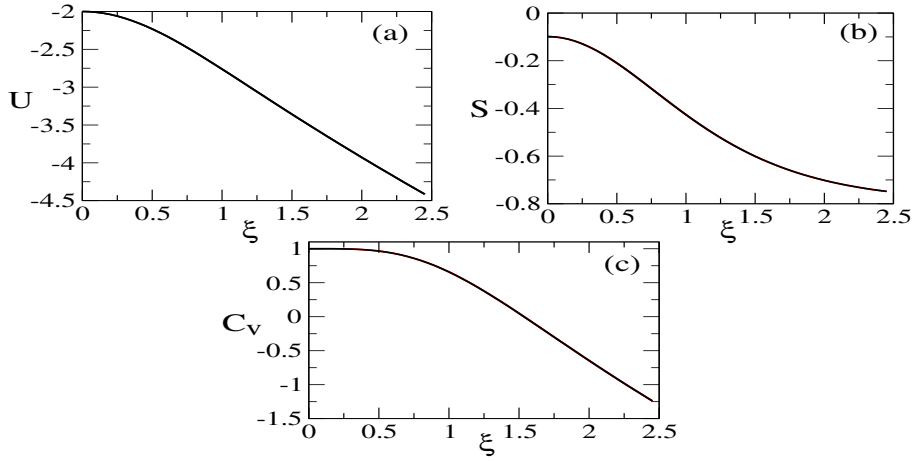

Figure 2.13: Inverse temperature dependence of (a) u, (b) S, (c) Specific heat for the Ising case.

(iii)*Ising case ($\sigma \to \infty$)*: In the Ising regime internal energy and entropy are given by

$$u_{Ising} = -\Big[KV - \frac{KV}{\sigma} + mB\cos\gamma\tanh\xi_{\parallel}\Big] \tag{2.41}$$

$$\frac{S_{Ising}}{k_B} = \sigma - \ln\sigma + \ln(\cosh\xi_{\parallel}) - \beta(KV - \frac{KV}{\sigma} + mB\cos\gamma\tanh\xi_{\parallel})\Big]. \tag{2.42}$$

and the specific heat is

$$\frac{c_{B,Ising}}{k_B} = 1 + \xi^2\cos^2\gamma sech^2(\xi\cos\gamma) - \xi\cos\gamma\tanh(\xi\cos\gamma). \tag{2.43}$$

(iv)*Plane-rotator case ($\sigma \to -\infty$)*: In this limiting condition internal energy, entropy and specific heat are given by

$$u_{rot} = \frac{KV}{2\sigma} - \frac{I_1(\xi_\perp)}{I_0(\xi_\perp)}mB\sin\gamma, \tag{2.44}$$

$$\frac{S_{rot}}{k_B} = -\frac{1}{2} + \frac{\xi_\perp I_1(\xi_\perp)}{I_0(\xi_\perp)}, \tag{2.45}$$

$$\frac{c_{B,rot}}{k_B} = -\frac{1}{2} - \xi_\perp^2\Big[\frac{I_0(\xi_\perp)I_2(\xi_\perp) - I_1^2(\xi_\perp)}{I_0^2(\xi_\perp)}\Big]. \tag{2.46}$$

(v)*Longitudinal field case*: In this case internal energy is given by

$$u_{\parallel} = KV\Big[h^2 - \frac{(1+h)^3R'(\sigma_+) + (1-h)^3R'(\sigma_-)}{(1+h)R'(\sigma_+) + (1-h)R'(\sigma_-)}, \tag{2.47}$$

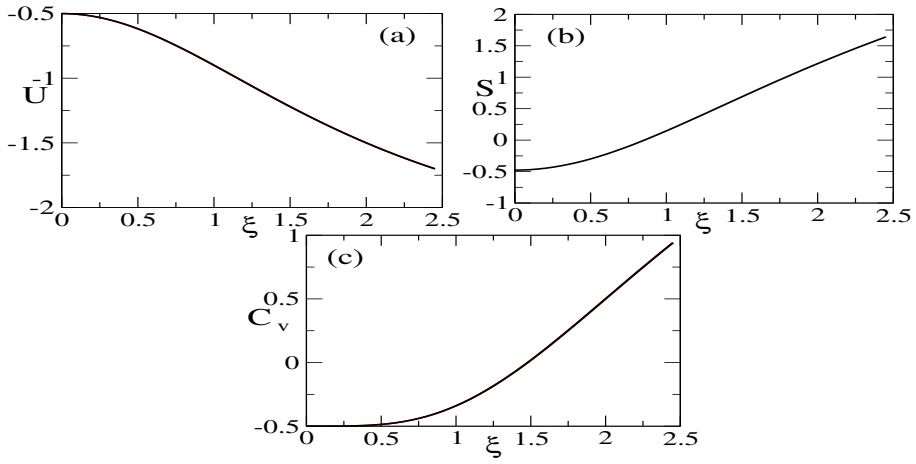

Figure 2.14: Inverse temperature dependence of (a) u, (b) S, and (c) specific heat for the plane-rotator case.

where $\sigma_\pm = \sigma(1 \pm h)^2$ and $h = \frac{\xi}{2\sigma}$. The entropy and specific heat are given by

$$S_\parallel = \ln\Big[(1+h)R(\sigma_+) + (1-h)R(\sigma_-)\Big] - \sigma\frac{(1+h)^3R'(\sigma_+) + (1-h)^3R'(\sigma_-)}{(1+h)R'(\sigma_+) + (1-h)R'(\sigma_-)} \tag{2.48}$$

$$\frac{c_{B,\parallel}}{k_B} = \Big\{\frac{(1+h)^5R'(\sigma_+) + (1-h)^5R'(\sigma_-)}{(1+h)R'(\sigma_+) + (1-h)R'(\sigma_-)} - \Big[\frac{(1+h)^3R'(\sigma_+) + (1-h)^3R'(\sigma_-)}{(1+h)R'(\sigma_+) + (1-h)R'(\sigma_-)}\Big]^2\Big\}\sigma^2. \tag{2.49}$$

In all the above mentioned limiting cases, specific heat obeys a T^{-2} law at high temperatures and tends to nonzero values at low temperatures. This last fact does not obey Nernst's theorem which states that $C_v \to 0$ as $T \to 0$. This actually occurs due to the classical nature of the spins. In the longitudinal field case, entropy and specific heat both display a maximum. The height and location of this maximum depend on the applied field. At high fields Zeeman energy dominates over the anisotropy energy and thus the maximum is smeared out and its height decreases. This maximum can be understood in terms of crossover from high temperature isotropic regime to the low temperature Ising regime.

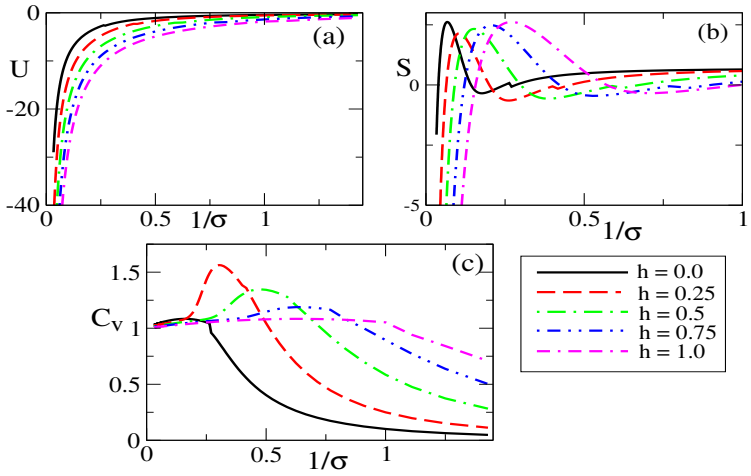

Figure 2.15: Temperature dependence of (a) u, (b) S and (c) specific heat for the longitudinal field case.

2.5 Summary and Conclusions

We have studied the magnetic and caloric properties of non-interacting anisotropic nanoparticles. Through the low field expansion of magnetization, we derive linear (χ_0) and non-linear susceptibilities (χ_2, χ_4) for a number of particular situations. In this analysis we have examined the effect of anisotropic potential on these magnetic properties of superparamagnetic fine particles. This anisotropic potential induces a crossover from free-rotator to either two-state or plane-rotator regime. In the crossover regime the temperature dependence of χ_0, χ_2 and χ_4 are much steeper than those of the limit inverse-temperature power laws (T^{-1}, T^{-3} and T^{-5}) respectively. This might misleadingly suggest the presence of inter-particle interaction because the non-linear susceptibilities resemble the high-temperature ranges of divergence at low temperature. Thus we have drawn out the basic differences between the canonical spinglass phase transition (e.g. in $Au_{96}Fe_4$) and the progressive freezing of the supermoments (e.g. in $Cu_{97}Co_3$). The linear susceptibility χ_0 and non-linear susceptibility χ_4 show positive peak whereas χ_2 has a negative

peak for the superparamagnetic fine-particle systems. However, the negative peak in χ_2 and positive peaks in χ_0 and χ_4 are very broad compared with that of the spinglass systems. The roundness of the peak and the width of the susceptibility curves are the distinguishing features between the spinglass phase transition and the progressive freezing of the supermoments. The analysis of the caloric properties show the essential role of the anisotropic potential and it proves the classical nature of the "supermoments".

The above analysis indicates that the origin of magnetic properties of superparamagnetic fine particles and spinglasses is very different, though the behavior of linear susceptibility and the magnetization of fine particles is similar to those of spinglasses. The non-linear susceptibilities play a crucial role in distinguishing canonical spinglass phase transition and the progressive freezing of supermoments. In conclusion, we can state that our study will help distinguish between the spinglass transition and the progressive freezing of "supermoments".

Chapter 3

Memory in a Magnetic Nanoparticle System - Polydispersity and Interaction Effects.

3.1 Introduction

Since the pioneering work of Neel almost six decades ago [24], the magnetic properties of nanoparticles have attracted immense attention due to their significance in both technological applications and fundamental research [17-21]. These systems can be considered as very good model systems for rotational Brownian motion, thermally activated multistable phenomena [22] and stochastic resonance [23].

The magnetic moment of the nanoparticle is a giant moment of a single domain comprising ferromagnetic spins with a large net spin (S $\sim 10^3 - 10^4$, supermoment). This spin is coupled to the environmental degrees of freedom (eg. phonons) of the host material. Due to dynamical disturbances of the surroundings this large spin undergoes a rotational Brownian motion surmounting the magnetic anisotropy potential barrier [24, 25]. In the high barrier limit, the magnetic response of noninteracting single domain particles will follow a Neel [24] relaxation process characterized by the relaxation time

$$\tau = \tau_0 \exp\Big(\frac{\Delta E_a}{k_B T} \Big), \tag{3.1}$$

where $\tau_0 \simeq 10^{-10} - 10^{-13}$ sec. The parameter τ is related to intrawell motion, the height of the energy barrier due to anisotropy $\Delta E_a = KV$ (K is the anisotropy constant, and V is the particle volume) as well as the thermal energy. In Eq. (3.1) k_B is the Boltzmann constant and T is the absolute temperature. For our purpose K would be treated as a parameter whose typical value is about 10^{-1} Joule/cm^3. Therefore, at room temperature,

τ can be as small as 10^{-1} sec for a particle of diameter 11.5 nm but can be astoundingly as large as 10^9 sec for a particle of diameter just about 15 nm. Thus, a slight polydispersity (i.e., a distribution in the volume V) can yield a plethora of time scales, giving rise to interesting slow dynamics. Depending on the relation between the relaxation time τ and measurement time t_m, different phenomena are observed. When $\tau << t_m$, the magnetic moment exhibits the thermal equilibrium distribution as in a paramagnet. Due to the large value of S, the name superparamagnet is used. On the other hand, if $\tau >> t_m$, the reversal mechanism is blocked and the magnetic moment stays very close to the energy minima. The crossover mark, derived from the temperature dependence of τ, yields the concept of 'blocking temperature' (T_B). Under intermediate condition ($\tau \sim t_m$), there is interesting time-dependent phenomena. Thus single-domain magnetic particles have been a happy hunting ground for studying non-equilibrium physics, characterized by irreversibility, hysteresis and other memory effects.

In recent times this subject has attracted a great deal of attention in view of the heightened interest in Nanoscience and magnetic memory devices. As it turns out, it is not just the temperature T which can be used as a control parameter but even the mean size and the distance between the particles can be profitably tuned because of the exponential dependence of τ on the volume (V) of the particle [44-50]. Thus polydispersity leads to a distribution of relaxation times [51, 52], those larger than the measurement time yielding 'frozen' behavior, whereas those shorter giving rise to 'magnetic viscosity' [49, 50]. A given sample then displays strong memory effects which are reported here. Our results are based on the measurements of temperature-dependent magnetization during cooling and heating cycles. These memory effects may have important device applications in the future [45] . Here we report the theory of relaxation, relevant to magnetization and coercivity measurements, and back up our theory results with qualitative comparison with experimental data.

The system we employ for our investigation is nickel ferrite single domain nanoparticles ($NiFe_2O_4$) embedded in a host nonmagnetic SiO_2 matrix. We prepared the following two specimen samples by using the sol-gel technique [53]. Sample A, which contains 35% $NiFe_2O_4$ (by volume) making possible a weak dipolar interaction between the magnetic nanoparticles, and sample B, which contains 15% $NiFe_2O_4$ (by volume) yield an almost

noninteracting sample. Both X-ray photograph and TEM micrograph suggest that the mean interparticle separation is 5 nm for specimen A and is 15 nm for specimen B, whereas for each specimen the average particle radius is $\simeq 3nm$.
In the next section we review the basic relaxation theory of single-domain magnetic particles and specialize to the case of large uniaxial anisotropy *vis-a-vis* the thermal energy. In this limit the relaxation dynamics can be described in terms of a two-state rate theory. We motivate next a mean field theory in order to incorporate a *weak* dipolar interaction between the magnetic particles. The theory developed in the next section is employed to interpret the irreversible magnetization measurements in the field-cooled (FC) and zero field-cooled (ZFC) processes.

3.2 Relaxation Theory

We assume for the sake of simplicity that the anisotropy, responsible for single-domain behaviour of the magnetic nanoparticle, is uniaxial governed by the energy:

$$E(\Phi) = VK \sin^2 \Phi \tag{3.2}$$

In Eq. (3.2), V is the volume of the particle, K is a parameter referred to in the literature as the anisotropy energy, and Φ is the angle between the anisotropy axis and the direction of the 'giant' magnetic moment of the single-domain particle. Because of thermal fluctuations the magnetic moment undergoes rotational Brownian motion over an anisotropy barrier in Eq. (3.2), in which $\Phi(t)$ is a continuous stochastic process as a function of the time t [25]. However it turns out that if $VK >> k_BT$, k_B being the Boltzmann constant and T is the absolute temperature, the magnetic moment is mostly locked in two orientations, corresponding to $\Phi = 0$ and $\Phi = \pi$, with slow relaxation between the two configurations. Thus we are in the so-called 'Ising' limit in which $\Phi(t)$ may be viewed as a dichotomic Markov process, in which it jumps at random between the angles 0 and π at a rate governed by the Arrhenius-Kramers formula:

$$\lambda_{0\to\pi} = \lambda_{\pi\to 0} = \lambda_0 \exp(-\frac{KV}{k_BT}), \tag{3.3}$$

where λ_0 is the 'attempt' frequency which is the inverse of τ_0 in Eq. (3.1). In what follows we restrict our discussion to the Ising case wherein the magnetic moment vector points either parallel or antiparallel to the anisotropy axis.

We now discuss the effect of interaction which we assume to be dipolar in nature. It

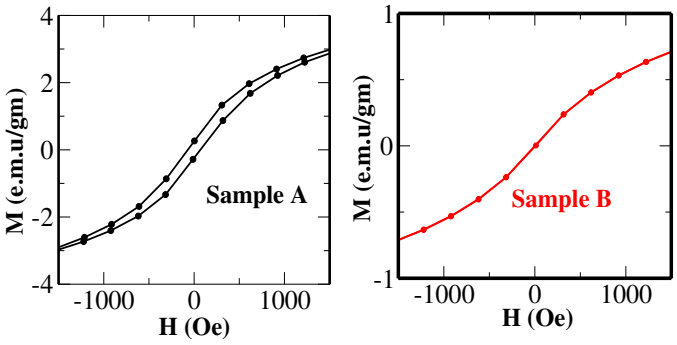

Figure 3.1: Room temperature dc M-H measurement of interacting sample A and noninteracting sample B. The solid lines are drawn through the experimental points, indicated by dots.

is well known that dipolar interactions, being long-ranged, anisotropic and alternating in the sign of interaction, can indeed lead to very complex magnetic order [54]. However, our dc M-H measurement, exhibited in Fig. 3.1, indicates that even for specimen A for which the dipolar interaction is relevant, there is no shift of the hysteresis loop, thereby implying that the bulk magnetization, for the zero applied field, is *zero*. Our interpretation is that because of the largeness of anisotropy energy as mentioned above, we are operating in the Ising limit of the dipolar interaction, for which the local field, in the mean field sense, points parallel or antiparallel to the anisotropy axis, with equal probability. The dipolar coupling can now be described by its 'truncated' form [55]:

$$\mathcal{H}_{d-d} = \sum_{ij} \gamma_i \gamma_j \hbar^2 \frac{(1 - 3\cos^2\theta_{ij})}{|\vec{r_{ij}}|^3} m_{zi} m_{zj}, \tag{3.4}$$

where γ_i and γ_j are the gyromagnetic ratio of the ith and jth particle respectively, $\vec{r}_{ij}$ is the vector distance between the 'sites' at which the two magnetic particles are located, θ_{ij}

is the angle between $\vec{r}_{ij}$ and the anisotropy axis and m_{zi} is the (giant) magnetic moment for the i^{th} nanoparticle along the direction of anisotropy axis (i.e. Z). Given the fact that m is proportional to the volume V of the particle, Eq. (3.4) can be rewritten as

$$\mathcal{H}_{d-d} = \mu^2 V^2 \sum_{ij} \gamma_i \gamma_j \hbar^2 \frac{(1 - 3\cos^2\theta_{ij})}{|\vec{r_{ij}}|^3} \cos\Phi_i \cos\Phi_j, \tag{3.5}$$

where μ is the magnetic moment per unit volume and Φ has the same definition as in Eq. (3.2). The interaction in Eq. (3.5), along-with that given in Eq. (3.2), is quite complicated to treat in detail. For the purpose of this chapter we invoke a mean field theory in which each magnetic nanoparticle is visualized to be embedded in an effective medium which creates a local magnetic field at its site. Thus in this approximation, $\mathcal{H}_{d-d}$ is replaced by its mean field(MF) form :

$$\mathcal{H}^{MF}_{d-d} = \gamma\hbar\mu^2 V^2 \cos\Phi \sum_{j} \gamma_j \hbar \frac{(1 - 3\cos^2\theta_{ij})}{|\vec{r_{ij}}|^3} \langle\cos\Phi_j\rangle, \tag{3.6}$$

wherein the angular brackets $\langle ... \rangle$ represent a thermal average. Further, in accordance with our assumption about the largeness of the anisotropy energy, $\cos\Phi$ can be replaced by a two-state Ising variable σ :

$$\mathcal{H}^{MF}_{d-d} = \gamma\hbar\mu^2 V^2 \sigma \sum_{j} \gamma_j \hbar \frac{(1 - 3\cos^2\theta_{ij})}{|\vec{r_{ij}}|^3} \langle\sigma_j\rangle, \tag{3.7}$$

In line with this approximation each particle can be viewed to be subjected to a local magnetic field H such that

$$\mathcal{H}^{MF}_{d-d} = \mu V \sigma H, \tag{3.8}$$

$$H = \mu\Lambda V \langle\sigma\rangle, \tag{3.9}$$

where Λ is a parameter that subsumes all the other constants. Note that we have dropped the suffix j on σ, implying that we consider the embedding medium to be homogeneous. Within the proposed self-consistent mean field theory, H can be expressed as

$$H = \mu\Lambda V \tanh(\frac{\mu V H}{k_B T}). \tag{3.10}$$

Note that Eq. (3.10) admits both positive and negative solutions for H, in accordance with our discussion preceding Eq. (3.4). Further, within the present approximation in

which Φ is restricted to the value 0 and π, the anisotropy energy in Eq. (3.2) dose not figure in the expression for H. We now turn our attention to relaxation kinetics. The dichotomic Markov process, mentioned in the paragraph preceding Eqs. (3.4 - 3.5), yields the following set of rate equations for the number of magnetic particles with a specific orientation of their magnetization:

$$\frac{d}{dt}n_0(t) = -\lambda_{0\to\pi}n_0(t) + \lambda_{\pi\to 0}n_\pi(t), \tag{3.11}$$

$$\frac{d}{dt}n_\pi(t) = \lambda_{0\to\pi}n_0(t) - \lambda_{\pi\to 0}n_\pi(t), \tag{3.12}$$

where the subscripts on n indicate the two allowed values of Φ. Solving Eqs. (3.11) and (3.12), we may derive for the time-dependent magnetization M(t):

$$\begin{aligned} M(t) \quad &\equiv V\mu[n_0(t) - n_\pi(t)] \\ &= M(t=0)\exp(-\bar{\lambda}t) \\ &+\mu VN\frac{\Delta\lambda}{\bar{\lambda}}[1-\exp(-\bar{\lambda}t)]. \end{aligned} \tag{3.13}$$

In Eq. (3.13),

$$N = n_0 + n_\pi, \tag{3.14}$$

which is a constant,

$$\bar{\lambda} = \lambda_{0\to\pi} + \lambda_{\pi\to 0}, \tag{3.15}$$

and

$$\Delta\lambda = \lambda_{\pi\to 0} - \lambda_{0\to\pi}. \tag{3.16}$$

The expressions for the rate constants necessitate now a generalization of Eq. (3.3) in view of the dipolar interaction, and are given by:

$$\lambda_{0\to\pi} = \lambda_0 \exp\Big[-\frac{KV}{k_BT}\Big(1+\frac{H\mu}{2K}\Big)^2\Big]\Big(1+\frac{H\mu}{2K}\Big), \tag{3.17}$$

and $\lambda_{\pi\to 0}$ is obtained by switching the sign of H. We conclude this section by reiterating a few remarks on the theory presented here. First, we have assumed at the outset that the anisotropy is large, a very good assumption in the context we believe, which has allowed us to approximate a continuous stochastic process by its discrete version. The anisotropy barrier does not appear in equilibrium properties (cf. Eq. (3.10)) but does

strongly influence relaxation kinetics (cf. Eqs. (3.17) and (3.18)). Our second remark concerns the dipolar interaction, which is treated in mean field theory. This interaction, though weak, has a significant contribution to the relaxation effects (cf. Eqs. (3.17) and (3.18)). In particular, and in the context of magnetic nanoparticles, the relaxation rates acquire a V^2-dependent term in the exponent (see also Eqs. (3.9) and (3.10)) in addition to an effective temperature-dependent tan-hyperbolic term.

3.3 Polydispersity-linked Memory Effects

Having discussed the effect of slowing down of relaxation due to the weak interaction between magnetic nanoparticles in terms of the theory developed in the previous section, we now focus our attention to another important attribute, viz., the volume-distribution of the nanoparticles. We show that such a distribution leads to striking memory effects in our low-temperature DC magnetization measurements on the $NiFe_2O_4$ nanomagnetic particles embedded in SiO_2 matrix.

The magnetization measurements are carried out in accordance with the following cooling and heating protocol. At T=300K ($T = T_\infty$), a small magnetic field ($h = 50$ Oe) is applied and the magnetization(M) measured. Keeping the field on, the temperature(T) is lowered continuously at a steady rate to T_n and M is simultaneously measured upto the temperature T_n. Thus one obtains M versus T in the cooling regime ($T_n \leq T \leq T_\infty$). At T_n the field is switched off and the drop of M is monitored for several (≈ 4) hours. Subsequently, the magnetic field is *switched* back on and M(T) versus T is mapped in the cooling regime($T_{n-1} \leq T \leq T_n$). At T_{n-1} the field is switched off again and the process of measurement repeated, until the lowest temperature T_0 is reached. Thus, one obtains field-cooled response and zero-field relaxation of the magnetization as a function of temperature. At the end of the cooling cycle, at T_0, the field is turned on and M(T) monitored as the system is heated from T_0 through T_{n-2},T_{n-1},T_n and eventually to T_∞, the magnetic field remaining on throughout. Our results are shown in Fig. 3.2, for sample A and sample B. The heating path surprisingly shows wiggles in M(T) at all the T steps T_{n-2},T_{n-1},T_n where h was earlier switched off during cooling, apparently

retaining a memory of the temperature steps at which the cooling was arrested. One

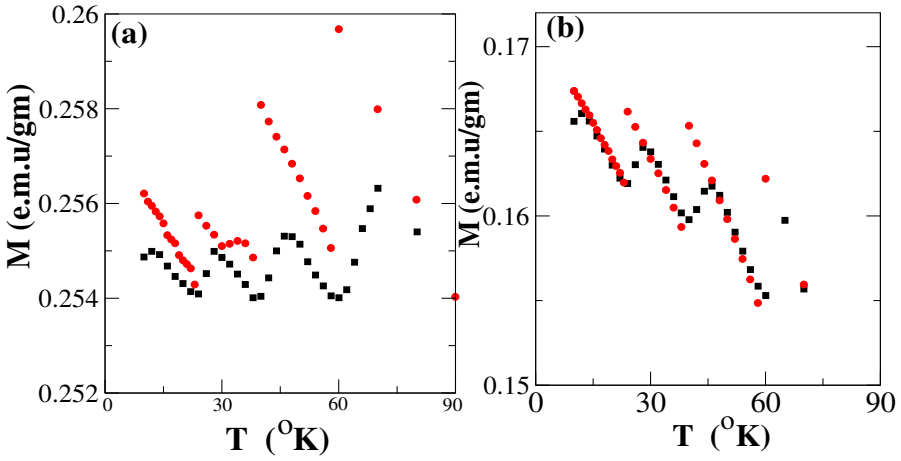

Figure 3.2: Experimental M(T) curves during cooling (∘ red) in a small magnetic field $h = 50$ Oe and zero-field heating (□ black) for the (a) interacting and (b) non-interacting samples showing prominent memory effects. A constant heating/cooling rate of 2K/min was maintained except at 60K, 40K and 20K where the cooling was arrested for 4 h duration at each temperature during which time h was switched off.

tantalizing aspect of our results is that memory effects are more prominent for sample B than for sample A, although in the latter the average inter-particle distance is smaller and hence the dipolar interaction non-negligible. Recently Sun *et al* [51] have reported very similar history dependent effects in the magnetization measurements of a monolayer of sputtered permalloy($Ni_{81}Fe_{19}$) clusters on a SiO_2 substrate. These authors attribute the disparate cooling and heating histories to aging and concomitant memory effects found in a spin glass phase [56]. Spin glass transitions are known to occur due to disorder and frustration in dilute magnetic alloys that are characterized by a complicated free energy landscape with deep valleys and barriers [57] . Strongly non-equilibrium memory dependent behavior ensues as a result of the system getting trapped in a deep valley such that the relaxation time(τ) for deactivation becomes long compared to experimental time

scales of measurement [58].

Our interpretation of the results shown in Fig. 3.2 is very different from that of [51]. We demonstrate below that the observed phenomena are *not* connected to complicated spin glass type interactions but can be simply attributed to a superposition of relaxation times, arising from particle size distribution, as it were, in *noninteracting* single-domain magnetic particles. Experimentally it is known [52] that nanoparticle sizes are usually distributed according to a log-normal distribution. However, we show below that the exact form of the distribution is irrelevant for explaining the memory effect. In fact, in order to keep the analysis simple and to obtain a clear understanding of the physics it is sufficient to take a sample size distribution consisting of two delta function peaks so that there are only two kinds of particles "large" (volume V_1) and "small" (V_2). Correspondingly we have only two relaxation times $\tau = \tau_1$ and τ_2 in our model, if we remember that(cf. Eqs. (3.17) :

$$\tau(V) = \exp\Big[-\frac{KV}{k_BT}\Big(1+\frac{H\mu}{2K}\Big)^2\Big]\Big(1+\frac{H\mu}{2K}\Big). \tag{3.18}$$

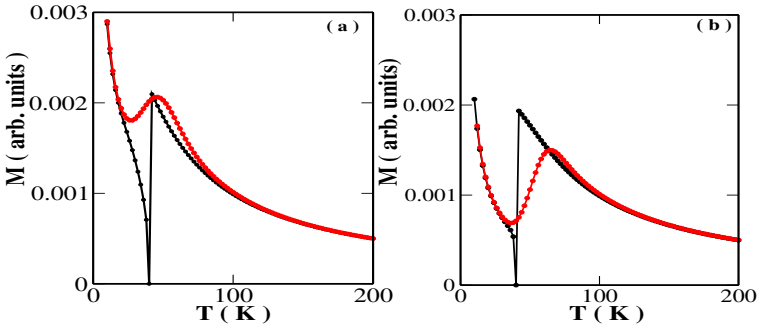

The interpretation of the observed results hinges on the premise that the time τ_1 is much larger than the measurement time while τ_2 is much smaller, at the lowest measured temperature (T_0). Both τ_1 and τ_2 are expected to be smaller than the measurement time at the highest temperature T_∞. Therefore, in the intermediate temperature domain ($T_0 \leq T \leq T_\infty$), the small particles equilibrate rapidly, thus showing superparamagnetic viscosity [50] while the large particles are 'blocked'. This is observed in Fig. 3.3(c) where we have plotted computer simulations of M(T) separately for the two sets of interacting

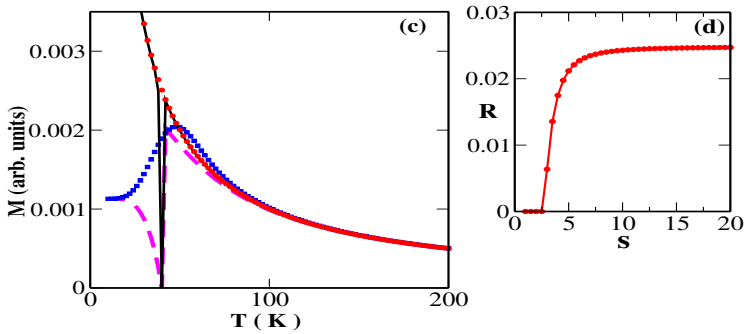

Figure 3.3: Simulated M (arbitrary unit) vs. T curves during cooling (solid black) and heating (dashed red) for the (a) interacting and (b) non-interacting cases: The curve (c) shows the various contributions to the total magnetization of interacting sample(A) coming from the (i) fast particles during the cooling cycle (black solid line), (ii) fast particles during the heating cycle (red filled circle), (iii) slow particles during the cooling cycle (magenta dashed line) and (iv) slow particles during the heating cycle (blue square). The theoretical curves (a) - (c) have been calculated using a double delta function distribution of particle sizes. Curve (d) shows a plot of the recovery parameter R (see text) as a function of the width(s) of a Gaussian particle size distribution.

particles under the same cooling and heating regimens. Here we choose the temperature T^* at which h is switched off such that the blocking temperatures [48, 49] corresponding to the two different particle sizes flank T^*. The simulations are based on rate theory calculation for the time dependent magnetization given in the previous section. When h is zero, both sets of particles relax to M=0. However, when h is turned on, particles 1 are blocked(M=0) while 2 show facile response. As T is increased again, M for particles 2 decreases with T while M for particles 1 initially increases before dropping off. The resultant graph is a superposition (see Fig. 3.3 (c)) of a monotonically decreasing curve and a hump, thus producing a wiggle. This effect is seen only when the temperature of arrest is in-between the two respective blocking temperatures, in conformity with the findings of [52]. We have performed measurements on the same system but now with increased inter-particle separation ($\simeq$15nm.) (see Fig. 3.2(b)), the simulation results of which are shown in Fig. 3.3(b).

The resultant interaction effect due to dipole-dipole coupling, not considered in [52], is

also quite distinct from the quenched-in disorder mediated interactions proposed in [51]. As described earlier, the effect of interaction, within a mean-field picture, is incorporated by adding a term proportional to V^2 in the exponent of $\tau(V)$ (cf. Eqs. (3.9) and (3.10)). Thus, even small particles (V_2) can now have τ_2 *larger* than the measurement time. This becomes more prominent at lower temperatures. Therefore, the blocking temperatures for both particles 1 and 2 are now shifted to higher T, thereby causing the wiggles to disappear. This is consistent with the results of Fig. 3.2 which show that the memory effects are *stronger* for the non-interacting particles. We conclude then that the unexpected wiggles seen in the cooling and heating cycles of M(T) versus T have much less to do with interaction effects but more to do with polydispersity of the sample.

How crucially does the nature of the particle size distribution function affect the magnetization recovery during the zero field heating cycle ? In order to answer this question we first quantify the memory effect by defining a parameter,

$$R = \Theta\Big(\frac{dM}{dT}\Big)|_{T=T_n}\frac{dM}{dT}, \tag{3.19}$$

where $\Theta(x)$ is the Heaviside step function. The parameter R measures the positive slope of the M(T) curve during zero field heating. We have calculated R using a Gaussian size distribution centered at $V = V_0$ and with width s. Our results for R are shown in Fig. 3.3(d) for a particular choice of V_0 as a function of s. We observe that R increases with the width of the distribution and saturates quickly. In this regime, R is almost independent of V_0 and accordingly, the detailed nature of the distribution. We conclude that the memory effects will be best seen in samples with a dilute dispersion of particles but a very wide (flat) distribution of sizes. Indeed in this limit the relaxation is known to be prominently dominated by magnetic viscosity characterized by a logarithmic relaxation in time [51]. Not surprisingly, a logarithmic relaxation has been observed in the experiments of Sun *et al.* although the interpretation offered is different from ours [51].

Our interpretation of the M vs. T data is further substantiated by our earlier reported results (in Fig. 3.1) of hysteresis measurements and thereby coercivity estimation for both the interacting sample A and non-interacting sample B. Clearly, for sample B the relaxation times are shorter than the measurement time, at 300K. Thus, there is no hysteresis loop and the coercivity (measured by the width along the abscissa on the zero-magnetization line) is also zero. On the other hand, for sample A, we observe a non-zero

coercivity even at 300K due to the slowing down of relaxation because of the presence of an additional term proportional to V^2 in the exponent of $\tau(V)$ as mentioned above.

Next we repeat the above measurements down to 4K, using a SQUID magnetometer. The

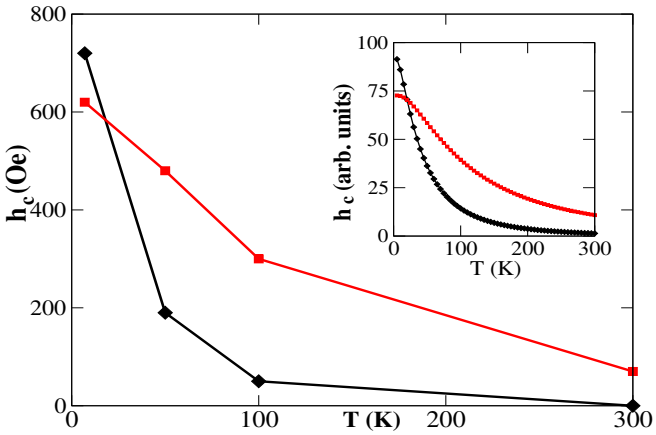

Figure 3.4: Coercivity(h_c) as a function of temperature for the interacting (□ red) and non-interacting (◇ black) samples. The corresponding curves (h_c in arbitrary unit) obtained from our theory assuming a double delta function particle size distribution is shown in the inset.

coercivity(h_c) is plotted as a function of temperature(T), in Fig. 3.4. Because relaxation slows down for both sample A and sample B, h_c increases with decrease of T (Fig. 3.4). The coercivity of the interacting sample A is larger than that of the non-interacting sample B for temperatures greater than 25K. However, at T=25K a surprising *crossover* is detected, where the coercivity for sample B shoots above that for sample A. We suggest that the reason for this behavior is that the term H in the exponent of $\tau(V)$ in Eq.(3.17) is replaced by H+δH, where H is the applied field and the mean field δH arises from interaction (cf. Eq. (3.10)):

$$\delta H = \mu V \Lambda \tanh(\frac{\mu V(h+\delta H)}{k_B T}). \tag{3.20}$$

The tanh term augments the V^2 term in the exponent of $\tau(V)$ below 25K, making the larger particles relax so slowly that they don't respond to H at all. Therefore, the larger particles are 'frozen out' from further consideration, making the mean relaxation time in

the interacting case even smaller than that for the non-interacting case. This somewhat nonintuitive conclusion is further confirmed by our simulated coercivity computation, shown in Fig. 3.4 (inset).

3.4 Summary and Conclusions

We have presented here both theoretical and experimental results and their inter-comparison. Our main focus has been to analyze how the relaxation and response behavior of magnetic nanoparticles is influenced by their mutual interaction as well as polydispersity of particle sizes. The theory presented in section 2.2 is based on the simplifying assumption of large uniaxial anisotropy energy vis-a-vis the thermal energy. A further simplifying assumption has been invoked in treating the interaction due to dipolar coupling between magnetic nanoparticles within a mean field approximation. The symbiotic relationship of polydispersity and interaction in influencing the relaxation phenomena has been brought out through low-temperature magnetization and coercivity data. We have demonstrated that just a bimodal distribution of particle size, in which one set of particles remains frozen in its response behavior while the other set exhibits magnetic viscosity, suffices to interpret dramatic memory effects seen in cooling and heating cycles of the magnetic response. These memory effects are quite akin to and often interpreted to be due to much complex spin glass phenomenon which is characterized by fascinating aging effects.
In conclusion, the strong history dependent effects seen in magnetization and coercivity measurements in $NiFe_2O_4$ magnetic nanoparticles have been interpreted as being due to arrested Neel relaxation. Our model has been simplified by choosing just two volumes of the particles, on either side of the 'blocking' limit. Further corroboration of the proposed mechanism has been achieved by performing measurements on an interacting system. Our results suggest that either by tuning the interaction (through changing inter-particle distance) or by tailoring the particle size distribution, these nanosized magnetic systems can be put to important application in memory devices. In particular, a flat volume distribution can be of great utility than a monodispersed distribution with a single sharp peak.

Chapter 4

Memory in Nanomagnetic Systems: Superparamagnetism Versus Spinglass Behavior

4.1 Introduction

As discussed in Chapter 3, though the subjects of both superparamagnetism and spinglasses are quite old and well studied [19, 21, 24, 25, 49, 59, 60], yet they have been rejuvenated in recent years in the context of fascinating memory and aging properties of nanomagnets. These properties, which are believed to be of great practical usages, have been recently investigated in a large number of experiments on magnetic nanoparticles [52,61-67], as reported earlier in the previous chapter. The observed slow dynamical behaviour has been variously interpreted, based on the paradigm of either superparamagnet or spinglass, sometimes even obscuring the difference between the two distinct physical phenomena. The purpose of this chapter is to reexamine some of the data, others' as well as our own, and critically assess the applicability of the physics of either superparamagnets or spinglasses and occasionally, even a juxtaposition of the two. Our main point is, spinglasses are marked by Complexity, arising out of two separate attributes — Frustration and Disorder. While the manifested properties, such as stretched exponential relaxation and concomitant aging effects, can also occur due to 'freezing' of superparamagnetism, especially in a polydisperse sample, the physics of spinglasses is naturally much richer than that of superparamagnets. A discernible experimental signature of superparamagnetism versus spinglass behavior seems to be the magnitude of the field-cooled (FC) magnetization memory effect that is significantly larger for the interacting glassy systems than the one in non-interacting superparamagnetic particles [68]. Therefore, invoking spinglass

physics in interpreting data on the slow dynamics of nanomagnets can sometimes be like 'killing a fly with a sledge hammer', especially if a simpler interpretation on the basis of superparamagnetism is available. We explore such situations in this chapter.

Superparamagnetism was discussed quite early by Frenkel and Dorfman and later by Kittel, as a property arising out of single-domain behavior when a bulk ferromagnetic or an antiferromagnetic specimen is reduced to a size below about 50 nm [19]. For such a small particle-size the domination of surface to bulk interactions yields a mono-domain particle inside which nearly 10^5 magnetic moments are coherently locked together in a given direction, thus yielding a giant or a supermoment. Clearly, for this to happen, the ambient temperature must be much less than the bulk ordering temperature, so that the integrity of the super moment is maintained. However, as Neel pointed out, in the context of magnetic properties of rocks in Geomagnetism, the direction of the supermoment is not fixed in time [24]. Indeed, because of thermal fluctuations, this direction can undergo rotational relaxations across an energy-barrier due to the anisotropy of the single-domain particle, governed by the Neel relaxation time (Eq. (3.1)).

As mentioned in Chapter 3, the transition from superparamagnetism to frozen-moment behavior occurs at a temperature, referred to in the literature as the blocking temperature T_b, defined by

$$\tau_E = \tau_0 \exp\big(\frac{KV}{k_B T_b}\big). \tag{4.1}$$

When the measurement temperature T is less than T_b the magnetic particles are blocked whereas in the other extreme they display facile response to applied fields. Therefore, we emphasize that even within a single particle picture, *sans* any form of inter-particle interactions, such as in a dilute nanomagnetic specimen, one can obtain apparently intriguing effects such as 'stretched exponential' relaxation simply because of size distributions. The latter will be shown to be responsible for much of the data on slow relaxations in nanomagnets.

Turning now to spinglasses, historically the phenomenon was first observed in dilute alloys such as $Au_{1-x}Fe_x$ (or $Cu_{1-x}Mn_x$) in which magnetic impurities Fe (or Mn) in very low concentrations were "quenched-in" from a solid solution with a host metallic system of Au (or Cu) [38]. The localized spin is coupled with the s-electron of the host metal which itself interacts with the other conduction electrons via what is called the

Ruderman-Kittel-Kasuya-Yoshida (RKKY) Hamiltonian, thereby setting up an indirect exchange interaction between the localized moments. Because the coupling constant of the exchange interaction, in view of the RKKY coupling, alternates in sign (between ferro and antiferromagnetic bonds), the system is 'frustrated'. Thus the ground state is highly degenerate yielding a zero-temperature entropy. An additional effect is due to disorder. Because the dilute magnetic moments are quenched-in at random sites, the exchange coupling-strengths are randomly distributed. The dual occurrence of frustration and disorder has led to novel concepts in the Statistical Mechanics of spinglasses such as configuration-averaging, replica-techniques (for computing the free energy), broken-ergodicity, etc. [69]. Experimentally, spinglasses are characterized by a 'cusp' in the susceptibility and stretched exponential relaxation of time-dependent correlation functions [38]. It is no wonder then that spinglasses also exhibit slow dynamics with associated memory and ageing effects, albeit the root causes are much more complex than a system of polydisperse, noninteracting single-domain nanomagnetic particles, discussed earlier. Indeed spinglasses, because of their complexity, have been employed as paradigms for studying real structural glasses, an unresolved problem of modern condensed matter physics [70].

Given this background on two distinct physical phenomena (and yet manifestly similar properties) of superparamagnets and spinglasses, a natural question to ask is: can there be spinglass-like physics emanating from a collection of single-domain nanomagnetic particles embedded in a non-metallic, non-magnetic host? The answer is clearly an YES when the system is no longer a diluted one such that the supermoments start interacting via dipole-dipole coupling. Because the dipolar interaction (like the RKKY-mediated exchange interaction) is also endowed with competing ferro and antiferromagnetic bonds [71], as well as randomness due to random locations of the magnetic particles, all the attributes of spinglasses can be simulated in interacting single-domain particles. This will be analyzed below.

4.2 Superparamagnetic Slow Dynamics

Recently Sun et al have made a series of measurements on a permalloy ($Ni_{81}Fe_{19}$) nanoparticle sample which demonstrate striking memory effects in the dc magnetization [51]. These involve field-cooled (FC) and zero-field cooled (ZFC) relaxation measurements under the influence of temperature and field changes. We have also observed very similar memory effects in $NiFe_2O_4$ magnetic particles in a SiO_2 host [62]. More recently Sasaki et al [52] and Tsoi et al [63] have reported similar results for the noninteracting (or weakly interacting) superparamagnetic system of $\gamma - Fe_2O_3$ nanoparticles and ferritin (Fe-N) nanoparticles respectively. Further, to understand the mechanisms of the experimental approach of Sun et al, Zheng et al [64] replicated the experiments on a dilute magnetic fluid with Co particles and observed similar phenomena. In this section we present a comparison of simulated results with all the above mentioned experimental observations on the basis of a simple two-state noninteracting model plus a log-normal distribution of particle size, developed earlier in Chakraverty et al [62].

We begin our discussion from the most basic and well known protocol, viz. the zero field-cooled magnetization (ZFCM) and the field-cooled magnetization (FCM). The analysis is based on the time-dependent magnetization, given by the formula :

$$\bar{M}(t) = \int dV P(V) M(V,t), \tag{4.2}$$

where $P(V)$ is a log-normal distribution of volume V :

$$P(V) = \frac{1}{\gamma V\sqrt{2\pi}} \exp\Big[- \ln \frac{V^2}{2\gamma^2}\Big], \tag{4.3}$$

with γ being a fitting parameter. The rate theory expression for $M(V,t)$ is given in Eq. (3.13). In the experimental procedure the external field has been taken to vary between 50 Oe to 100 Oe. The cooling or heating rate is about 2K/min. The temperature varies between 300 K to 4 K. In all the simulations, the results of which are presented below, we have used a log-normal distribution of particle sizes wherein the parameter γ is set to 0.5. The average anisotropy energy $K\bar{V}$ is chosen as the unit of energy as well as that of temperature by setting $k_B = 1$ and $\bar{V} = \exp(\gamma^2/2)$. The volume V is measured in units of the average volume $\bar{V}$ and the magnetic field in units of $\frac{K\bar{V}}{\mu}$. The heating or cooling rate

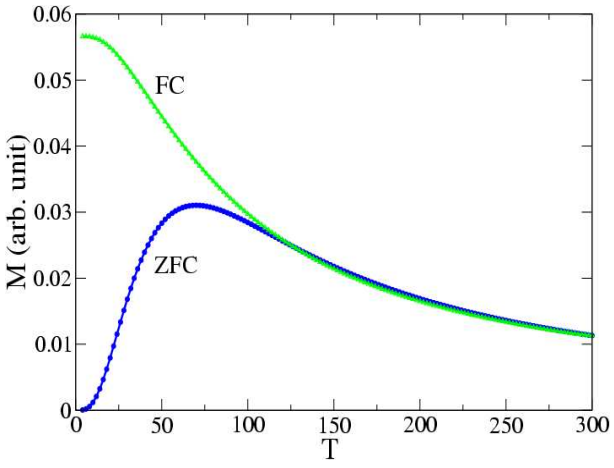

Figure 4.1: Numerically calculated dc magnetization for the FC and ZFC processes.

is set to $r = 2.4 \times 10^{12}\tau_0$ per temperature unit. Because τ_0 for nanoparticles is around 10^{-9} sec and a typical experimental time window is about 10 sec, we have investigated the predictions of our model in the time window $10^{10}\tau_0$. After doing the simulation we re-express the temperature and time data in K and sec for the purpose of plotting.
In previous studies, Sasaki et al [52], Tsoi et al [63] and Zheng et al [64] have numerically reproduced only the ZFC and FC relaxation measurements of Sun et al with temporary cooling. But in this chapter we have successfully reproduced all other relaxation measurements of Sun et al [51] based on our simple two state model. Figure 4.1 shows the simulated FC-ZFC curves that match well with the experimental results of Sun et al [51] (Fig. 4.1). The ZFCM has a peak at $T_{max} = 72K$, which corresponds to the blocking temperature T_b. The magnetization of the FC curve continues to increase with decreasing temperature as would be expected for a system in thermal equilibrium. The two curves depart from one another at a temperature higher than T_{max}. Figure 4.2 shows the M-H curve below and above the blocking temperature T_b, indicating hysteresis below T_b.

The most striking experimental observation of Sun et al is the memory effect in the dc magnetization obtained from the following procedure. The sample is cooled in 50 Oe field at a constant cooling rate of 2K/min from 200K (T_H) to 10K (T_{base}). After reaching T_{base}, the sample is heated continuously at the same rate to T_H. The obtained M(T) curve is the normal FC curve which is referred to as the reference curve. Then the sample is

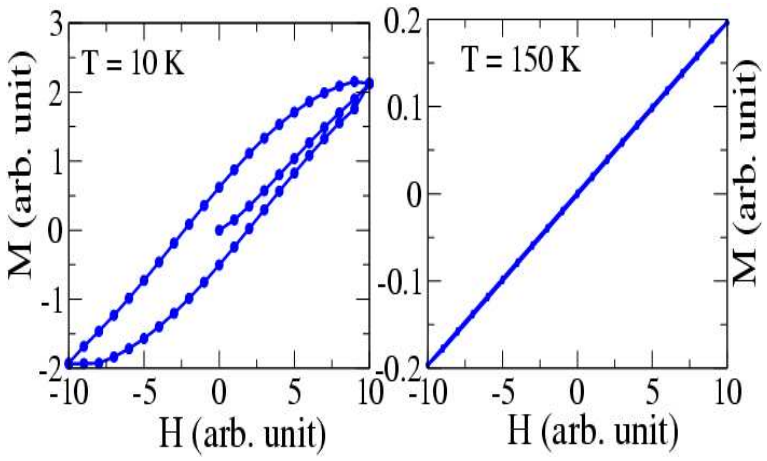

Figure 4.2: Numerically calculated M Versus H curve below and above T_b.

cooled again at the same rate, but the cooling is arrested three times (at T = 70, 50 and 30K) below T_b with a wait of $t_w = 4h$ at each stop. During t_w, the applied field is also turned off to let the magnetization decay. After each stop and wait period, the 50 Oe field is reapplied and cooling is resumed. The cooling procedure produces a step like M(T) curve. After reaching the base temperature, the sample is warmed continuously at the same rate to T_H in the continual presence of the 50 Oe field. Surprisingly, the M(T) curve obtained in this way also shows the step like behavior. Similar memory effects, following the same protocol were seen by us in $NiFe_2O_4$ sample in which the magnetic particles were embedded in a host SiO_2 matrix [62]. Although the effects were earlier explained in terms of a bimodal distribution of particle size [62], a log normal distribution in the simulation also indicates satisfactory agreement with experiments, as seen in Fig. 4.3.

In the Sun et al measurements [51] for magnetic relaxation with temporary cooling and field change for the ZFC method the sample is cooled to $T_0 = 30K$ in zero field. Then a 50 Oe field is applied and the magnetization is measured for a time t_1. After t_1, the sample is quenched to temperature $T = 22K$ in the absence of an external field and the magnetization is recorded for a time t_2. Finally the temperature is returned back to T_0 and the field is turned on again. The magnetization is measured for a time t_3.

In Fig. 4.4 we show our corresponding numerically simulated results. When a field of 50

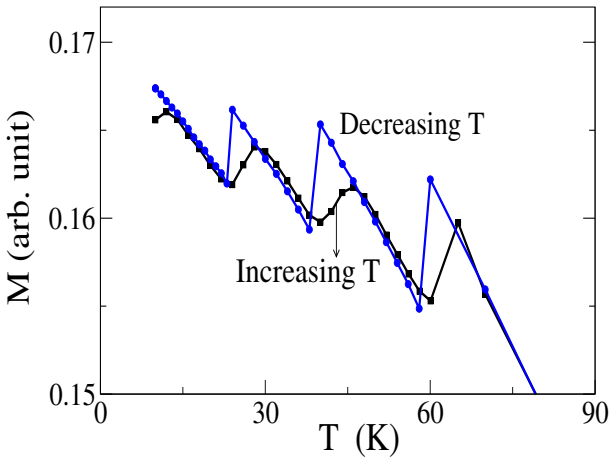

Figure 4.3: Numerically simulated memory effect observed in dc magnetization curves.

Oe is applied the magnetization immediately reaches a certain value, because the particles with $T_b \leq 30K$ equilibrate rapidly. Then a slow logarithmic response begins which is due to the energy distribution of the particles [74]. Now as the field is turned off, we observe a sharp jump in $M(t)$ due to those particles with $T_b \leq 22K$ which reach their equilibrium state at $T = 22K$ and hence do not contribute to the magnetization. However the particles with $T_b > 30K$ are not in equilibrium and relax extremely slow at $T = 22K$, so we get a constant curve during t_2. Now as the field is turned on again and the temperature of the sample is increased to $T = 30K$, the particles with $T_b \leq 30K$ and those flipped during time $t_1 + t_2$ come back to the new equilibrium state which is same as that pertaining before quenching. Therefore the relaxation in t_3 is the continuation of that during the time t_1.

In the FC magnetic relaxation with temporary cooling and field change the sample is cooled to $T_0 = 30K$ in a 50 Oe field and then the relaxation is measured for a time t_1 after the field is cut-off. The field is turned on again and the sample is cooled to $T = 22K$ and the magnetization is recorded for a time t_2. Finally the temperature is turned back to T_0 and the field is switched off again. The relaxation is now measured for a time t_3.

We represent our numerical results for the same protocol in Fig. 4.5. When the field is cut-off the particles with $T_b \leq 30K$ do not contribute to the magnetization . After t_1,

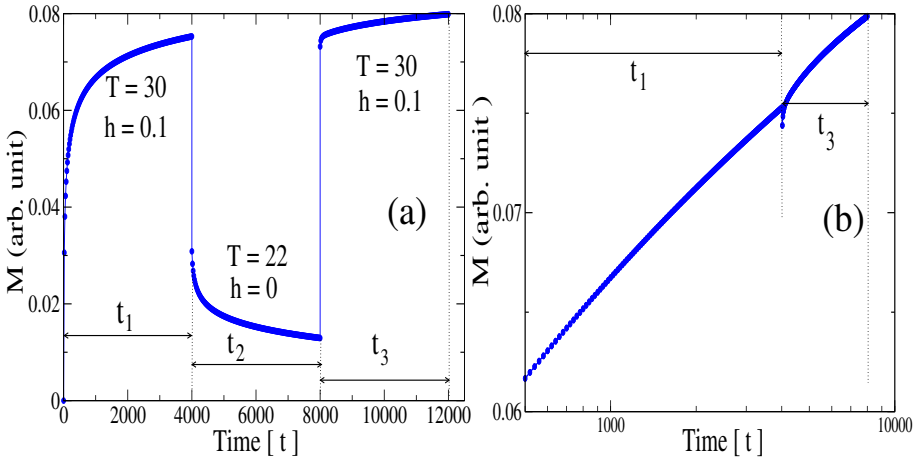

Figure 4.4: (a) Numerically simulated ZFC relaxation curves with temporary cooling and field change; (b) the same data vs the total time spent at 30 K on a logarithmic scale.

when the sample is quenched to $22K$ and the field is turned on there is naturally a sudden jump in the magnetization due to the particles with $T_b \leq 22K$ which have much higher magnetization than the value just before quenching. As discussed earlier the particles with $T_b > 30K$ are not in equilibrium and their relaxation is very slow at $T = 22K$, which explains an almost constant curve during t_2. After t_2, the field is turned off, and the temperature is turned back to T_0. Naturally, the magnetization jumps down, because the particles with $T_b \leq 30K$ reach a new equilibrium state which has almost zero magnetization immediately following the field and temperature changes and the system returns back to its state prevailing before quenching.

Finally, Sun et al have studied magnetic relaxation after a temporary heating (instead of temporary cooling) from 30K to 38K which do not exhibit any memory effect. After temporary heating, when temperature returns back to T_0, the system does not come back to its previous state before heating. Sun et al suggested that this asymmetric response with respect to negative/positive temperature cycling is consistent with a hierarchical model of the spin-glass phase. However, we have numerically reproduced the same results as that of Sun et al based on our two-state independent particle model, as shown in Fig. 4.6. No memory effect appears after positive heating which can be explained as follows. In the FC method the sample is cooled to $T_0 = 30K$ in the presence of a 50 Oe field and

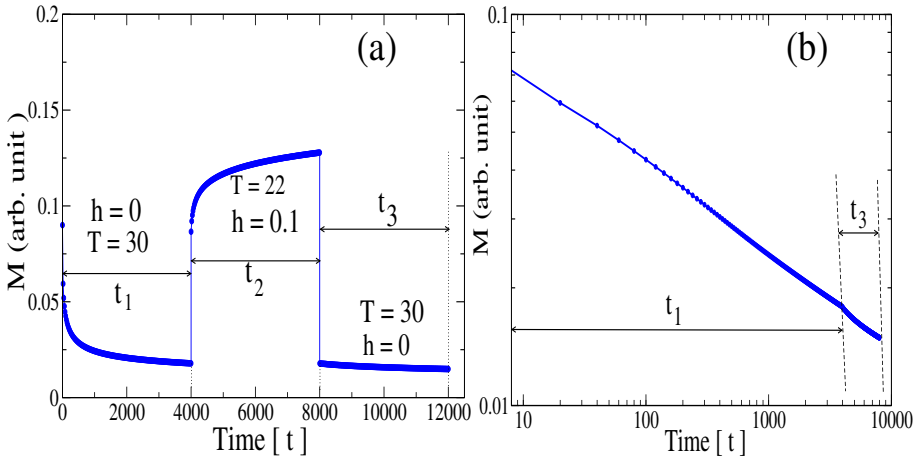

Figure 4.5: (a) Numerically simulated FC relaxation curves with temporary cooling and field change; (b) the same data vs the total time spent at 30 K on a logarithmic scale.

then the field is cut-off and the relaxation is measured for a time t_1. So the magnetization decreases with time for a time t_1. Now as the temperature is increased all the particles with $T_b \leq 38K$ respond to this temperature change and relax to the new equilibrium state. Since thermal agitation increases with the increase of temperature, the magnetization decreases further for the time t_2. As the temperature returns back to $T = 30K$, the particles with $T_b > 30K$ are unable to respond to this temperature change. Thus the particles with $T_b \leq 30K$ actually follow the path during time t_2 rather than t_1. Because all the particles which had flipped during the time $t_1 + t_2$ cannot return back to their previous state as that before heating, no memory effect is observed.

In the ZFC method the sample is cooled to T_0 in the absence of an external field and then a 50 Oe field is turned on and relaxation is measured for a time t_1, yielding a finite magnetization, for particles with $T_b \leq 30K$. Then a slow logarithmic relaxation begins which is due to the energy distribution of the particles. As the sample is further heated to $T = 38K$, all the particles with $T_b = 38K$ respond to this temperature change. Thus the logarithmic relaxation is continued but there is a jump in magnetization, because the particles with $T_b \leq 38K$ and those flipped during t_1 reach a new equilibrium state. As the temperature of the sample is returned back to $T = 30K$ thermal agitation is reduced, so there is a jump in magnetization. But now only the particles with $T_b > 30K$ are allowed

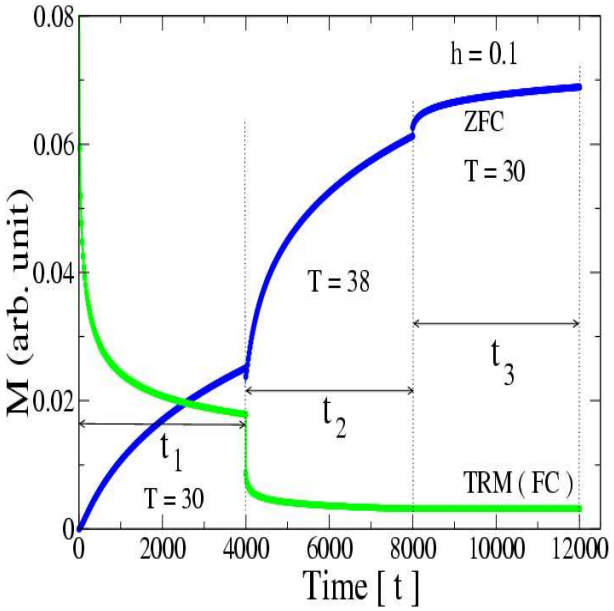

Figure 4.6: Numerically simulated FC and ZFC relaxation curves with temporary heating.

to relax and their relaxation is very slow at $T = 30K$, so we obtain an almost flat curve. We conclude this section by underscoring that our simulations based on the simple two-state noninteracting model reproduce all the features of the memory effects observed by Sun et al in the Permalloy ($Ni_{81}Fe_{19}$). Secondly, positive heating does not yield memory effect whereas temporary cooling does. So there is an asymmetric response with respect to negative/positive temperature cycling. This asymmetry is due to the fact that after temporary cooling only smaller nanoparticles are able to respond to the temperature or field change and relax to the new equilibrium state. The larger nanoparticles are frozen. Upon returning to the initial temperature or field value, the smaller particles rapidly respond to the change such that this new state is essentially the same as that before the temporary cooling, and the larger nanoparticles are now able to resume relaxing to the equilibrium state. This results in a continuation of the magnetic relaxation after the temporary temperature or field change. In contrast, for positive heating, all the particles, smaller as well as bigger, are able to respond to the temperature or field change. Therefore, after returning to the initial temperature, the bigger particles do not respond at all whereas the smaller particles take time to respond, thus leading to no memory effect in

the positive heating cycle.

4.3 Spinglass Like Slow Dynamics

Time-dependent magnetization measurements suggest that dense nanoparticle samples may exhibit glassy dynamics due to dipolar inter-particle interaction [68,75-77]; disorder and frustration are induced by the randomness in the particle positions and anisotropy axis distributions. As discussed within a simple mean field theory picture, adapted to the two-state model of Chakraverty et al [62], the random dipolar interaction can be accounted for in terms of a local, self-consistent field that has the form, given earlier in Eq. (3.10). As Eq. (3.10) admits both positive and negative solutions for H, corresponding to ferro and antiferro-magnetic bonds, frustration is automatically incorporated within the simplified two-state picture. The rate constant in Eq. (3.17) is thus modified replacing H by $h + H$, where h is the applied external field and H is the mean dipolar field.

The ZFC and FC behavior (for the magnetization) for the dense magnetic nanoparticle

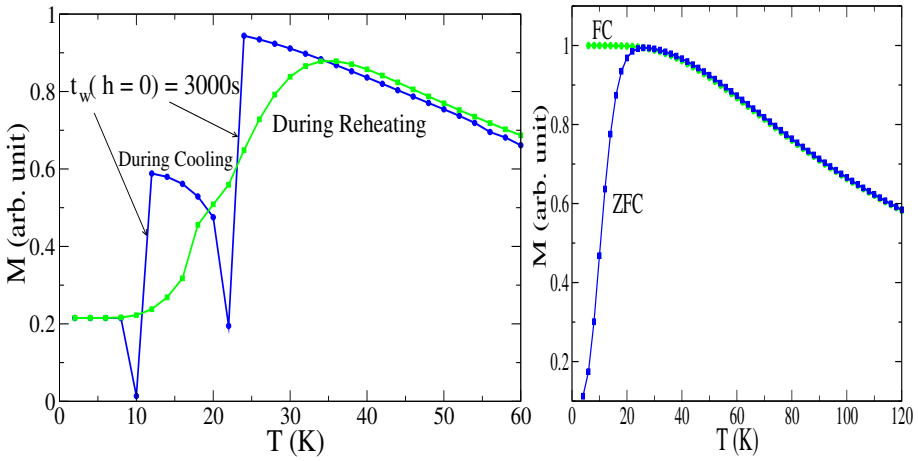

Figure 4.7: (a) Numerically simulated results for the double memory experiment (DME) for the FC method; (b) the FCM and ZFCM vs. temperature of the interacting system are shown.

system, as measured by Sasaki et al [52], is numerically simulated by us and are shown in Fig. 4.7. We observe a peak in the ZFCM which corresponds to an average blocking temperature $< T_b >$. In the superparamagnetic case the ZFC-FC curves bifurcate at a

temperature away from the peak position of the ZFCM (see Fig. 4.1). On the other hand, for the dense system the ZFCM-FCM curves bifurcate at a temperature very close to the peak position of the ZFCM. The FCM of the dense system does not increase but stays almost constant below $< T_b >$ which is the primary indicator for the glassy state [52].

In order to have a better understanding of glassy relaxation, time-dependent magne-

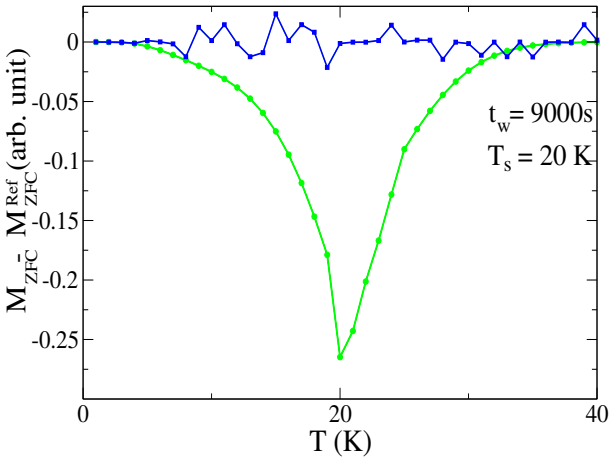

Figure 4.8: Numerically simulated results for the double memory experiment (DME) for the ZFC method in an interacting system (green circle) and in a non-interacting system (blue square).

tization studies under various heating and cooling protocols were performed by Sasaki et al [52] on dense Fe-N nanoparticle systems, by Raj Sankar et al [66] on $LaMnO_{3.13}$, by Kundu et al on $La_{0.7}Ca_{0.3}CoO_3$ [67] and by Telem-Shafir and Markovich on MICS76 sample [68]. In a double memory experiment (DME) under FC protocol the system is cooled under a field of 50 Oe. The field is cut-off during the intermittent stops of the cooling at $T = 30K$ and at $T = 40K$ for 3000 sec at each stop. After reaching the lowest temperature the magnetization measurement is repeated in the heating mode without any intermittent stop. In Fig. 4.7(a) we have shown our numerically simulated results of DME based on our interacting nanoparticle model, which have a striking resemblance to the experimental results.

Another protocol has been suggested by Sasaki et al to confirm whether the observed

memory effect is due to glassy behavior or not. In this, the sample is first rapidly cooled in zero field from a reference temperature (T_{ref}) to the stop temperature (T_s), where it is kept for 9000 sec. The cooling is then resumed down to the lowest temperature where a magnetic field is applied and the susceptibility is recorded on reheating the sample. The conventional ZFC susceptibility is also recorded. The difference between the aged and the normal ZFC susceptibility as a function of temperature was measured by Sasaki et al [52]. Figure 4.8 is our numerically simulated results, which are again very similar to that of the experiment. In the fitting procedure Eq. (3.10) has been numerically solved by choosing Λ randomly between 0 and 1, fixing h to 0.5, as before.

4.4 Superparamagnetism versus spinglass

From the above analysis it is evident that the slow dynamics in nanoparticle systems can be classified into two kinds. The first one is due to the broad distribution of relaxation times originating solely from the anisotropy energy barriers. In this non-interacting case the magnetic moment of each particle relaxes according to its individual energy barrier, that depends on the magnetic anisotropy, which in turn depends on the volume of the nanoparticle. Therefore, a distribution of particle volumes results in a distribution of energy barriers and blocking temperatures. In the second kind of slow dynamics in dense magnetic nanoparticle systems, cooperative spin-glass like dynamics, accompanied by frustration caused by the strong dipolar interactions among the particles, are the underlying reasons for memory effects. Here no unique ground state exists but rather many configurations are equally probable. The local energy barriers between these configurations are low, enabling a constant development towards equilibrium, but resulting in the inability to reach it.

Which kind of slow dynamics amongst the two scenarios, presented above, is relevant depends essentially on the concentration of the nanoparticles, at least for the data shown here. One indicator of the difference in the two kinds of slow dynamics of non-interacting and interacting nanoparticles is revealed by the field cooled (FC) magnetization measurements. As discussed earlier in Chapter 3, the extent of the memory effect can be

quantified by a parameter (R) (cf. Eq. (3.19)):

$$R = \Theta\Big(\frac{dM}{dT}\Big)_{T=T_n} \frac{dM}{dT}, \tag{4.4}$$

where, $\Theta(x)$ is the Heaviside step function and T_n is the temperature at which field is switched off. This parameter measures the positive slope of the M(T) curve during zero field heating. We have calculated R for the non-interacting and interacting cases from the figures (4.3) and (4.7-(a)) respectively. The value of R in the dense system is about eight times larger than that in the non-interacting case, implying that the magnitude of the FC magnetization memory effect does depend on the inter-particle dipolar interaction. This is in quite good agreement with the experimental results of Telem-Shafir et al [68].

In the non-interacting case, no memory effect is seen during a ZFC process (see Fig. 4.8) below (T_b), since the occupation probabilities of up and down particles are both equal to 0.5 (two-state model). So this system does not show any difference between the magnetization curves with and without intermittent stops during the cooling process. But in the interacting case there exist a huge number of states, because the local mean dipolar field is a random variable. The system goes into deeper and deeper valleys with higher and higher energy barriers as time progresses. Therefore, the energy barrier of the state in which the system is blocked depends on the ageing time of the system, when temperature is low, and the consequent higher energy barrier makes the system more reluctant to respond to an applied field. Thus the difference in the energy barrier with and without intermittent stops on cooling causes the dip in Fig. 4.8. Further the memory effect observed in the ZFC method in the interacting case can be observed over a temperature range, albeit narrow, below T_b. It can therefore be said that although no true superparamagnetic to spinglass phase transition occurs in the strongly interacting case, a sharp transition from a superparamagnetic state towards local domains of stable magnetic moments, does occur very close to T_b.

The third significant difference between "superspin" and "superparamagnet" is in the behavior of the FCM. The latter for the superparamagnet increases with the decrease of temperature whereas it not only does not increase but can even decrease as the temperature is lowered for the interacting sample (see Figs. 4.1 and 4.7). The individual blocking model reproduces a monotonous increase in FCM for "superparamagnets". The field-cooled magnetization increases with decreasing temperature until all particles are

blocked. Such features reflect a distribution of T_b, i.e., distribution of particle volumes. On the other hand the temperature independence of the FCM for the "superspins" can not be explained by the individual particle model and is a clear indication of progressive freezing of particle moments which behave in a collective manner.

4.5 Conclusions

In conclusion, similarities as well as distinct differences in the slow dynamics of isolated nanoparticles and of strongly interacting nanoparticles are discussed. Our interacting and non-interacting models are good enough to capture all these signatures. From the comparative study, it is well understood that the similarities are observed in the memory effect following the temperature and field protocol of Sun et al. On the other hand the differences are seen in the FC memory effect, ZFC memory effect and in the FCM.

Chapter 5

Coercivity of Magnetic Nanoparticles: A Stochastic Model.

5.1 Introduction

Coercivity of nanomagnetic systems is an important quantity which plays a crucial role as far as the stabilization of a magnetic system is concerned [78, 79]. Modern magnetic recording technologies involve particles that are near the superparamagnetic limit. In this limit, the energy barrier separating the two energetically degenerate magnetic orientations is small enough that thermal fluctuations naturally lead to spontaneous switching of the orientation. The random magnetization reversals in particles below the superparamagnetic limit degrade recorded information. Thus the main challenge is to keep the energy barrier in the individual particles high enough to make spontaneous switching infrequent and the material is kept magnetically soft enough to facilitate recording. Materials with higher coercivities due to strong magnetocrystalline anisotropies are employed in recording media. Therefore it is essential to understand the size dependent behaviour of coercivity of magnetic fine particles [80].

Various theoretical models have been published on the particle size dependence of coercivity [81, 82]. Thermal switching in single-domain particles was considered by many people [25, 72, 83-85]. The effect of constant magnetic field in Neel relaxation of single-domain regime was discussed by Coffey et al [86, 87]. Nucleation of domain walls was investigated by Braun [88, 89]. The crossover from single to multi-domain switching was investigated numerically by Hinzke et al [90]. But these models failed to explain the decrease in H_c with the increase in particle size. Also the effect of measurement time which is the time

lag between the measurement and the application of field was not included in the above mentioned theoretical models.

In this chapter we have explained the non-monotonic behavior i.e. first increase and

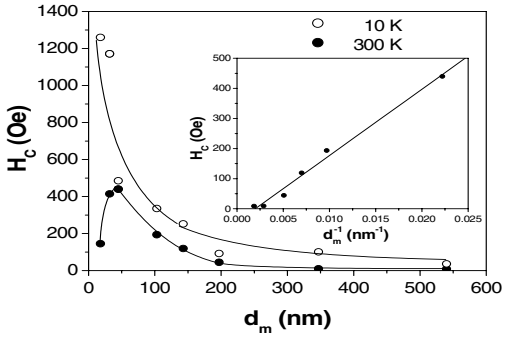

Figure 5.1: Dependence of coercive field on the particle size of $Co_{80}Ni_{20}$ at two different temperatures (solid curves are just a guide to the eye). The inset shows the linear dependence of the coercive field on the inverse of the average particle size. C. Luna *et al*, Nanotechnology *14*, 268 (2003).

then decrease in coercivity with the increase of particle size at room temperature with the help of non-equilibrium statistical mechanics (see Figure 5.1)[91]. Also we have elucidated the monotonous decrease of coercivity with the increase of particle size at very low temperature (10K) within the framework of our two state model (see Figure 5.1). We have added to the model the influence of anisotropy and have used supersymmetry quantum mechanics (SUSY QM), a novel application to a problem in magnetism. Thus, our model puts the phenomena on a more mathematical as well as a quantitative basis, including the effect of measurement time and anisotropic potential. We have assumed that our system is noninteracting and mono-dispersed. The particle size distribution and inter-particle interaction can produce further interesting effects [51, 52, 62, 92], but are not considered here.

In the next section, we have discussed the increasing part of coercive force at room temperature for single-domain particles, assuming the validity of the high barrier and weak noise

limit. Also we have discussed the decrease of the coercive force at low temperature ($10K$). We have justified our model by comparing our numerical results with experimental data. The variation of other magnetic properties, in particular saturation magnetization M_s and the ratio of the remanence to saturation magnetization $\frac{M_r}{M_s}$ values are also discussed in detail in this section. The effect of magnetocrystalline anisotropy on the equilibrium magnetization is illustrated is section 5.3. In section 5.4 we discuss the decreasing part of the coercivity by invoking SUSY method for the multi domain nanoparticles. Finally we summarize and conclude in section 5.5.

5.2 Single-domain Regime and Size Dependent Magnetic Properties

A basic assumption in small-particle magnetism is that a single-domain particle, with a given physical orientation, is in thermal equilibrium at a temperature T. Its constituent spins rotate in unison, so the only relevant degree of freedom is the orientation of the net magnetic moment. We consider systems where the magnetic-anisotropy energy has an axial symmetry. Now in an external field $\vec{B}$, the total magnetic energy is

$$V(\vec{m}) = -\frac{KV}{m^2}(\vec{m}\cdot\hat{n})^2 - \vec{m}.\vec{B}, \tag{5.1}$$

where K is the magnetic-anisotropy energy constant, V is the volume of the nanoparticle, and $\hat{n}$ is a unit vector along the anisotropy axis. Introducing the unit vectors $\hat{e} = \frac{\vec{m}}{m}$ and $\hat{b} = \frac{\vec{B}}{B}$, as well as the dimensionless anisotropy and field parameters $\sigma = \frac{KV}{k_BT}$, $\xi = \frac{mB}{k_BT}$, we can express the potential energy (5.1) as

$$-\beta V = \sigma(\hat{e}.\hat{n})^2 + \xi(\hat{e}.\hat{b}), \tag{5.2}$$

where $\beta = \frac{1}{k_BT}$ and k_B is the Boltzmann constant. It is customary to choose the anisotropy axis $\hat{n}$ as the polar axis of a spherical coordinate system. Then, if (θ, ϕ) and $(\lambda, 0)$ denote the angular coordinates of $\vec{m}$ and $\vec{B}$ respectively as shown in figure (5.2), the magnetic energy can be written as

$$-\beta V(\theta,\phi) = \sigma\cos^2\theta + \xi_{\parallel}\cos\theta + \xi_{\perp}\sin\theta\cos\phi, \tag{5.3}$$

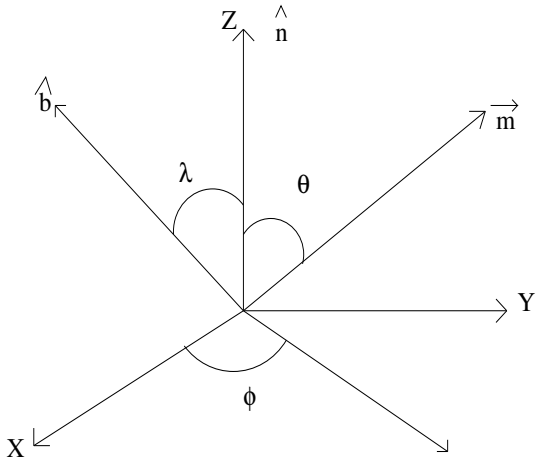

Figure 5.2: Coordinate system used for our calculation in the Section 5.2.

where $\xi_{\parallel} = \xi \cos\lambda$ and $\xi_{\perp} = \xi \sin\lambda$. The potential energy (5.3) is plotted in figure (5.3) for different orientation of λ.

The first phenomenological equation of motion describing the average behavior of the magnetization vector $\vec{m}$ was put forward by Landau and Lifshitz [93] which is given by

$$\dot{\vec{m}} = \gamma \vec{m} \times \vec{H}_{eff}, \tag{5.4}$$

where γ is the gyromagnetic ratio and $\vec{H}_{eff}$ is an effective magnetic field given by

$$\vec{H}_{eff} = -\frac{1}{M_s}\frac{\partial V(\theta,\phi)}{\partial \vec{m}}, \tag{5.5}$$

where M_s is the spontaneous magnetization. Gilbert [94] then proposed an effective damping term yielding

$$\dot{\vec{m}} = \frac{b}{a} M_s \vec{m} \times \vec{H}_{eff} + b M_s (\vec{m} \times \vec{H}_{eff}) \times \vec{m}, \tag{5.6}$$

where $b = \frac{\gamma a}{(1+a^2)M_s}$, $a = \eta\gamma M_s$ and η is a phenomenological damping constant. From Eq. (5.6) Brown [25] derived the Fokker-Planck equation for the distribution of magnetization vector, following the work of Wang and Uhlenbeck [8]. Brown's treatment is based on the assumption that the individual magnetization vector in a system of single-domain magnetic particles is like a density that is connected to a current of representative points moving around the surface of a unit sphere having a number density W($\vec{m}$,t) and current

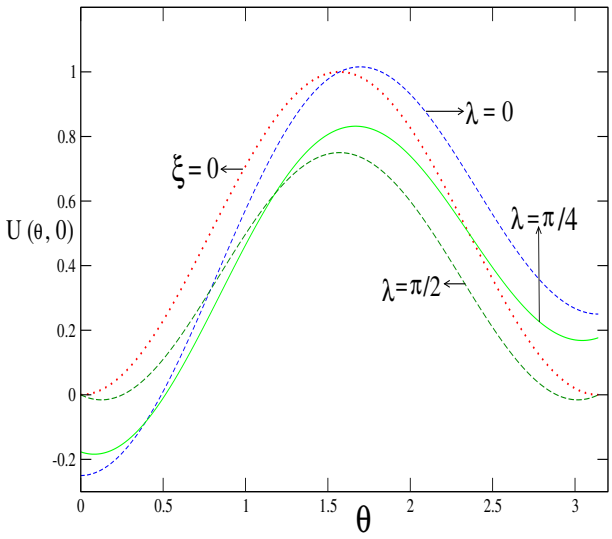

Figure 5.3: Variation of the potential function with polar angle θ for different values of λ. The angle ϕ is fixed at zero.

density $\vec{J}(\vec{m},t)$. Since such representative points can neither be created nor destroyed, W and $\vec{J}$ satisfy the continuity equation

$$\dot{W} = -\frac{\partial \vec{J}}{\partial \vec{m}}. \tag{5.7}$$

The representative points that are concentrated around the minima are dispersed by the influence of the random thermal agitation. This can be represented by the inclusion of a diffusion term of the form $-\kappa\frac{\partial W}{\partial \vec{m}}$, where κ is a constant at a given temperature. Thus the current density $\vec{J}$ is given by

$$\begin{aligned} \vec{J} &= W\dot{\vec{m}} - \kappa\frac{\partial W}{\partial \vec{m}} \\ &= -\frac{b}{a}W\vec{m}\times\frac{\partial V}{\partial \vec{m}} - bW\frac{\partial V}{\partial \vec{m}} - \kappa\frac{\partial W}{\partial \vec{m}} \end{aligned} \tag{5.8}$$

Now following Brown's treatment [25] we obtain the following Fokker-Planck equation in spherical polar co-ordinates:

$$\begin{aligned} \dot{W} &= \beta^{-1}b\nabla^2 W + bW\nabla^2 V + b\Big(\frac{\partial V}{\partial\theta}\frac{\partial W}{\partial\theta} + \frac{1}{\sin^2\theta}\frac{\partial V}{\partial\phi}\frac{\partial W}{\partial\phi}\Big) \\ &\quad + \frac{b}{a\sin\theta}\Big(\frac{\partial V}{\partial\theta}\frac{\partial W}{\partial\phi} - \frac{\partial V}{\partial\phi}\frac{\partial W}{\partial\theta}\Big). \end{aligned} \tag{5.9}$$

In the intermediate-to-high-damping (IHD) approximation of Brown, the potential V may be taken approximately close to the i^{th} stationary point by a Taylor series [95] truncated at the second-order terms so that

$$V(\vec{m}) = V_i + \frac{1}{2}C_1^{(i)}\langle \vec{m}.e_1^{(i)}\rangle^2 + \frac{1}{2}C_2^{(i)}\langle \vec{m}.e_2^{(i)}\rangle^2, \tag{5.10}$$

where the co-ordinate systems $\{e_k^{(i)}\}_{k=1,2,3}$ are oriented so that $e_3^{(i)}$ points in the direction of the stationary point. The condition for stationarity for the potential (5.3) is

$$\sin\theta\cos\theta + h\cos\lambda\sin\theta - h\sin\lambda\cos\theta\cos\phi = 0, \tag{5.11}$$

where $h = \frac{\xi}{2\sigma}$. On introducing $u = h\cos\lambda$, $r = h\sin\lambda$ and $x = \cos\theta$, we obtain

$$(x+u)\sqrt{1-x^2} \pm rx = 0, \tag{5.12}$$

where the negative sign corresponds to the stationary points that occur for $\phi = 0$ while the positive sign represents the local maximum that occurs for $\phi = \pi$. Thus we obtain

$$V_i = \beta^{-1}\sigma\Big(1 - x_i^2 - 2ux_i - 2r\sqrt{1-x_i^2}\Big), \tag{5.13}$$

$$C_1^{(i)} = 2\beta^{-1}\sigma\Big(x_i^2 + ux_i + r\sqrt{1-x_i^2}\Big), \tag{5.14}$$

$$C_2^{(i)} = 2\beta^{-1}\sigma\Big(-1 + 2x_i^2 + ux_i + r\sqrt{1-x_i^2}\Big), \tag{5.15}$$

where $-1 \le x_2 \le x_0 \le x_0' \le x_1 \le 1$ are the roots of the equation

$$(x+u)^2(1-x^2) = r^2x^2 \tag{5.16}$$

which is obtained by squaring equation (5.12). Let us assume that the ratio of barrier height to thermal energy is appreciable i.e. $(\beta(V_0 - V_i) \ge 1)$, so that we may say that the density of magnetic moment orientation W, if replaced by n_i (the number of particles in the i^{th} orientation), rapidly achieves a state of quasiequilibrium [25]. Thus the Fokker-Planck equation (5.9) reduces to the rate equations :

$$\dot{n}_1 = -\dot{n}_2 = \nu_{2,1}n_2 - \nu_{1,2}n_1, \tag{5.17}$$

where $\nu_{i,j}$ is the transition probability from orientation i to orientation j, and n_1 and n_2 are the number of particles with a positive orientation and negative orientation respectively. The transition probabilities are given by

$$\nu_{1,2} = \tau_1^{-1} = b\sqrt{C_1^{(1)}C_2^{(1)}}e^{-\beta(V_0-V_1)}\frac{-(C_1^{(0)}+C_2^{(0)}) + \sqrt{(C_2^{(0)}-C_1^{(0)})^2 - \frac{4C_1^{(0)}C_2^0}{a^2}}}{4\pi\sqrt{-C_1^{(0)}C_2^{(0)}}} \tag{5.18}$$

and

$$\nu_{2,1} = \tau_2^{-1} = b\sqrt{C_1^{(2)}C_2^{(2)}}e^{-\beta(V_0-V_1)}\frac{-(C_1^{(0)}+C_2^{(0)}) + \sqrt{(C_2^{(0)}-C_1^{(0)})^2 - \frac{4C_1^{(0)}C_2^0}{a^2}}}{4\pi\sqrt{-C_1^{(0)}C_2^{(0)}}} \tag{5.19}$$

The solution of equation (5.17) is

$$n_2(t) = \frac{n\tau_2 - e^{-(\frac{1}{\tau_1}+\frac{1}{\tau_2})t}(n\tau_2 - n_2(\tau_2+\tau_1))}{\tau_1+\tau_2}, \tag{5.20}$$

where $n = (n_1+n_2)$. We know (n_1-n_2) is proportional to the net magnetization along the direction of the applied magnetic field. For a single domain particle with large relaxation time, if one changes the magnetic field after a finite interval of time (t), then

$$\lim_{\delta H\to 0^-} n_2^{H-\delta H}(t) = n_2^{H^{\rightarrow}}(0) \neq \lim_{\delta H\to 0^+} n_2^{H+\delta H}(t) = n_2^{H^{\leftarrow}}(0). \tag{5.21}$$

This implies that for a particular value of H one should not expect to get the same value of magnetization during increasing and decreasing cycle of H. Since the relaxation time τ_i increases with particle volume, $(M^{H\leftarrow} - M^{H\rightarrow})$ also increases with particle volume giving rise to higher coercivity. Hence coercivity is a consequence of the quasi-static non-equilibrium measurement. Therefore, Langevin theory of paramagnetism is not applicable in these cases. We use equation (5.20) to generate M versus H curve as shown in Fig. (5.4), for particle sizes 7 nm and 18.5 nm., t = 120 sec and K=10^6 erg/cc which is realistic for measurements of coercivity by a vibrating sample magnetometer.

In the superparamagnetic limit the energy barrier separating the two energetically degenerate magnetic orientations is very small. Thus thermal fluctuations frequently lead to spontaneous switching of the orientation. In the Fig. (5.5) we have compared our numerically simulated data obtained from the two-state model with that of the experimental data obtained from the W. H. Meiklejohn [96] and F. E. Luborsky [97]. The agreement

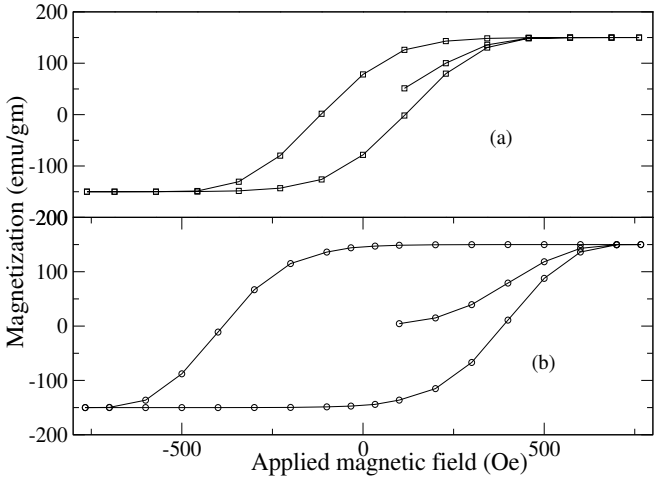

Figure 5.4: Simulated M versus H curve for two particle sizes (a) 7 nm and (b)18.5 nm respectively.

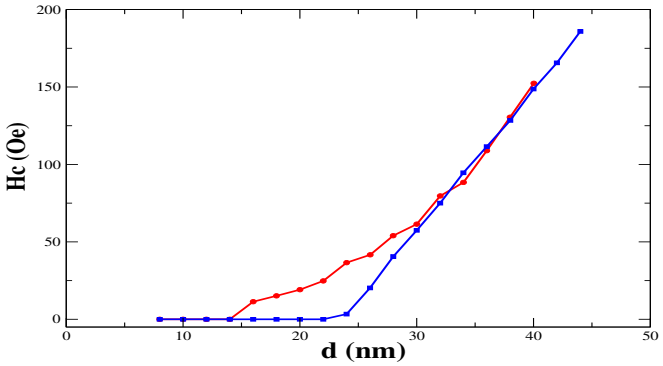

Figure 5.5: Dependence of coercive force on the particle diameter for the $Co_{80}Ni_{20}$ nanoparticles at room temperature (300K) for the single domain regime. Red filled dot denotes the experimental data (C. Luna et al [78]) and the blue filled square denotes the simulation data obtained from our model.

of the numerical data with that of experimental data is excellent. At very low temperatures thermal effects are negligible and a different size-dependence of the coercivity force is observed. The size dependence of coercivity at $10K$ monotonically decreases with in-

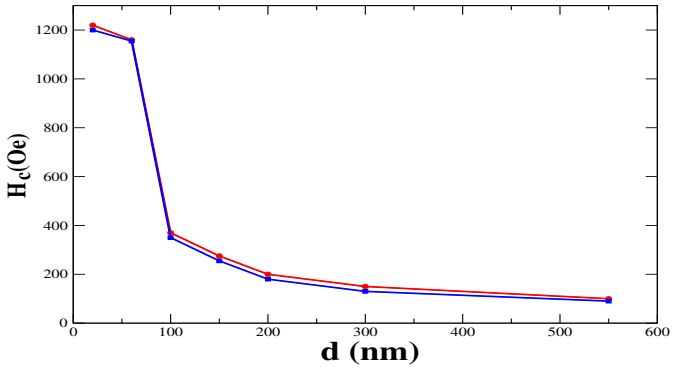

Figure 5.6: Dependence of coercive force on the particle diameter for the $Co_{80}Ni_{20}$ nanoparticles at $10K$. Red filled dot denotes the experimental data (C. Luna et al [78]) and the blue filled square denotes the simulation data obtained from our model.

creasing size over the whole range of sizes. This is shown in figure (5.6). At $10K$ the thermal energy is small in comparison to the anisotropy energy barrier, given by $K_{eff}V$, where V is the particle volume and the effective anisotropy constant takes the following phenomenological expression $K_{eff} = K_V + \frac{6}{d}K_s$, where K_V and K_s are the volume and surface anisotropy energy constants respectively. Thus the particles behave as if they are more anisotropic and the surface region is magnetically harder than the core region due to the anisotropy induced by the surface layer. This anisotropy which increases with the decrease of particle size has crystal field nature and is coming from the symmetry breaking at the boundaries of the particles.

The particle size dependence of M_s is shown in Fig. (5.7). The saturation magnetization, M_s, decreases from 130 to 55 emu g^{-1} at $300K$ as the particle size decreases. The decrease in coercivity follows an inverse linear relationship with the particle size. This linear relationship is also observed at low temperature ($10K$). Thus we can conclude that this reduction in M_s is totally related with the surface to volume ratio. As the ratio increases the surface contribution increases and ultimately resulting in a high saturation magnetization.

The variation of the remanence to saturation magnetization ratio, $\frac{M_r}{M_s}$, at $10K$ as a function of the particle size is shown in Fig. (5.8). This variation is somewhat similar to that of the coercivity. At very low temperature ($10K$) the smallest particles have an $\frac{M_r}{M_s}$

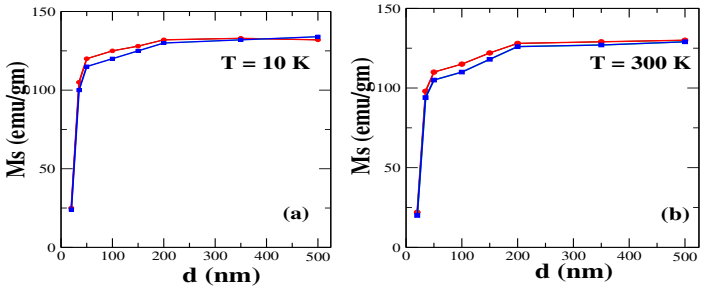

Figure 5.7: Dependence of saturation magnetization (M_s) on the particle diameter for the $Co_{80}Ni_{20}$ nanoparticles at (a) $10K$ and (b) $300K$. Red filled dot denotes the experimental data (C. Luna et al [78]) and the blue filled square denotes the simulation data obtained from our model.

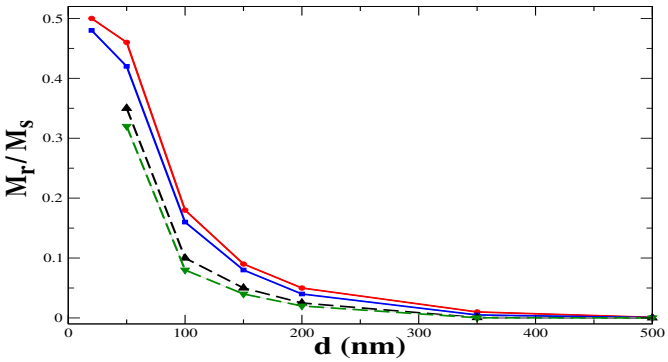

Figure 5.8: Dependence of the ratio of remanence to saturation magnetization ($\frac{M_r}{M_s}$) on the particle diameter for the $Co_{80}Ni_{20}$ nanoparticles at $10K$ and $300K$. Red filled dot solid line denotes the experimental data (C. Luna et al [78]) and the blue filled square solid line denotes the simulation data obtained from our model at $10K$. Black filled upward triangles dashed line denote the experimental data (C. Luna et al [78]) and green filled downward triangles dashed line denote the simulation data obtained from our model at $300K$.

value close to 0.5 which is the value of $\frac{M_r}{M_s}$ for a random distribution of non-interacting uniaxial particles. The other particles have much smaller value of $\frac{M_r}{M_s}$. On the other hand

this ratio is much smaller for the smallest particles at room temperature. This is due to thermal agitation which frequently leads to spontaneous switching of the orientation.

In simulating all the above mentioned graphs we always use the two state model i.e. the high barrier and weak noise limit (equation 5.17), and the following parameters. The anisotropy energy is measured in units of thermal energy (k_BT). Experimentally $K \sim 10^6$ erg/c.c and we use $V = \frac{4}{3}\pi r^3$. Now the ratio $\alpha = \frac{KV}{k_BT}$ is chosen in such a way that KV varies between $0.5k_BT$ to $10k_BT$. The relaxation dynamics is mainly governed by $\tau_{1,2} = \tau_0 \exp\left(\frac{KV \pm M_s h}{k_BT}\right)$. We know $\tau_0 \sim 10^{-10}$ sec. Typically we have focused in the time window of $10^{11}\tau_0$ which is equivalent to experimental measurement time of DC magnetization. We use $hM_s \sim 0.2k_BT$ for our simulation. Here we are dealing with about 1000 (n) particles.

In this section we have shown that the non-equilibrium state governs the magnetic hysteresis of nano-magnetic systems. The variation of coercivity at room temperature as well as at 10K as a function of particle size has also been explained in this section. We have also studied the effect of surface anisotropy on the magnetic properties of our nanomagnetic system.

5.3 Effect of Anisotropic Potential

In the case of a superparamagnetic system, a common practice is to fit the magnetization curve by using the Langevin theory of paramagnetism [98]. But the Langevin theory of paramagnetism does not include magnetocrystalline anisotropy energy, and hence it is necessary to obtain deeper insight into the statistical properties of non-interacting magnetically anisotropic nanoparticles in the framework of classical physics. We derive the first few terms in the expansion of partition function $\mathcal{Z}$ in powers of $\sigma = \frac{KV}{k_BT}$. This expansion will provide a suitable description of the magnetization when the anisotropy energy is small in comparison to the thermal energy. Now the magnetic energy corresponding to figure (5.9) is given by

$$-\beta V(\theta, \phi, \lambda) = \sigma\Big(\sin\theta \sin\lambda \cos\phi + \cos\theta \cos\lambda\Big)^2 + \xi \cos\theta. \tag{5.22}$$

With this choice of co-ordinate and magnetic energy, the partition function becomes

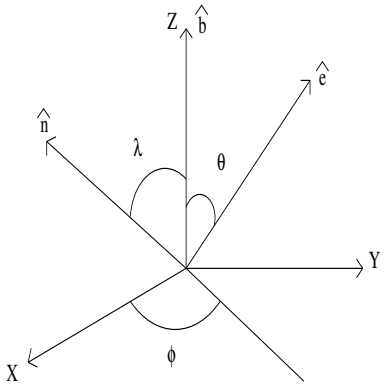

Figure 5.9: Coordinate system used for our calculation in the Section 5.3.

$$\mathcal{Z} = \frac{1}{2\pi}\int_0^{\pi} d\theta \sin\theta \exp(\xi\cos\theta)\int_0^{2\pi} d\phi \exp[\sigma(\sin\theta\sin\lambda\cos\phi + \cos\theta\cos\lambda)^2]. \quad (5.23)$$

5.3.1 Weak Anisotropy

We expand the second exponential of equation (5.23) to obtain

$$\mathcal{Z} = \sum_0^{\infty} \frac{\sigma^i}{i!} z_i, \quad (5.24)$$

where

$$z_i = \frac{1}{2\pi}\int_0^{\pi} d\theta \sin\theta \exp(\xi\cos\theta)\int_0^{2\pi} d\phi(\cos\lambda\cos\theta + \sin\lambda\cos\theta\cos\phi)^{2i} \quad (5.25)$$

Let us rewrite equation (5.24) in powers of σ as

$$\mathcal{Z} = \mathcal{Z}_0\Big(1 + \frac{\mathcal{Z}_1}{\mathcal{Z}_0}\sigma + \frac{\mathcal{Z}_2}{2\mathcal{Z}_0}\sigma^2 + ...\Big). \quad (5.26)$$

Thus

$$\ln\mathcal{Z} \simeq \ln\mathcal{Z}_0 + \frac{\mathcal{Z}_1}{\mathcal{Z}_0}\sigma + \frac{1}{2}\Big[\frac{\mathcal{Z}_2}{\mathcal{Z}_0} - \Big(\frac{\mathcal{Z}_1}{\mathcal{Z}_0}\Big)^2\Big]\sigma^2, \quad (5.27)$$

where

$$\mathcal{Z}_0 = \frac{2}{\xi}\sinh\xi \quad (5.28)$$

$$\frac{\mathcal{Z}_1}{\mathcal{Z}_0} = \Big(1 - \frac{2}{\xi}L(\xi)\Big)\cos^2\lambda + \frac{1}{\xi}L(\xi)\sin^2\lambda \quad (5.29)$$

$$\frac{1}{2}\Big[\frac{\mathcal{Z}_2}{\mathcal{Z}_0}-\Big(\frac{\mathcal{Z}_1}{\mathcal{Z}_0}\Big)^2\Big] = \frac{2}{\xi^2}\Big\{[2(1-\frac{3}{\xi}L)-L^2]\cos^4\lambda-[6(1-\frac{3}{\xi}L)-L^2-\xi L]\cos^2\lambda\sin^2\lambda +\frac{1}{4}[3(1-\frac{3}{\xi}L)-L^2]\sin^4\lambda\Big\} \tag{5.30}$$

and

$$L(\xi)=\coth\xi-\frac{1}{\xi}. \tag{5.31}$$

From the relation

$$\mathcal{M}_B=m\frac{\partial}{\partial\xi}(\ln\mathcal{Z}), \tag{5.32}$$

we obtain

$$\frac{\mathcal{M}_B}{m}\simeq L(\xi)+\frac{d}{d\xi}\Big(\frac{\mathcal{Z}_1}{\mathcal{Z}_0}\Big)\sigma+\frac{1}{2}\frac{d}{d\xi}\Big[\frac{\mathcal{Z}_2}{\mathcal{Z}_0}-\Big(\frac{\mathcal{Z}_1}{\mathcal{Z}_0}\Big)^2\Big]\sigma^2. \tag{5.33}$$

Taking derivatives of equations (5.29) and (5.30) with respect to ξ, we obtain magnetization for some relevant particular cases. First we consider the case when the external applied field direction is parallel to the anisotropy axis

$$\frac{\mathcal{M}_{B,\parallel}}{m} \simeq L(\xi)+\frac{2}{\xi}\Big[L^2-(1-\frac{3}{\xi})L\Big]\sigma+\frac{4}{\xi^3}\Big[3L^2-5(1-\frac{3}{\xi}L) +\xi L[L^2-(1-\frac{3}{\xi}L)]\Big]\sigma^2. \tag{5.34}$$

For the perpendicular case

$$\frac{\mathcal{M}_{B,\perp}}{m} \simeq L(\xi)-\frac{1}{\xi}\Big[L^2-(1-\frac{3}{\xi}L)\Big]\sigma+\frac{3}{2\xi^3}\Big[3L^2-5(1-\frac{3}{\xi}L) +\xi L[L^2-(1-\frac{3}{\xi}L)]\Big]\sigma^2. \tag{5.35}$$

When anisotropy axes are distributed at random,

$$\frac{\langle\mathcal{M}_B\rangle_{ran}}{m}\simeq L(\xi)-\frac{4}{15}(1-\frac{3}{\xi}L)\frac{1}{\xi}[L^2-(1-\frac{3}{\xi}L)]\sigma^2. \tag{5.36}$$

From Fig. 5.10(a) it is evident that for the longitudinal field case, anisotropy favors the alignment of magnetic moment along the field direction, whereas in the transverse field case the anisotropy hinders the magnetic moment to align in the field direction. The anisotropy contribution $\Big(\mathcal{M}_B(\xi)-mL(\xi)\Big)$ has been shown in figure 5.10(b). From this figure it is evident that the random orientation of the anisotropy axes significantly reduces the anisotropy induced contribution to the magnetization process. In the low

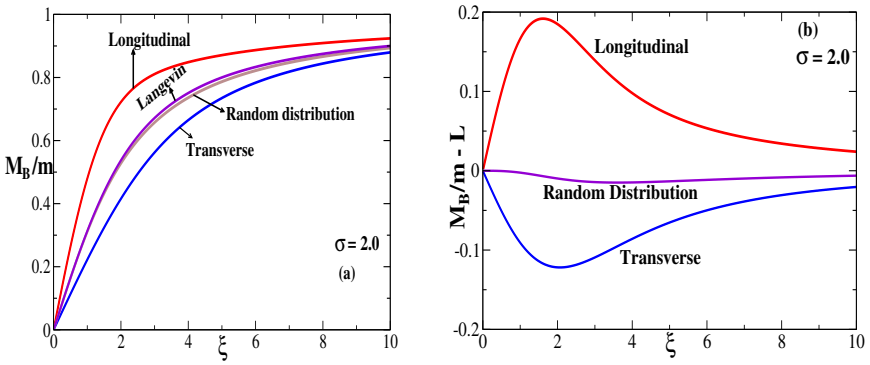

Figure 5.10: (a) Variation of magnetization with longitudinal field $\xi = \frac{mB}{k_B T}$ for different cases with easy axis anisotropy (b) Variation of anisotropy-induced contribution with longitudinal field for the same.

field regime, this cancellation is exact. For the easy-plane anisotropy case ($\sigma < 0$), the longitudinal and transverse field interchange their roles. In this case, when $\vec{B} \parallel \hat{n}$, the anisotropy hinders the magnetization process, whereas when $\vec{B} \perp \hat{n}$, anisotropy favors it and for the anisotropy axes distributed at random, the randomness again reduces the anisotropy induced contribution as shown in figure 5.11(a). In figure 5.11(b) we have shown the anisotropy induced contribution for the easy-plane case ($\sigma < 0$).

5.3.2 Strong Anisotropy

In order to complement the weak-anisotropy expansion, we now discuss the asymptotic expansion of the partition function for strong anisotropy. The desired expansion is given by

$$\begin{aligned} \mathcal{Z} \;\simeq\; & \frac{e^{\sigma}}{\sigma}\cosh\xi_{\parallel}\Big\{1+\frac{1}{4\sigma}[(2+\xi_{\perp}^{2})-2\xi_{\parallel}\tanh\xi_{\parallel}\Big]+\frac{1}{4\sigma^{2}}[(3+\xi_{\parallel}^{2} \\ & +\xi_{\perp}^{2}+\frac{1}{8}\xi_{\perp}^{4})-(3+\xi_{\perp}^{2})\xi_{\parallel}\tanh\xi_{\parallel}]+....\Big\}, \end{aligned} \tag{5.37}$$

from which,

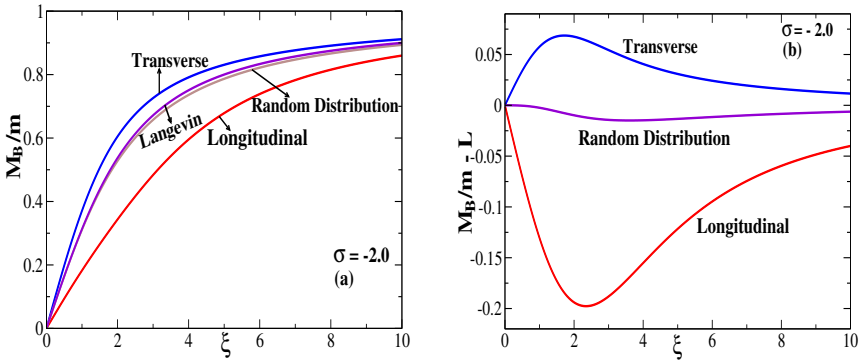

Figure 5.11: (a) Variation of magnetization with longitudinal field $\xi = \frac{mB}{k_B T}$ for different cases with easy plane anisotropy (b) Variation of anisotropy-induced contribution with longitudinal field for the same.

$$\ln \mathcal{Z} \simeq \ln\Big(\frac{e^{\sigma}}{\sigma}\cosh\xi_{\parallel}\Big) + \frac{1}{4\sigma}\Big[(2+\xi_{\perp}^{2}) - 2\xi_{\parallel}\tanh\xi_{\parallel}\Big] + \frac{1}{8\sigma^{2}} \times\Big[5 + (2\xi_{\parallel}^{2}+\xi_{\perp}^{2}) - (4+\xi_{\perp}^{2})\xi_{\parallel}\tanh\xi_{\parallel} - \xi_{\parallel}^{2}\tanh^{2}\xi_{\parallel}\Big]. \tag{5.38}$$

For the longitudinal field case, we obtain

$$\frac{\mathcal{M}_{B,\parallel}}{m} \simeq \tanh\xi\Big\{1 - \frac{1}{2\sigma}\Big[1 + \frac{2\xi}{\sinh(2\xi)}\Big] - \frac{1}{8\sigma^{2}}\Big[4 - \xi\frac{\sinh(2\xi) - 2\xi}{\cosh^{2}\xi}\Big]\Big\}, \tag{5.39}$$

and for the perpendicular case

$$\frac{\mathcal{M}_{B,\perp}}{m} \simeq \xi\Big(\frac{1}{2\sigma} + \frac{1}{4\sigma^{2}}\Big). \tag{5.40}$$

For the sake of completeness we plot in Fig. (5.12) the magnetization versus longitudinal field for both weak-anisotropy and strong-anisotropy cases for different values of the dimensionless anisotropy parameter (σ).

We conclude this section by stating that the anisotropic potential does effect the magnetization process of single-domain particle but one can use the Langevin theory of superparamagnetism for the weak anisotropy case with anisotropy axes distributed at random.

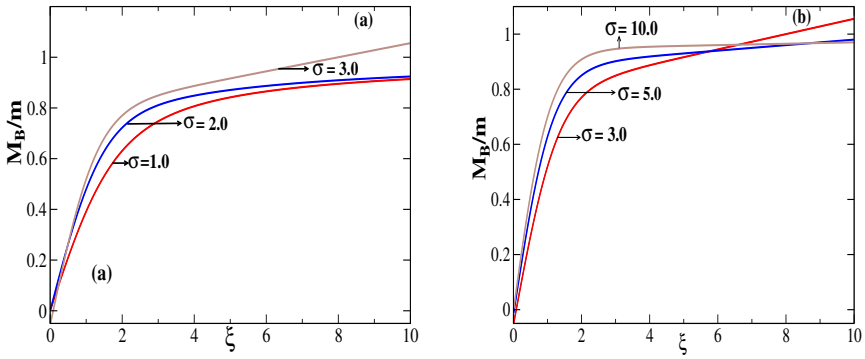

Figure 5.12: Variation of magnetization with longitudinal field $\xi = \frac{mB}{k_B T}$ for different values of σ (a) Weak-anisotropy case (b) Strong-anisotropy case.

5.4 Multi-domain Regime

We now provide an explanation for the decrease of the coercive field with the increase in particle size. It is clear from the above discussion that this can not happen if the particles still comprise single domains. Obviously a single to multi domain transformation takes place at the maximum of coercivity. The critical diameter for which the single domain structure becomes multidomain can be estimated from the balance between the energy to form a single wall and the alternative magnetostatic energy which is given by $d_c = \frac{9(AK)^{\frac{1}{2}}}{(2\pi M_s^2)}$, where A and K are the exchange and anisotropy constants respectively. The critical diameters above which the particle becomes multidomain for the $Co_{80}Ni_{20}$, Ni, Fe and Co are $30nm$, $42nm$, $10nm$ and $20nm$ respectively. For the sake of simplicity, we consider only the axial symmetry case for the multi-domain regime. Then both the Gibbs free energy per unit volume (V) and the distribution of magnetization orientation (W) are axially symmetric i.e V and W are independent of ϕ.

We consider an arrangement of spin in a linear chain as shown Fig. (5.13). In the following discussion one should keep in mind that we are not interested in the origin of the domain wall, instead we assume its existence and incorporate the relevant terms in the Hamiltonian. The Gilbert equation corresponding to the i-th spin is

$$\dot{\vec{m}}^{(i)} = \frac{b}{a} M_s \vec{m}^{(i)} \times \vec{H}_{eff}^{(i)} + b M_s (\vec{m}^{(i)} \times \vec{H}_{eff}^{(i)}) \times \vec{m}^{(i)} \tag{5.41}$$

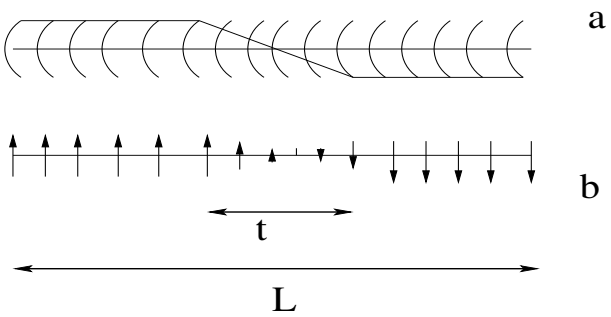

Figure 5.13: Spin distribution near 180^o domain wall (a) in real space (b) in probability space.

For a particular site the spin can rotate over the surface of a sphere along a semicircular curve ($\theta \, \epsilon \, [0, \pi]$). Writing all terms in spherical polar coordinate and proceeding as above (section 2) we have

$$\frac{\partial W^{(i)}(\theta,t)}{\partial t} = \frac{b}{\sin\theta}\frac{\partial}{\partial\theta}\Big[\sin\theta\Big(\frac{\partial V}{\partial\theta}W^{(i)} + \beta^{-1}\frac{\partial W^{(i)}}{\partial\theta}\Big)\Big]. \tag{5.42}$$

Here we use the condition $\frac{dJ^i(\theta,t)}{d\phi} = 0$, which physically means there is no spin hopping between two sites. This implies that the spin will start relaxing along the surface of the sphere without changing its position along Z-axis. We use the transformation $W(\theta,t) = \sqrt{W_{eq}(\theta)}\psi(\theta,t)$ with $W_{eq}(\theta) = A_0 e^{\frac{-U(\theta)}{\epsilon}}$ and $\epsilon = k_B T$ in equation (5.42) and we obtain

$$\frac{d\psi}{dt} = k_1\psi'' + h_1\Big(\frac{U''(\theta)}{2} - \frac{U'^2}{4\epsilon}\Big)\psi, \tag{5.43}$$

where $h_1 = \frac{b}{k_B T}$. Introducing a new function $\phi(\theta)$ such that $\psi(\theta,t) = \phi(\theta)e^{-\lambda' t}$, we obtain from equation (5.43)

$$\lambda\phi = \epsilon\phi'' + \Big(\frac{U''(\theta)}{2} - \frac{U'^2}{4\epsilon}\Big)\phi, \tag{5.44}$$

with $\lambda = \frac{\lambda'}{h_1}$. Now we shall define two operators $A = \frac{\partial}{\partial\theta} + \frac{U'}{2\epsilon}$ and $A^\dagger = -\frac{\partial}{\partial\theta} + \frac{U'}{2\epsilon}$, such that one can easily rewrite equation (5.44)

$$\epsilon A^\dagger A\phi = \lambda\phi. \tag{5.45}$$

Without loss of generality, we can choose the ground state eigenvalue of $A^\dagger A$ equal to zero (since $A\phi_0 = 0$ to get equilibrium distribution). Once we satisfy $A^\dagger A = 0$, the next step in Super Symmetric (SUSY) Quantum Mechanics (QM) is to define the operator

$AA^\dagger$. Now it is well known in SUSY QM that if ϕ_1 is the first excited eigenstate of $A^\dagger A$ then it is the ground state of $AA^\dagger$ with ground state eigenvalue λ_1 [99]. One can apply a variational method to obtain λ_1

$$\lambda_1 = \frac{\int \phi_1(\theta)\epsilon AA^\dagger \phi_1(\theta)d\theta}{\int \phi_1(\theta)\phi_1(\theta)d\theta}. \tag{5.46}$$

The solution (λ_1) of the Fokker Planck equation can be obtained by using a trial wave-function for the variational method as $e^{\frac{f(\theta)}{2\epsilon}}$. We shall use the following form of $f(\theta)$ in different regions

$$f(\theta) = U(c) - U(c-\theta), \qquad -\infty \leq \theta \leq c$$

$$f(\theta) = U(\theta), \qquad c \leq \theta \leq d$$

$$f(\theta) = U(d) - U(\theta - d), \qquad d \leq \theta \leq \infty$$

with the condition that $f(\theta)$ must match at $\theta = c$ and $\theta = d$ from either side. The potential energy of the spins making an angle less than 90^0 can be approximated by a harmonic oscillator like potential $V(\theta) = \frac{1}{2}K\theta^2$. Once we get the form of $f(\theta)$ we can apply the variational method to equation (5.46). The result obtained for λ_1 will be in terms of variational parameters c and d. Setting the condition

$$\frac{d\lambda_1}{dc} = \frac{d\lambda_1}{dd} = 0, \tag{5.47}$$

we derive the desired relaxation rate as

$$\lambda_1 \sim h_1(e^{\frac{-(U_0 - U(\theta_1))}{\epsilon}} + e^{\frac{-(U_0 - U(\theta_2))}{\epsilon}}), \tag{5.48}$$

where U_0 is the barrier height and θ_1 and θ_2 are the two minima. It is clear that the relaxation rate depends on the damping parameter as well as the barrier height, which in turn depends on the value of anisotropy constant and the angle between successive spins. The anisotropy constant is higher (one order of magnitude) for smaller particles, giving rise to a higher coercive field. Even though our model, consisting of a linear chain of ferromagnetic particles having just two domains, with their easy axes parallel to each

other, and not containing a domain of closure, is a simplistic one, it can still be regarded as a starting point to explain qualitatively the hysteresis of a multi domain system.
The above mentioned claim can be verified by comparing the theoretical results obtained from the Monte Carlo (M. C.) simulation of our model with that of the experimental results of Gangopadhyay et al [79] and Luna et al [78]. The study of the relaxation dynamics of a realistic multi-domain system is beyond the scope of this chapter. But one can think of the following scheme. We can simulate the relaxation kinetics by the infinitesimal spin-rotation dynamics [100]. This dynamics can be realized by the Metropolis algorithm. The acceptance probability in the metropolis algorithm for the proposed rotation of the spin at site j from S_j to $R(S_j)$ is defined as $W[S_j \rightarrow R(S_j)] = min[1, \exp(-\beta\delta E_j)]$, where δE_j is the energy change due to the spin rotation. Here the relaxation of the dimensionless system magnetization can be studied by starting from an initial state magnetized opposite to the applied field. One can randomly choose one spin (say j-th) out of the whole spin chain. Then the orientation of the j-th spin is kept fixed and the other spins are allowed to relax. Considering the configurations of all other spins we can calculate the energy of the j-th spin, change the orientation of the same spin by an infinitesimal small angle $\delta\theta$, and do the same calculation. In this way one can easily evaluate the energy profile of the j-th spin as a function of θ. Using our model one can easily calculate the relaxation time depending upon the special position of the spin and verify the model.

5.5 Summary and Conclusions

The particle size dependence of different magnetic properties of nanomagnetic particles is explained from the view point of non-equilibrium statistical mechanics. At room temperature, a maximum in coercive force field is observed. Thus below a certain critical diameter d_c, the coercive force decreases with the decrease of particle size and above d_c the coercive force increases with the decrease of the particle size. It indicates that two different mechanisms are responsible for this contrasting behaviour in magnetization reversal process. Below d_c, the decrease in H_c with decreasing particle size is due to thermal effects observed in particles which behave as single domain particles. In this regime the magneti-

zation reversal occurs by coherent spin rotation. The largest particles behave as magnetic multidomain particles and the magnetization reversal occurs by wall motion. Assuming the single to multi-domain transformation we have shown that the relaxation time of the sample decreases with increase in particle size due to decrease in surface pressure and anisotropy constant that yields a decrease in coercivity. In the multidomain regime we apply a SUSY QM approach that matches with the alternate method of Coffey et al [83]. In addition, we extend the study to explain the decrease in coercivity of nanoparticles. The important point to note is that in any experimental study of a single domain particle at room temperature, one should perform a coercive field (H_c) versus particle size curve to determine the peak in the curve and make all the measurements below d_c to analyze the behavior of single domain magnetic nanoparticles. At room temperature, the saturation magnetization M_s decreases in an inverse linear relationship with the decrease of particle size. The variation of the ratio $\frac{M_r}{M_s}$ as a function of particle size is somewhat similar to that of the coercivity at $300K$.

Turning to low temperatures ($< 10K$), the magnetic properties of nanoparticles are quite different from that at the room temperature. At $10K$ the coercive field decreases monotonically with increasing size over the whole range of sizes. The ratio $\frac{M_r}{M_s}$ also decreases monotonically over the whole range of particle size at $10K$. The contributions of thermal and surface effects are different at different temperatures. As a result we observe differences in magnetic behaviour at different temperatures, in particular in the saturation magnetization, the coercivity and the ratio of the remanence to saturation magnetization. The surface effect dominates at low temperature, whereas thermal effect dominates at high temperature, as expected.

We have also demonstrated the effect of an anisotropic potential on equilibrium magnetization of such a collection of non-interacting single-domain magnetic nanoparticles. It is seen that a random distribution of anisotropy axis reduces the anisotropy induced contribution considerably, thereby validating the use of the Langevin theory of superparamagnetism for the weak anisotropy and random axis case.

Our results can be useful in the interpretation of magnetic data and magnetization reversal process observed in nanocrystalline particles where the interparticle interaction can be neglected. This study is also helpful in studying magnetic relaxation of nanoparticles

which is very important in understanding magnetic recording technologies.

Chapter 6

Diffusion Enhancement in a Periodic Potential Under High-frequency Space-dependent Forcing

6.1 Introduction

So far, we have studied the rotational Brownian motion of the giant magnetic moment of a single domain nanomagnetic particle across an anisotropic potential barrier. In this chapter we discuss the translational Brownian motion of an underdamped Brownian particle moving in a systematic periodic potential in the presence of a high-frequency space-dependent forcing[101]. Brownian motion in periodic structures has various applications to condensed matter physics, nanotechnology and molecular biology [102-104]. Adding noise to deterministic nonlinear dynamics leads to interesting and important phenomena such as stochastic resonance [105], Brownian motors and chaotic ratchet transport [106], resonant activation [107], noise induced phase transition [108, 109], etc.. Thermal diffusion of a Brownian particle which we will discuss here is of great interest in numerous other contexts, namely Josephson junction [110], rotating dipoles in external fields [111], superionic conductors [112], synchronization phenomena [113], diffusion on crystal surfaces [114], particle separation by electrophoresis [115], and biophysical processes such as intracellular transport [102].

Here we focus on the underdamped motion of a Brownian particle which feels viscous forces and random impulses from the surrounding medium and is confined by a potential well. Our primary interest is to study the effect of an externally applied position dependent driving force that is periodic in time. The frequency is much larger than all other relevant frequencies of the system. Hence we can apply the usual Kapitsa analysis for

high frequency oscillating fields [116]. It has earlier been shown that on time scales larger than the period of perturbation the dynamics is equivalent to one in which the periodic perturbation can be replaced by a time independent effective potential [117, 118]. Ref. [118] treats the overdamped Brownian motion, whereas we deal with underdamped motion of the Brownian particle. The underdamped regime has also been studied by Dutta and Burma [117], who have however based their analysis on the Fokker-Planck equation approach. Here we provide an alternative derivation of the main results through the Langevin dynamics, which is more straightforward.

Further we extend Kapitsa's analysis by using the additional contributions to the effective potential arising from the space dependent periodic force for the calculation of the thermal diffusion coefficient [119, 120]. One remarkable feature of our results is that the effective diffusion coefficient of an underdamped Brownian particle in a periodic potential in the presence of an externally applied space-dependent oscillating force is larger than that in the absence of the external force by about twelve orders of magnitude. With respect to bare thermal diffusion coefficient this enhancement is by about four orders of magnitude. In addition, certain features of the ratchet mechanism in molecular motors [121] are relevant in this context in terms of transport properties(currents).

6.2 Model

The stated Brownian dynamics is governed by the Langevin equation

$$m\ddot{x} = -\gamma\dot{x} - \frac{\partial}{\partial x}U(x) + F(x,t) + \eta(t), \tag{6.1}$$

where m is the mass of the Brownian particle, γ is the friction coefficient, U(x) is the confining potential, F(x,t) is the periodic driving force with a period τ and F(x,t) = F(x,t+τ). Thermal fluctuations are modeled by the zero mean δ-correlated white noise $\eta(t)$ i.e. $<\eta(t)> = 0$ and $<\eta(t)\eta(t')>= 2\gamma\beta^{-1}\delta(t-t')$, where $\beta = (k_BT)^{-1}$, k_B being the Boltzmann constant and T is the temperature. Our goal is to show that, on time scales larger than τ, the dynamics can be mapped onto a modified Langevin dynamics in which the periodic forcing is absent but the potential U(x) can be replaced by a suitable effective potential $U_{eff}(x)$. The methodology we follow is based on Kapitsa's treatment

for high frequency oscillating fields in parametric oscillations [122]. We derive the form of the effective potential upto second order in ξ (expansion parameter which is related to the inverse of the square of the oscillating frequency) in Sec. 6.3.
We also study the transport properties and diffusion coefficient for ratchet like systems. The corresponding Langevin dynamics is governed by the equation

$$m\ddot{x} + \gamma\dot{x} = -V'(x) + A(x)\cos(\Omega t) + \sqrt{2\gamma k_B T}\eta(t), \tag{6.2}$$

where V(x) is a periodic potential with period L i.e. V(x) = V(x+L) and the prime denotes 1st derivative of V(x) with respect to x. In our case $V(x) = -V_0(\sin(x) - \mu\sin(2x))$ with $V_0 = 1$ and $\mu = \frac{1}{4}$ throughout this work. We define the above dynamics as the original dynamics. Following Kapitsa's treatment we derive in the sequel an effective potential for which the dynamics is governed by the equation

$$m\ddot{x} + \gamma\dot{x} = -V'_{eff}(x) + \sqrt{2\gamma k_B T}\eta(t), \tag{6.3}$$

where V_{eff} is derived in Sec. 6.3 below. The first basic quantity of interest in the transport process is the average particle current defined as

$$< \dot{x} >= \lim_{t\to\infty} \frac{< x(t) >}{t}. \tag{6.4}$$

The other quantity of important interest is the effective diffusion coefficient which is defined as

$$D_{eff} = \lim_{t\to\infty} \frac{<< x^2(t) >> - << x(t) >>^2}{2t}, \tag{6.5}$$

where the two brackets respectively denote averages over the initial conditions of position and velocity, and over all realizations of thermal noise. Exact analytical results for D are known for two special cases. First in the absence of the periodic potential we have the famous Einstein's relation $\bar{D} = \frac{k_B T}{\gamma}$. Second is the case in which the periodic potential is present but the external field $A(x)\cos(\Omega t)$ is absent, wherein D is obtained as [123, 124]

$$D = \frac{\bar{D}}{\int_0^L \frac{dx}{L} e^{\frac{V(x)}{k_B T}} \int_0^L \frac{dy}{L} e^{\frac{-V(y)}{k_B T}}}. \tag{6.6}$$

Numerically we calculate this diffusion coefficient for our periodic potential and it is seen that $D << \bar{D}$ as expected.

Calculation of the diffusion coefficient in the presence of both externally applied space-dependent periodic force and arbitrary periodic potential is not analytically possible. Hence we solve Eq. (6.2) and Eq. (6.3) numerically, but by first converting them into dimensionless forms. In doing this we recognize that the characteristic timescale τ_0 that governs the Newtonian dynamics: $m\frac{d^2x}{dt^2} = -V'(x)$, is given by $\tau_0^2 = \frac{mL^2}{V_0}$. Therefore we rescale x by dividing by L and rescale t by dividing by τ_0, to obtain:

$$\ddot{x} + b\dot{x} = -\hat{V}'(x) + a(x)\cos(\omega t) + \sqrt{2bD_0}\hat{\eta} \tag{6.7}$$

$$\ddot{x} + b\dot{x} = -\hat{V}'_{eff}(x) + \sqrt{2bD_0}\hat{\eta}, \tag{6.8}$$

where Eq. (6.7) denotes original dynamics, whereas Eq. (6.8) is for effective dynamics. The various dimensionless quantities appearing above are given by $b = \frac{\gamma\tau_0}{m}$, $\hat{V}(x) = \frac{V(x)}{V_0}$, $a = \frac{AL}{V_0}$, $\omega = \Omega\tau_0$, $D_0 = \frac{k_BT}{V_0}$ and $\hat{\eta}(t) = \sqrt{\tau_0}\eta(t)$.

6.3 Effective Potential

As mentioned earlier our focus is on the result that on time scales larger than the period of perturbation, the dynamics is equivalent to one in which the time dependent periodic perturbation can be replaced by a time independent effective potential [118, 122]. In Sarkar and Dattagupta [118], it has been shown in great detail that the expression of the effective potential does not alter in the presence of noise. We presume and verify that this result is true even when the forcing term is space dependent. Further, unlike [118] we treat the underdamped case from which all the results of [118] can be obtained as a limit.

6.3.1 First Order Correction

It is evident from the nature of the field in which the particle moves that it will traverse a smooth path and at the same time will execute small noisy fluctuations about that path. Accordingly, we represent the function x(t) as a sum:

$$x(t) = X(t) + \xi(t), \tag{6.9}$$

where X(t) is a slow variable and $\xi(X,t)$ is a fast variable. The following transformations then follow:

$$\begin{aligned} \dot{x} &= \dot{X} + \dot{\xi}(X,t), \\ \ddot{x} &= \ddot{X} + \ddot{\xi}(X,t), \\ \frac{\partial}{\partial x} &= \frac{1}{1+\xi'}\frac{\partial}{\partial X}. \end{aligned} \tag{6.10}$$

Now setting the noise term to zero and putting the above transformations in Eq. (6.1) we obtain

$$\begin{aligned} m\Big(\ddot{X}(t) + \ddot{\xi}(X,t)\Big) &= -\gamma\Big(\dot{X}(t) + \dot{\xi}(X,t)\Big) + F(X+\xi,t) \\ &\quad -\frac{1}{1+\xi'}\frac{\partial}{\partial X}U(X+\xi). \end{aligned} \tag{6.11}$$

To find the effective potential experienced by the particle correct to first order, we perform a Taylor series expansion of Eq. (6.11) upto first order. Thus,

$$\begin{aligned} m\ddot{X}(t) + m\ddot{\xi}(X,t) &= -\gamma\dot{X}(t) - \gamma\dot{\xi}(X,t) \\ &- \frac{1}{1+\xi'}\frac{\partial}{\partial X}(U(X) + \xi U'(X)) \\ &+ F(X,t) + \xi F'(X,t). \end{aligned} \tag{6.12}$$

The above Eq. (6.12) involves both 'fluctuating' and 'smooth' terms on the left and right sides which must be separately equal. For the fluctuating terms we can simply put

$$m\ddot{\xi}(t) + \gamma\dot{\xi}(t) = F(X,t), \tag{6.13}$$

where we take [117] $F(X,t) = f(X)\cos(\omega t) + g(X)\sin(\omega t)$. Solving Eq. (6.13) we obtain,

$$\begin{aligned} \xi(X,t) &= \frac{1}{m(\omega^2 + \frac{\gamma^2}{m^2})}\Big[\Big(f(X) + \frac{\gamma}{m\omega}g(X)\Big)\cos(\omega t) \\ &+ \Big(g(X) - \frac{\gamma}{m\omega}f(X)\Big)\sin(\omega t)\Big]. \end{aligned} \tag{6.14}$$

Since ω is large, $\frac{1}{1+\xi'} \simeq (1-\xi')$ is effective. Next combining Eq. (6.13) with Eq. (6.12) and then averaging over a time period we finally obtain

$$m\ddot{X}(t) + \gamma\dot{X}(t) = -\frac{\partial U(X)}{\partial X} + < \xi F'(X,t) >, \tag{6.15}$$

where

$$\begin{aligned} < \xi F'(X,t) > &= -\frac{1}{4m\Big(\omega^2+\frac{\gamma^2}{m^2}\Big)}\Big[\frac{\partial}{\partial X}(f^2(X)+g^2(X)) \\ &\quad +\frac{2\gamma}{m\omega}(f'(X)g(X)-g'(X)f(X))\Big]. \end{aligned} \tag{6.16}$$

With the help of Eq. (6.16) we can rewrite Eq. (6.15) as follows

$$\begin{aligned} m\ddot{X}(t)+\gamma\dot{X}(t) &= -\frac{\partial U(X)}{\partial X} \\ &- \frac{1}{4m\Big(\omega^2+\frac{\gamma^2}{m^2}\Big)}\Big[\frac{\partial}{\partial X}(f^2(X)+g^2(X)) \\ &+ \frac{2\gamma}{m\omega}(f'(X)g(X)-g'(X)f(X))\Big], \end{aligned} \tag{6.17}$$

or,

$$m\ddot{X}(t)+\gamma\dot{X}(t) = -\frac{\partial U_{eff}(X)}{\partial X}, \tag{6.18}$$

with $U_{eff}(X) = U(X) + U^1(X)$, where

$$\begin{aligned} U^1(X) &= \frac{1}{4m\Big(\omega^2+\frac{\gamma^2}{m^2}\Big)}\Big[\frac{\partial}{\partial X}(f^2(X)+g^2(X)) \\ &+ \frac{2\gamma}{m\omega}\int^X dy(f'(y)g(y)-g'(y)f(y))\Big]. \end{aligned} \tag{6.19}$$

It is clear that $U^1(X)$ vanishes for space-independent forcing, as in [118].

6.3.2 Second Order Correction

To find the second order correction term in the effective potential the transformation equations given in Eq. (6.10) have to be modified as

$$\begin{aligned} x &= X+\xi(X,t)+\xi(X,t)\xi'(X,t), \\ \dot{x} &= \dot{X}+\dot{\xi}+\dot{\xi}\xi'+\xi\dot{\xi}', \\ \ddot{x} &= \ddot{X}+\ddot{\xi}+\ddot{\xi}\xi'+\xi\ddot{\xi}'+2\dot{\xi}\dot{\xi}', \\ \frac{\partial}{\partial x} &= \frac{1}{1+\xi'+\xi'^2+\xi\xi''}\frac{\partial}{\partial X}. \end{aligned} \tag{6.20}$$

Putting the above transformation in Eq. (6.1) and retaining terms upto second order in ξ (O(ξ^2)) we derive

$$\begin{aligned} m\Big(\ddot{X}+\ddot{\xi}+\ddot{\xi}\xi'+\xi\ddot{\xi}'+2\dot{\xi}\dot{\xi}'\Big) &= -\gamma\Big(\dot{X}+\dot{\xi}+\dot{\xi}\xi'+\xi\dot{\xi}'\Big) \\ &\quad -(1-\xi'-\xi'^2-\xi\xi'')\Big[U'(X) \\ &\quad +U''(X)\xi+U'(X)\xi'+U''(X)\xi\xi'+U'(X)\xi'^2 \\ &\quad +U'(X)\xi\xi''+\frac{1}{2}U'''(X)\xi^2+U''(X)\xi\xi'\Big]+F(X,t) \\ &\quad +\xi F'(X,t)+\xi\xi' F'(X,t)+\frac{1}{2}\xi^2 F''(X,t). \end{aligned}$$

Next, after performing time averaging we ultimately obtain

$$\begin{aligned} m\ddot{X}+\gamma\dot{X} &= -U'(X)+U'(X)<\xi'^2> \\ &- \frac{1}{2}\frac{\partial}{\partial X}(U''(X)<\xi^2>)+<\xi F'(X,t)> \\ &= -\frac{\partial U_{eff}}{\partial X}, \end{aligned} \tag{6.21}$$

with $U_{eff}(X)=U(X)+U^1(X)+U^2(X)$, where U(X) is the systematic periodic potential, $U^1(X)$ is the first order correction to the effective potential given by Eq. (6.19) and the second order correction to the effective potential is given by

$$\begin{aligned} U^2(X) &= \frac{1}{4m^2\omega^2(\omega^2+\frac{\gamma^2}{m^2})}\Big[(f^2(X)+g^2(X))U''(X) \\ &- 8\int^X dy\Big(f'^2(y)+g'^2(y)\Big)\Big]. \end{aligned} \tag{6.22}$$

The results for $U^1(X)$ and $U^2(X)$ are identical to those obtained by Dutta and Barma [117] who have however employed a Fokker-Planck equation approach.

With the help of Eq. (6.19) and Eq. (6.22) we calculate the first order and second order correction terms for the periodic potential $V(x)$ and ultimately obtain the effective potential $V_{eff}(x)=V(x)+V^1(x)+V^2(x)$ which are given by, for the space independent case

$$\begin{aligned} V_{eff}(x) &= \Big(\frac{a^2}{4m^2\omega^2(\omega^2+\frac{\gamma^2}{m^2})}-1\Big)\sin(x) \\ &\quad +\mu\sin(2x)\Big(\frac{a^2}{m^2\omega^2(\omega^2+\frac{\gamma^2}{m^2})}-1\Big), \end{aligned} \tag{6.23}$$

and for the space dependent case

$$\begin{aligned} V_{eff}(x) &= \Big(\frac{a^2x^2}{4m^2\omega^2(\omega^2+\frac{\gamma^2}{m^2})}-1\Big)\sin(x) \\ &\quad +\mu\sin(2x)\Big(\frac{a^2x^2}{m^2\omega^2(\omega^2+\frac{\gamma^2}{m^2})}-1\Big) \\ &\quad +\frac{a^2x}{m(\omega^2+\frac{\gamma^2}{m^2})}(\frac{1}{2}-\frac{2}{m\omega^2}), \end{aligned} \tag{6.24}$$

where $F(x,t) = a\cos(\omega t)$ and $ax\cos(\omega t)$ for the space independent and space dependent cases respectively. In Fig. (6.1) we plot the periodic systematic ratchet potential

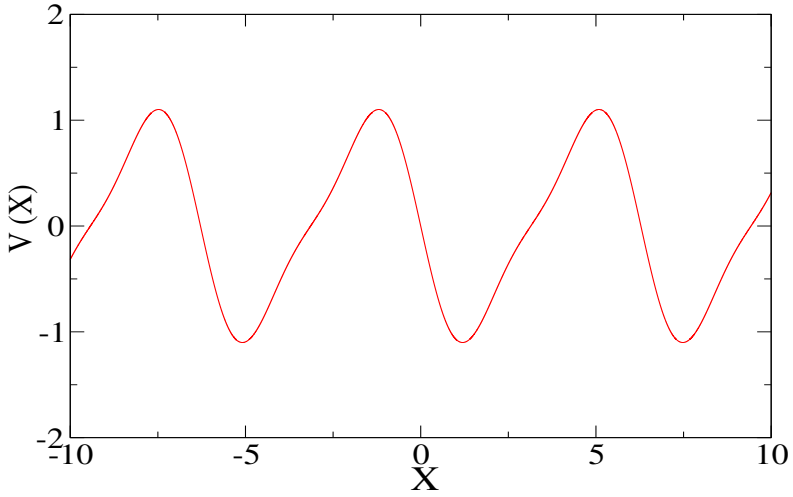

Figure 6.1: The periodic potential V(x).

$V(x) = -\sin(x) - \mu\sin(2x)$ with $\mu = \frac{1}{4}$. In Fig. (6.2) and Fig. (6.3) we plot the effective potential for the space independent and space dependent external force respectively. In the next section we further extend this analysis by using these results for calculating the effective diffusion enhancement and transport current.

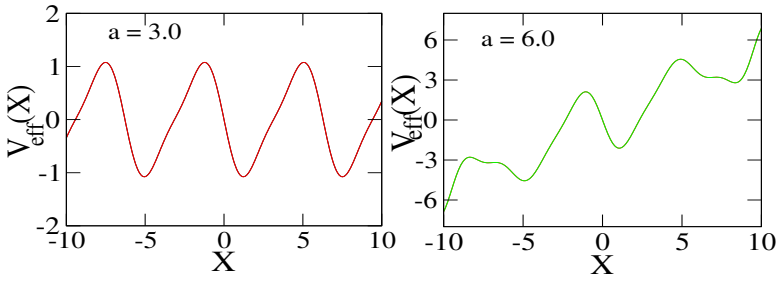

Figure 6.2: The effective potential $V_{eff}(x)$ when external force is space independent.

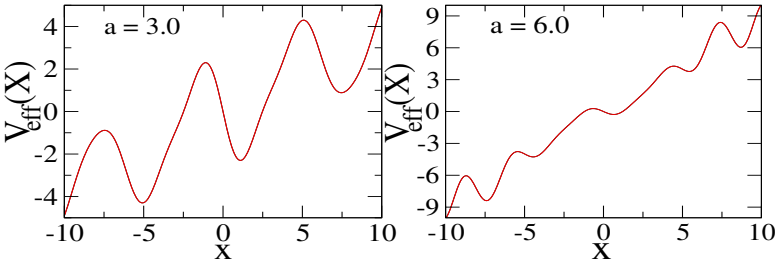

Figure 6.3: The effective potential $V_{eff}(x)$ when external force is space dependent.

6.4 Numerical Scheme and Results

We numerically solve Eqs. (6.7) and (6.8) with the aid of the Heun scheme which is basically the Runge-Kutta algorithm. Our main interest, as emphasized earlier, is to compute the effective diffusion coefficient which we do using Eq. (6.5). We calculate this quantity for the original dynamics and effective dynamics for the two special cases: (a) space dependent external periodic force and (b) constant amplitude external periodic force. We have taken upto second order correction term in solving the effective dynamics. There are four dimensionless parameters a,b, D_0, and ω (defined earlier in terms of physical quantities) and to define effective potential we need to specify three more parameters m, γ and μ. We

fix $b = 0.1, \omega = 5.0, m = 1.0, \gamma = 0.1, \mu = 0.25$ and $D_0 = 0.025$ throughout this work and vary the parameter 'a'. In Fig. (6.4) we have plotted effective diffusion coefficient versus external force field strength ('a') for both the space dependent and space independent cases. In both cases, the enhancement of effective diffusion coefficient as a function of the

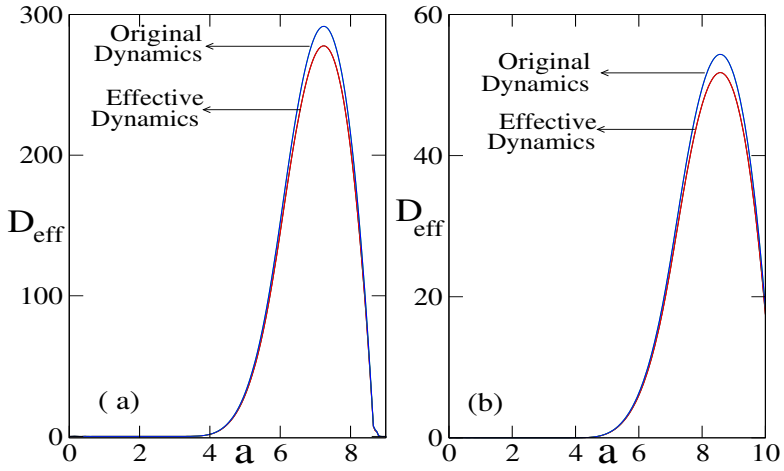

Figure 6.4: The effective diffusion coefficient for original and effective dynamics for two cases (a) space dependent (b) space independent external periodic force. The parameters which we use for this numerical calculation are $b = 0.1, \omega = 5.0, D_0 = 0.025, m = 1.0$ and $\gamma = 0.1$.

amplitude 'a' is clearly noticeable. In the absence of the external force, $D = 2.34 \times 10^{-10}$, (calculated using Eq. (6.6)) and it agrees very well with the Heun scheme results when 'a' = 0. From Fig. (6.4) it is evident that the effective diffusion coefficient in a periodic potential in the presence of an externally applied oscillating force can be larger than in the absence of the external force by about twelve orders of magnitude, for certain values of 'a'. This enhancement is however about 4 orders of magnitude higher than the free diffusion coefficient (D_0). The enhancement is more pronounced for the space dependent external periodic force than the constant amplitude external periodic force due to the extra terms in effective potential for the space dependence of the external force.

It is known that there are two states of a driven Brownian dynamical system: the locked

state, in which the particle stays inside one potential well, and the running state, for which the particle runs over the potential barriers. The first regime is characteristic of a small driving force strength. When the amplitude of the external field is made large, a running state appears where we can see both diffusive and regular behavior of the particle. The most interesting feature in Fig. (6.4) is the resonance like behaviour of the diffusion coefficient. This leads to the existence of an optimal 'a' for the enhancement of the diffusion rate. This phenomena is reminiscent of stochastic resonance (SR) [125-127]. So we can hereby employ the acronym "SR" to imply acceleration of diffusion. By this we mean that a new diffusion mechanism, with combined action of noise, spatially periodic potential and time-periodic modulation can be more effective than that of free Brownian motion, since D_{eff} is shown to exceed unity in a large region around some optimal parameter regions. In these regions the optimal matching of the periodic force and noise drive the particles up the potential hills during each time period. Then these particles scatter at the potential barriers and finally they diffuse very quickly into wide regions. Therefore in order to get the above mentioned diffusion enhancement we need the optimal collective actions of three forces —- spatially periodic force, time periodic modulation and stochastic stimulation. Further we should emphasize that the extra terms in the effective potentials due to space dependence of the external force do indeed aid this diffusion enhancement mechanism.

We have also studied the current 'J' which is defined as the time average of the average velocity over an ensemble of initial conditions. Thus it involves two different averages, the first is over M initial conditions, which we take randomly centered around the origin and with an initial velocity equal to zero. For fixed time t_j we calculate the average velocity $v_j = \frac{1}{M}\sum_{i=1}^{M} \dot{x}_i(t_j)$. The second average is over time and yields $J = \frac{1}{N}\sum_{j=1}^{N} v_j$. All quantities of interest are averaged over 250 different trajectories and 10^4 periods. In solving effective dynamics we have used upto second order correction term of effective potential for both space dependent and space independent cases. In Fig. 6.5 we have shown the behavior of the transport currents in case of space dependent external force. Initially the current is zero, following which it increases and peaks at some optimal values of 'a', then decreases with the increase of 'a'. The following explanation will help to understand the behavior of current. At very low force strength, escape jumps between the neighbouring

wells are very rare i.e. the average directed current is very small. The input energy is

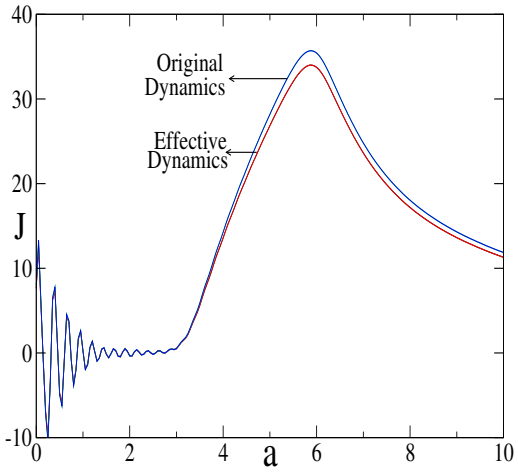

Figure 6.5: The current J of the inertial rocked Brownian motor when external force is space dependent. The parameters which we use for this numerical calculation are $b = 0.1, \omega = 5.0, D_0 = 0.025, m = 1.0$ and $\gamma = 0.1$.

mostly expanded into the kinetic energy of the intrawell motion and eventually dissipates. As 'a' is increased further, the Brownian motor mechanism starts to work and some part of energy contributes to the net motion of the particle. Now due to inertia, the mean velocity increases and reaches a maximum. Then 'a' reaches a second threshold value above which the current starts to decrease because of the debilitating effect of the ratchet potential. The occurrence of multiple reversals of the directed current, as is shown in the Fig. 6.5 and Fig. 6.6 for low force strength, is an interesting feature of the inertial Brownian motor system [128-133]. The phenomenon of current reversals can be described by different stability properties of the perturbed rotating orbits of the system [131]. Current reversals are also associated to bifurcations from chaotic to periodic orbits, in some cases, as discussed by Mateos [130].

By comparing the figures (6.5) and (6.6) we can surmise that the current is much more substantial for the space dependent external force case. Extra terms in the effective potential arising from space dependence of the external force do help in increasing the current.

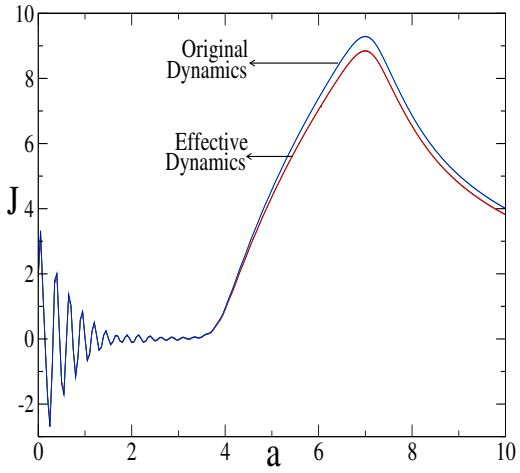

Figure 6.6: The current J of the inertial rocked Brownian motor when external force is space independent. The parameters which we use for this numerical calculation are $b = 0.1, \omega = 5.0, D_0 = 0.025, m = 1.0$ and $\gamma = 0.1$.

6.5 Summary and Conclusions

In this section we present an overview of the principal results of this chapter. We have addressed the problem of underdamped Brownian particle in a position dependent periodic driving force in the high frequency regime. We have then calculated the effective potential upto second order in the expansion parameter ξ and used these results to calculate the effective diffusion coefficient and transport current. In the high frequency regime the particle makes small but rapid excursions around a smooth path along which the motion is relatively slow. A systematic perturbative treatment in powers of the excursion amplitude shows that the first order correction in the effective potential exists only if the externally applied rapidly oscillating field is space dependent. This first order correction term (Eq. (6.19)) is the average kinetic energy which contributes to the work done against damping. The second order correction to the effective potential shows that a nontrivial contribution

arises even for position independent driving.

We have employed our derived results for the calculation of the effective diffusion coefficient and transport current. We obtained the effective diffusion coefficient by solving both the original dynamics and effective dynamics. We noted a giant enhancement of diffusion and the results arising from original and effective dynamics agree very well. This validates our method of calculation in the high frequency regime. The enhancement of diffusion is a result of the optimal collective actions of spatially periodic gradients, time periodic modulation and thermal noise. The enhancement is much more pronounced for the space dependent periodic external force which can be understood in terms of the extra terms arising in the effective potential from the space dependence of external force. We have analyzed the transport properties and the behavior of current for the Brownian motor mechanism and compared the currents for two cases: space dependent and space independent external forces. The current is larger for the space dependent case.

In a recent paper, Coupier *et al* [134] have shown experimentally the diffusion enhancement of a single file of particles moving in a fluctuating modulated quasi-1D channel. They observed diffusion of a circular file of particles for two different channels guiding the particles : a fluctuating modulated channel created by other particles and a bald channel without any modulation. The diffusion amplitude in a fluctuating potential is much larger than in a bald channel. We have shown [101] that diffusion of a single particle in a modulated potential can be largely enhanced if the particle is excited by a rapid fluctuating force. In the same way Coupier *et al* [134] have attributed the diffusion increase to the fluctuations of the modulated potential felt by the outer balls. The fluctuating part of the force is being associated with the momentum transfers resulting from the oscillations of the balls located in the inner shell.

Finally we would like to emphasize once again the practical implications of this work. The parameters which enter the effective potential can be used to separate different species of Brownian particles by identifying the minima of the effective potential. One can control the diffusion rates by varying periodic spatial gradients and the space dependent external field. In addition to myriad applications mentioned earlier, systems described by Eq. (6.1) are realized for charged particles moving on thermal surfaces under periodic potentials subjected to time varying fields. Recent motivation to study these systems has been

inspired by the theoretical modelling of the molecules called kinesin and myosin, which possess the ability to move unidirectionally along structural filaments of microtubulin and actin.

Chapter 7

Dissipative Diamagnetism : Gibbs Approach to Equilibrium Statistical Mechanics.

7.1 Introduction

Diamagnetism, which occurs as a result of the orbital motion of electric charges in the presence of a magnetic field, is an interesting and important problem. It was shown by Bohr and Van Leeuwen that when classical statistical mechanics are applied to the calculation of the diamagnetic moment, the answer is identically zero [135]. Thus, diamagnetism is an intrinsically quantum mechanical property, the treatment for which was provided by Landau after the advent of quantum mechanics [136]. There is an interesting issue of the role of the boundary within which the charges move, as was studied in depth by Van Vleck and Peierls [137, 138]. While in classical statistical mechanics the contribution to the diamagnetic moment arising from the orbiting charges within the bulk of the container exactly cancels the contribution coming from the boundary-currents, this cancellation is incomplete in the quantum case, yielding a non-zero value of the diamagnetic moment. The boundary currents or edge currents are also important in the context of the quantum Hall effect [139]. In an earlier work, Dattagupta and Singh [140] discussed the role of dissipation in diamagnetism. Because the diamagnetic moment is proportional to the expectation value of the vector product of the operators $\vec{r}$ and $\vec{v}$, $\vec{r}$ being the position of the charge and $\vec{v}$ its velocity, the calculation was set up as a transport problem, much like the celebrated Drude conductivity of charge carriers [141]. Thus, the stationary form of the magnetic moment was obtained from the asymptotic (i.e. time $t \to \infty$) limit of the exact solution of an underlying quantum Langevin equation (QLE) for $\vec{r}$ and $\vec{v}$ [142].

Naturally, the role of the boundary had to be carefully assessed by first solving the QLE in the presence of a confining boundary, then taking the $t \to \infty$ limit for the diamagnetic moment, and finally removing the boundary.

The QLE employed in Dattagupta and Singh [140] is in the spirit of the Caldeira Leggett model for which the harmonic oscillators are viewed to constitute a quantum bath that defines the temperature [143]. Here in Chapter 7 we present an alternative calculation of the diamagnetic moment, which is now viewed as a thermodynamic property, derivable from the derivative of the Gibbs partition function[144]. Thus the full Hamiltonian comprising the charged particle in a magnetic field, the harmonic oscillators and their coupling, is treated in the canonical ensemble of equilibrium statistical mechanics. For reasons mentioned earlier, a confining boundary has to be also included, which is to be eliminated only after the derivative of the partition function is computed. In the present calculation, the temperature T is that of an 'invisible' bath in which the canonical system is viewed to be embedded. While Dattagupta and Singh [140] have considered only the ohmic dissipation in the Caldeira-Leggett model, both non-ohmic and ohmic cases are treated here. We may point out that the combined effect of dissipation and confinement on Landau diamagnetism, the latter arising from coherent cyclotron motion of the electrons, is particularly relevant in the context of intrinsic decoherence in mesoscopic structures and fluctuation induced diamagnetic susceptibility and conductivity in superconducting systems [139, 146-149].

7.2 Model, Formalism and Effective Action

The starting point of Dattagupta and Singh [140] as indeed in this section is the Feynman-Vernon [150] Hamiltonian for a charged particle e in a magnetic field $\vec{B}$:

$$\mathcal{H} = \frac{1}{2M}\omega_0^2\vec{x}^2 + \frac{1}{2M}\Big(\vec{p} - \frac{e\vec{A}}{c}\Big)^2 + \sum_{j=1}^{N}\Big[\frac{1}{2m_j}\vec{p_j}^{\,2} + \frac{1}{2}m_j{\omega_j}^2(\vec{x}_j - \vec{x})^2\Big], \tag{7.1}$$

where the first term is the Darwin [151] term representing a confining potential to recover the correct boundary contribution, $\vec{p}$ and $\vec{x}$ are the momentum and position operators of the particle, $\vec{p_j}$ and $\vec{x}_j$ are the corresponding variables for the bath particles, and $\vec{A}$ is the vector potential. We will work in the 'Symmetric Gauge'. The bilinear coupling

between $\vec{x}$ and $\vec{x}_j$ as envisaged in Eq. (7.1) has been the hall mark of the Caldeira-Leggett approach to dissipative quantum mechanics [143, 152]. Further, it has been shown by Chang and Chakravarty that a fermionic heat bath for electron-hole excitations near the Fermi surface, as appropriate for a metal, can indeed be represented by bosonic operators, which are just the second quantized forms of the harmonic oscillator variables of the Caldeira Leggett model, especially when ohmic dissipation is assumed [153]. Assuming the $\vec{B}$ field to be along the z-axis, all the vectors in Eq. (7.1) can be taken to lie in the xy-plane. Thus, the vector $\vec{x}$ has two components x and y etc.

Using the imaginary time path integral method we calculate the effective Euclidean action. The partition function of the whole system is given by

$$\mathcal{Z} = \int D[\vec{x}] \exp\Big[- \frac{\mathcal{A}_e[\vec{x}]}{\hbar}\Big], \tag{7.2}$$

where $\mathcal{A}_e[\vec{x}]$ is the effective Euclidean action and the functional integral is over all periodic paths with period $\hbar\beta$. The free energy is then given by

$$\mathcal{F} = -\frac{1}{\beta} ln \mathcal{Z}. \tag{7.3}$$

The important thermodynamic quantity, viz., the magnetization can easily be obtained by taking the first derivative of $\mathcal{F}$ with respect to the magnetic field B, applied along the z-axis:

$$\mathcal{M}_z = -\frac{\partial \mathcal{F}}{\partial B}. \tag{7.4}$$

Having laid down the background to the calculation of diamagnetism we pose and answer the following question in this part. Should we not be able to calculate the equilibrium magnetization directly from Eq. (7.1) by following the usual Gibbsian statistical mechanics in which all the terms in Eq. (7.1) are treated on the same footing and there is no separation between what is a system and what is a bath? If the answer to this question is in the affirmative and the resultant magnetization matches with the result derived in Dattagupta and Singh [140] in the 'equilibrium limit', that would indeed make the Brownian motion approach of Dattagupta and Singh [140] equivalent to the usual statistical mechanics method.

Our method of calculation is based on the functional integral approach to statistical

mechanics which we find to be the most convenient tool for studying charged particle dynamics in a magnetic field [154-158]. The canonical operator $\exp(-\beta\mathcal{H})$ is related to the time evolution operator $\exp(-\frac{i\mathcal{H}t}{\hbar})$ by an analytic continuation procedure known as Wick's rotation $t = -i\hbar\beta$. So in order to obtain the Euclidean action we have to analytically continue to imaginary time $\tau = it$. The Euclidean action corresponding to the Hamiltonian in Eq. (7.1) can be written as :

$$\mathcal{A}_e = \int_0^{\hbar\beta} d\tau[\mathcal{L}_S(\tau) + \mathcal{L}_B(\tau) + \mathcal{L}_I(\tau)], \tag{7.5}$$

where the subscripts S, B and I stand for 'system', 'bath' and 'interaction' respectively. The corresponding Lagrangians are enumerated as:

$$\mathcal{L}_S(\tau) = \frac{M}{2}\Big[\dot{\vec{x}}^2(\tau) + \omega_0^2\vec{x}^2(\tau) - i\omega_c(\vec{x}(\tau) \times \dot{\vec{x}}(\tau))_z\Big], \tag{7.6}$$

where $\omega_c = \frac{eB}{Mc}$, is the cyclotron frequency,

$$\mathcal{L}_B(\tau) = \sum_{j=1}^{N} \frac{1}{2} m_j[\dot{\vec{x}}_j^2(\tau) + \omega_j^2\vec{x}_j^2(\tau)], \tag{7.7}$$

$$\mathcal{L}_I(\tau) = \sum_{j=1}^{N} \frac{1}{2} m_j\omega_j^2[\vec{x}^2(\tau) - 2\vec{x}_j(\tau) \cdot \vec{x}(\tau)]. \tag{7.8}$$

Since the path $x(\tau)$ has imaginary time periodicity $x(\hbar\beta) = x(0)$, we can perform imaginary time Fourier series expansion of system variables and bath variables as follows:

$$\vec{x}(\tau) = \sum_n \vec{\tilde{x}}(\nu_n)e^{-i\nu_n\tau}, \tag{7.9}$$

$$\vec{x}_j(\tau) = \sum_n \vec{\tilde{x}}_j(\nu_n)e^{-i\nu_n\tau}, \tag{7.10}$$

where the Bosonic Matsubara frequencies ν_n are given by

$$\nu_n = \frac{2\pi n}{\hbar\beta}, \quad n = 0, \pm1, \pm2, ..., \tag{7.11}$$

Using Eqs. (7.9) and (7.10) and following the detailed treatment given by Weiss [157] the system-part of the action in terms of Fourier components is:

$$\mathcal{A}_e^S = \frac{M}{2}\hbar\beta \sum_n \Big[(\nu_n^2 + \omega_0^2)(\vec{\tilde{x}}(\nu_n) \cdot \vec{\tilde{x}}^*(\nu_n)) + \omega_c\nu_n(\vec{\tilde{x}}(\nu_n) \times \vec{\tilde{x}}^*(\nu_n))_z\Big]. \tag{7.12}$$

Further the combined contributions of the bath and the interaction terms to the action can be written as:

$$\mathcal{A}_e^{B-I} = \frac{M}{2}\hbar\beta\sum_n \xi(\nu_n)(\vec{\tilde{x}}(\nu_n)\cdot\vec{\tilde{x}}^*(\nu_n)), \tag{7.13}$$

where

$$\xi(\nu_n) = \frac{1}{M}\sum_{j=1}^{N} m_j\omega_j^2\frac{\nu_n^2}{(\nu_n^2+\omega_j^2)}. \tag{7.14}$$

Introducing the spectral density for bath excitations as:

$$J(\omega) = \frac{\pi}{2}\sum_{j=1}^{N} m_j\omega_j^3\delta(\omega-\omega_j), \tag{7.15}$$

we may rewrite

$$\xi(\nu_n) = \frac{2}{M\pi}\int_0^\infty d\omega\frac{J(\omega)}{\omega}\frac{\nu_n^2}{(\nu_n^2+\omega^2)}. \tag{7.16}$$

Now, combining Eq. (7.13) with Eq. (7.12), the full action can be expressed as:

$$\mathcal{A}_e = \frac{M}{2}\hbar\beta\sum_n\Big[(\nu_n^2+\omega_0^2+\nu_n\tilde{\gamma}(\nu_n))(\vec{\tilde{x}}(\nu_n)\cdot\vec{\tilde{x}}^*(\nu_n)) + \omega_c\nu_n(\vec{\tilde{x}}(\nu_n)\times\vec{\tilde{x}}^*(\nu_n))_z\Big], \tag{7.17}$$

where the 'memory-friction' is given by

$$\tilde{\gamma}(\nu_n) = \frac{2}{M\pi}\int_0^\infty d\omega\frac{J(\omega)}{\omega}\frac{\nu_n}{(\nu_n^2+\omega^2)}. \tag{7.18}$$

Note that $\vec{\tilde{x}}(\nu_n)$ is a two-dimensional vector $(\tilde{x}(\nu_n),\tilde{y}(\nu_n))$. Introducing then normal modes:

$$\begin{aligned}\tilde{z}_+(\nu_n) &= \frac{1}{\sqrt{2}}(\tilde{x}(\nu_n)+i\tilde{y}(\nu_n))\\ \tilde{z}_-(\nu_n) &= \frac{1}{\sqrt{2}}(\tilde{x}(\nu_n)-i\tilde{y}(\nu_n)),\end{aligned} \tag{7.19}$$

Eq. (7.17) can be rewritten in a 'separable' form:

$$\begin{aligned}\mathcal{A}_e &= \frac{M}{2}\hbar\beta\sum_n\Big[(\nu_n^2+\omega_0^2+\nu_n\tilde{\gamma}(\nu_n)+i\omega_c\nu_n)(\tilde{z}_+(\nu_n)\tilde{z}_+^*(\nu_n))\\ &\quad +(\nu_n^2+\omega_0^2+\nu_n\tilde{\gamma}(\nu_n)-i\omega_c\nu_n)(\tilde{z}_-(\nu_n)\tilde{z}_-^*(\nu_n))\Big].\end{aligned} \tag{7.20}$$

Equation (7.20) is the required effective Euclidean action.

7.3 Free Energy and Magnetization.

In this section we employ the action given by Eq. (7.20) to first calculate the canonical partition function and from it, the thermodynamic free energy. In doing this calculation we tacitly assume *a la* Gibbs that the entire Hamiltonian, described by Eq. (7.1), is embedded in a thermal bath that defines the temperature of the system. This is in contrast to the QLE approach in Dattagupta and Singh [140] which assumes that it is the subsystem alone, comprising the electron in a magnetic field, that is immersed in a heat bath of quantum harmonic oscillators.
From Eq. (7.20) the partition function can be written as:

$$\mathcal{Z} = \frac{2\pi}{M\beta}\prod\nolimits_n \Big[(\nu_n^2 + \omega_0^2 + \nu_n\tilde{\gamma}(\nu_n))^2 + \omega_c^2\nu_n^2\Big]^{-1}, \tag{7.21}$$

where, we have used the definition of partition function as given in Eq. (7.2). In view of Eq. (7.3) the Helmholtz Free energy $\mathcal{F}$ can be deduced from Eq. (7.21) as

$$\mathcal{F} = \frac{1}{\beta}\ln\Big(\frac{M\beta\omega_0^4}{2\pi}\Big) + \frac{2}{\beta}\sum_{n=1}^{\infty}\ln\Big[(\nu_n^2 + \omega_0^2 + \nu_n\tilde{\gamma}(\nu_n))^2 + \omega_c^2\nu_n^2\Big], \tag{7.22}$$

where the first term is independent of the magnetic field and owes its existence purely to the Darwinian constraining potential. Equation (7.22) contains all the thermodynamic properties, the most important of which is the *magnetization* given by the negative derivative of $\mathcal{F}$ with respect to B :

$$\mathcal{M}_z = -\sum_{n=1}^{\infty}\frac{\frac{4}{\beta B}\omega_c^2\nu_n^2}{[(\nu_n^2 + \omega_0^2 + \nu_n\tilde{\gamma}(\nu_n))^2 + \omega_c^2\nu_n^2]}, \tag{7.23}$$

thus yielding a manifestly negative magnetization, the hallmark of diamagnetism.We additionally note that the dissipative system of a charged quantum oscillator in an external magnetic field is still diamagnetic. Equation (7.23) identically matches with the asymptotic ($t \to \infty$) limit of the expression obtained by Li *etal* [142] from a quantum Langevin equation formulation. Equation (7.23) can be recast in terms of dimensionless parameters like $\zeta(=\frac{\hbar\tilde{\gamma}(\nu_n)}{2k_BT})$, $\nu_c(=\frac{\hbar\omega_c}{2k_BT})$ and $\nu_0(=\frac{\hbar\omega_0}{2k_BT})$ as follows:

$$\mathcal{M}_z = -\frac{B}{k_BT}\Big(\frac{e\hbar}{Mc}\Big)^2\sum_{n=1}^{\infty}\frac{1}{[n\pi + \frac{\nu_0^2}{n\pi} + \zeta]^2 + \nu_c^2}. \tag{7.24}$$

In the limit $\nu_0 = 0$ the above equation (7.24) reduces to

$$\mathcal{M}_z = -\frac{|e|\hbar}{Mc}\nu_c \sum_{n=1}^{\infty} \frac{1}{\nu_c^2 + (\zeta + n\pi)^2}. \tag{7.25}$$

It has often been felt, starting from the old Larmor theory of diamagnetism [137], that $\mathcal{M}_z$ ought to be simply proportional to the mean-squared electron radius, as it connects to the square of the vector potential $\vec{A}$ occurring in the Hamiltonian in (1) [147]. In order to explore this connection, we now switchover to the calculation of the dispersion of position in equilibrium states which is given by

$$< x^2 >= \frac{1}{M\beta\omega_0^2} + \frac{2}{M\beta} \sum_{n=1}^{\infty} \frac{\nu_n^2 + \omega_0^2 + \nu_n\tilde{\gamma}(\nu_n)}{\Big[(\nu_n^2 + \omega_0^2 + \nu_n\tilde{\gamma}(\nu_n))^2 + (\nu_n\omega_c)^2\Big]}. \tag{7.26}$$

From Eq. (7.26) it is evident that the mean square radius $< x^2 >$ decreases monotonically with the increasing strength of the dissipative factor ($\tilde{\gamma}(\nu_n)$). Combining Eq. (7.26) with Eq. (7.23) we obtain

$$\mathcal{M}_z = -\frac{2B}{Mc}\Big[< x^2 > -\frac{1}{M\beta\omega_0^2} - \frac{2}{M\beta} \sum_{n=1}^{\infty} \frac{\omega_0^2 + \nu_n\tilde{\gamma}(\nu_n)}{\Big[(\nu_n^2 + \omega_0^2 + \nu_n\tilde{\gamma}(\nu_n))^2 + (\nu_n\omega_c)^2\Big]}\Big]. \tag{7.27}$$

Even after ignoring the classical equipartition term (i.e. the first term on the right of Eq. (7.26)) we find that $\mathcal{M}_z$ in magnitude is further decreased from $< x^2 >$ by a nontrivial damping dependent term given by a summation over n. This implies actually an increase beyond the value of $< x^2 >$, in view of the overall positive sign in front of the sum over n. The origin of this additional contribution may be traced to the fact that the treatment provided above is an exact one, including the linear term in $\vec{A}$. Be that as it may, the decrease in magnitude of diamagnetization, as the damping increases, may be interpreted to be due to the squeezing of $< x^2 >$ due to dissipation. Thus the present effect is related to how dissipation diminishes the fluctuation induced diamagnetic susceptibility (above T_c) of superconducting grains.

One can also re-express the equilibrium dispersion Eq. (7.26) in terms of dimensionless parameters ζ, ν_c and ν_0

$$< x^2 > \;=\; \frac{\hbar^2}{4Mk_BT}\Big[\frac{1}{\nu_0^2} + \sum_{n=1}^{\infty} \frac{1 + (\frac{\nu_0}{n\pi})^2 + \frac{\zeta}{n\pi}}{[n\pi + \frac{\nu_0^2}{n\pi} + \zeta]^2 + \nu_c^2}\Big]. \tag{7.28}$$

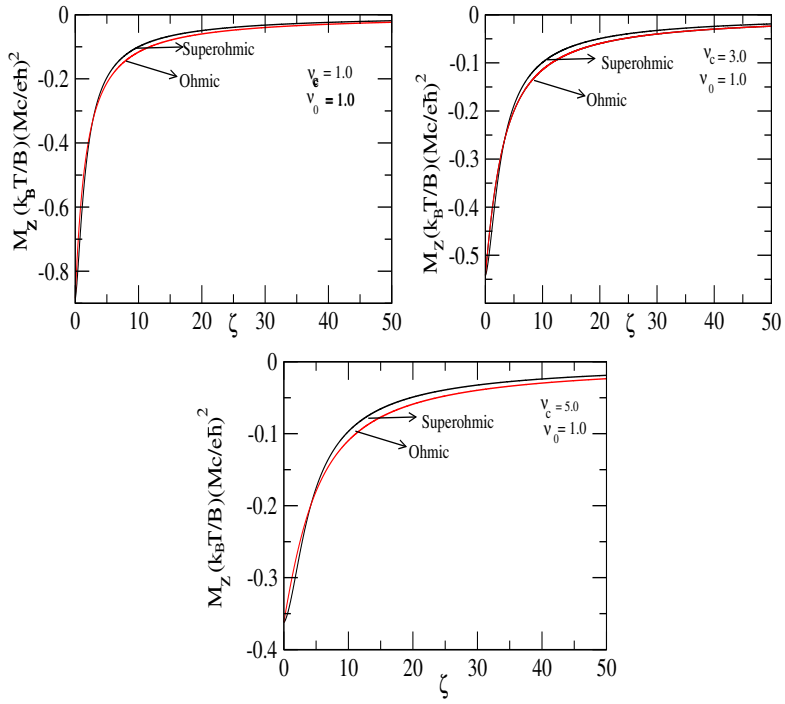

Figure 7.1: Plot of $\frac{2k_BT}{B}\left(\frac{Mc}{e\hbar}\right)^2\mathcal{M}_z$ versus the damping parameter ζ for the both ohmic (J(ω) $\sim \omega$) and nonohmic (J(ω) $\sim \omega^3$) cases.

Now to make our theoretical analysis more accessible and more interesting we numerically plots our main results i.e Eq. (7.24) and Eq. (7.28). We consider both the frequency dependent and independent damping cases i.e both nonohmic (J(ω) $\sim \omega^3$) and ohmic (J(ω) $\sim \omega$) dissipation. We plot in Fig. (7.1) magnetization $\mathcal{M}_z$ versus dimensionless damping parameter ζ for different values of ν_c in accordance with Eq. (7.24) . It is seen that $\mathcal{M}_z$ monotonically approaches zero for large value of ζ, although this approach is slower the larger ν_c is. A large value of ν_c gives strong quantum effect which ultimately yields classical like effects when dissipation ζ is strong. In Fig. (7.2) we plot equilibrium position dispersion versus ζ for different values of ν_c. Here $< x^2 >$ decreases monotoni-

cally to zero for large value of ζ, although the behavior of $< x^2 >$ is different from Mz.

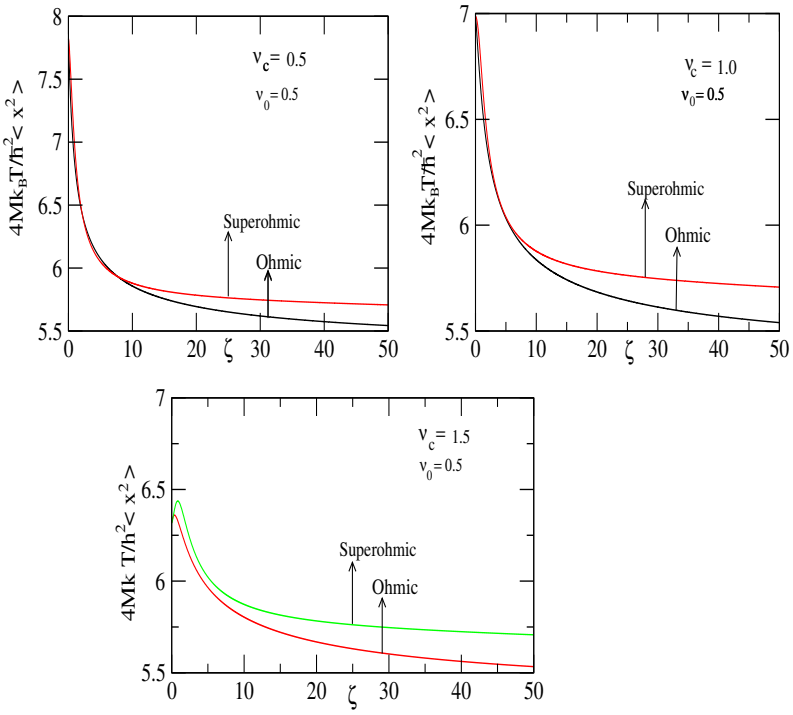

Figure 7.2: Plot of equilibrium position dispersion $< x^2 >$ in unit of $\frac{\hbar^2}{4Mk_BT}$ for both ohmic (J(ω) $\sim \omega$) and nonohmic (J(ω) $\sim \omega^3$) dissipation cases.

7.4 Equilibrium Position Autocorrelation Function

In this section we calculate the position autocorrelation function from the 'equilibrium' Gibbsian ensemble form of the Euclidean action for the Feynmann-Vernon model. This equilibrium position autocorrelation function actually measures the spontaneous fluctuations of the system dgrees of freedom due to coupling with the environment. The position

autocorrelation function in equilibrium is defined as

$$C(t) = \langle \vec{x}(t) \cdot \vec{x}(0) \rangle = Tr((\vec{x}(t) \cdot \vec{x}(0))\rho_\beta), \tag{7.29}$$

where ρ_β is the equilibrium density matrix of the full system and $\vec{x}$ is the two dimensional position vector in the x-y plane.. We determine $C(t)$ by first calculating its imaginary time version starting from the Euclidean action of the system as described by Eq. (7.1)

$$\begin{aligned} S^E[\vec{x}] &= \int_0^{\hbar\beta} d\tau \Big(\frac{m}{2}\dot{\vec{x}}^2 + \frac{m}{2}\omega_0^2 \vec{x}^2 + im\omega_c(\dot{\vec{x}} \times \vec{x})_z \Big) + \frac{1}{2m}\int_0^{\hbar\beta} d\tau \int_0^{\hbar\beta} d\sigma \tilde{\gamma}(\tau - \sigma)\vec{x}(\tau) \cdot \vec{x}(\sigma) \\ &\quad + \int_0^{\hbar\beta} d\tau \vec{f}(\tau) \cdot \vec{x}(\tau), \end{aligned} \tag{7.30}$$

where the first term (within round brackets) takes care of the system part, the second term accounts for the coupling to the environment and the third term corresponds to the interaction with an external force, in imaginary time. This helps us to determine the correlation function by variation with respect to this force [159, 160]

$$\langle \vec{x}(\tau) \cdot \vec{x}(\sigma) \rangle = \hbar^2 Tr\Big(\frac{\delta}{\delta \vec{f}(\tau)} \frac{\delta}{\delta \vec{f}(\sigma)} \rho_\beta \Big)_{\vec{f}=0}. \tag{7.31}$$

It is sufficient to restrict ourselves to the classical path for the calculation of the auto-correlation function [159, 160]. Thus the Fourier representation of the classical Euclidean action becomes [92, 159]

$$\begin{aligned} S_{cl}^E &= -\frac{1}{2m\hbar\beta} \sum_{n=-\infty}^{+\infty} \Big[\frac{1}{\nu_n^2 + \frac{\tilde{\gamma}(|\nu_n|)\nu_n}{m} + \omega_0^2 - i\omega_c\nu_n} + \frac{1}{\nu_n^2 + \frac{\tilde{\gamma}(|\nu_n|)\nu_n}{m} + \omega_0^2 + i\omega_c\nu_n} \Big] \\ &\quad \times \int_0^{\hbar\beta} d\tau \int_0^{\hbar\beta} d\sigma \vec{f}(\tau)\vec{f}(\sigma) \exp(i\nu_n(\tau - \sigma)), \end{aligned} \tag{7.32}$$

where $\nu_n = \frac{2\pi n}{\hbar\beta}$ are the so-called Matsubara frequencies. Since the force appears only through the action in the exponent of the equilibrium density matrix, we can easily evaluate the functional derivatives according to Eq. (7.30) and obtain the position auto-correlation function in imaginary time:

$$C(\tau) = \frac{1}{m\beta} \sum_{n=-\infty}^{+\infty} \Big[\frac{1}{\nu_n^2 + \frac{\tilde{\gamma}(|\nu_n|)\nu_n}{m} + \omega_0^2 - i\omega_c\nu_n} + \frac{1}{\nu_n^2 + \frac{\tilde{\gamma}(|\nu_n|)\nu_n}{m} + \omega_0^2 + i\omega_c\nu_n} \Big] \exp(i\nu_n\tau). \tag{7.33}$$

The real time correlation function cannot be obtained by simply replacing τ by it, because

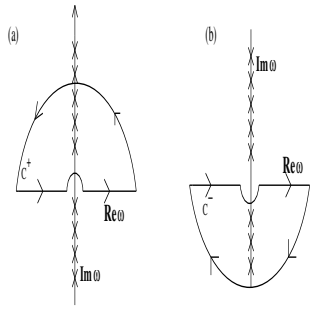

Figure 7.3: The analytic continuation of the imaginary time correlation function to real times by using the contours depicted in (a) and (b) to obtain Eq. (7.34).

for negative times the sum does not converge. The idea is to express the sum in Eq. (7.32) as a contour integral in the complex frequency plane and look for a function which is well-behaved at infinity, but has poles at $\omega = i\nu_n$ [161]. This requirement is fulfilled by the term : $\frac{\hbar\beta}{1-\exp(-\hbar\beta\omega)}$. Now doing the integration along the contour shown in Figs. (7.3-a) and (7.3-b) and after some algebra, we find the real time correlation function as

$$C(t) = \frac{\hbar}{\pi m^2}\int_{-\infty}^{+\infty} d\omega\Big[\frac{\tilde{\gamma}(\omega)\omega}{(\omega^2-\omega_0^2-\omega\omega_c)^2+\frac{\tilde{\gamma}^2(\omega)\omega^2}{m^2}}+\frac{\tilde{\gamma}(\omega)\omega}{(\omega^2-\omega_0^2+\omega\omega_c)^2+\frac{\tilde{\gamma}^2(\omega)\omega^2}{m^2}}\Big] \times\frac{e^{(-i\omega t)}}{1-e^{(-\hbar\beta\omega)}}. \tag{7.34}$$

7.5 Summary and Conclusion

Equation (7.23) embodies several intriguing results which deserve special comments: (1) Diamagnetic susceptibility in small particles is proportional to the mean squared radius $< x^2 >$ of the charged particles in this grain; $< x^2 >$ is squeezed due to dissipation and hence fluctuation induced diamagnetic susceptibility of superconducting grains also decreases. This is an important message of the present work. (2) It has often been seen that while the approach to equilibrium does depend on relaxation parameters such as damping, the equilibrium results themselves are independent of such parameters [162, 163]. The diamagnetization is one of the rare equilibrium properties which depends directly on the damping parameter γ that characterizes the dissipative dynamics of the underlying

Hamiltonian. The reason is, like in the much studied problem of quantum dissipation of a harmonic oscillator [164], the system-bath coupling is so strong that it needs an exact treatment. Thus the degrees of freedom of the entire many body system are inexorably entangled with each other and therefore, it is no longer meaningful to separate what is a system from what is a bath. In this context we should mention that the derivation of Boltzmann distribution $\exp(-\beta\mathcal{H})$ only works in the limit of vanishing interaction strength [165] and indeed this has been discussed for the Caldeira-Leggett model by Benguria et al[166]. But ours is a calculation in which the system-bath interaction has been treated exactly. (3) Diamagnetism as a material property is seen to have components of both thermodynamics and transport phenomena. The thermodynamic nature of the property is rooted on its being able to be calculated from the free energy, as shown here. On the other hand, diamagnetism, like the Drude conductivity [141], is also based on transport mechanism in that it is related to the expectation value of the operator $(\vec{r}\times\vec{v})$ (see Dattagupta and Singh [140]). (4) Normally, in statistical mechanics, a thermodynamic limit is taken as a result of which surface contributions to bulk become irrelevant. However, for diamagnetism the surface enters crucially, as argued above; even though, there are fewer surface electrons than in the bulk, their contribution to the operator $\vec{r}$ in $(\vec{r}\times\vec{v})$ is substantial. A remarkable feature of diamagnetism is the need to first calculate the magnetization in the thermodynamic limit and then switch the boundary off i.e. by setting $\omega_0 = 0$. Because for a mesoscopic system surface effects are non-negligible, the present study has a bearing on our understanding of mesoscopic structures.(5) It has been argued by Jayannavar and Kumar [167], not only is there no classical diamagnetism — due to the Bohr-Van Leeuwen theorem — there is no dissipative classical diamagnetism either. Thus, the time-dependent, classical diamagnetization relaxes to zero, a damping-independent result. Therefore, we emphasize once again that the appearance of damping terms in equilibrium answers, as discussed under points (2) and (5), is an intrinsically quantum aspect. (6) Finally, we have derived the equilibrium position autocorrelation function *a la* of Gibbs. We use this result in the next chapter which is based on the QLE i.e. *a la* Einstein to establish the fluctuation-dissipation relationship in the context of dissipative diamagnetism. We further demonstrate the equivalence of the Einstein and the Gibbs approaches to Statistical Mechanics for the phenomenon i.e. dissipative

diamagnetism at hand.

Chapter 8

Landau-Drude Diamagnetism: Fluctuation, Dissipation and Decoherence.

8.1 Introduction

As discussed in Chapter 7, diamagnetism is a material property that characterizes the response of an ensemble of charged particles to an applied magnetic field. The magnetic field causes cyclotron motion of each particle, thereby creating an orbital magnetic moment, governed by Faraday-Lenz's law. Thus the system exhibits a negative magnetic susceptibility, the hallmark of diamagnetism. But the remarkable feature is that the diamagnetism vanishes within the framework of classical Gibbsian statistical mechanics which is known as the celebrated Bohr-Van Leeuwen's (BVL) theorem [135]. The quantum result for nonvanishing diamagnetism is little hard to explain intuitively. It arises from the fact that the boundary electrons have different quantized velocities than those which do not touch the walls of the container, and so the magnetic moments of these two types of electrons do not compensate each other as in classical theory. Classically both types have the Maxwell-Boltzmann distribution of velocities.

The problem of diamagnetism which was first solved by Landau [136] in 1930 is still an enigmatic subject. The Landau diamagnetism provides a unique platform for discussing the contemporary relevant issues like the role of boundary, dissipation, the meaning of thermodynamic limits and above all the environment induced decoherence. In the chapter 7 we have analyzed the role of boundary electrons, dissipation and the meaning of thermodynamic limits. In the present chapter we want to discuss the consequences of coupling of a system to its environment[168]. Mainly three types of effect can be observed

due to the environmental coupling. First, energy may irreversibly be transferred from the system to the environment in the manner of dissipation [143, 169, 170]. Second, the spontaneous fluctuations in the system in thermodynamic equilibrium, maintained by its coupling to the environment, govern the response of the system degrees of freedom to weak, external stimuli [157, 158]. Finally the entanglement between the system and the environment degrees of freedom destroys the coherent superposition of quantum states, leading to decoherence [171].

We discuss all the three above mentioned effects in the context of Landau diamagnetism which is inherently and intrinsically quantum in nature. For the purpose of investigating fluctuation, dissipation and decoherence in what we call Landau-Drude diamagnetism [13, 168] it is convenient to use the formulation given by Ford et al [172, 173], following the classical treatment due to Zwanzig [174]. Starting from the Feynman-Vernon model in which a particle moving in an arbitrary potential is assumed to be linearly coupled to a collection of quantum harmonic oscillators [154], these authors derive a quantum Langevin equation (QLE). We use this QLE as the basis of our further discussion, in what may be referred to as the Einstein approach to Statistical Physics [145].

At this stage it is important to indicate in what ways is our present work an advancement on existing results in the literature, in order to put matters in perspective. Ford et al [175] had solved the problem of a charged oscillator in a harmonic potential well and linearly coupled to a heat bath using the generalized QLE. This solution was further extended by Li et al [173] but in the presence of a magnetic field. From the asymptotic expression, which obtains in the limit of time t approaching infinity, these authors derived the influence of dissipation on the diamagnetic moment. While the diamagnetism is the first moment of an underlying quantum distribution function, we go beyond this in the present discussion by treating the fluctuations in the asymptotic state, embodied in the generalised susceptibility tensor. We further connect the latter, derived from a 'non-equilibrium' QLE approach, to the position autocorrelation function calculated from the 'equilibrium' Gibbsian ensemble form of the Euclidean action for the Feynmann-Vernon model in the previous chapter (Eq. 7.33). This connection allows us to establish a relation between the position autocorrelation function and the imaginary part of the susceptibility —- a statement of the fluctuation-dissipation theorem, and thus unify equilibrium and

non-equilibrium statistical mechanics, in the context of dissipative diamagnetism. This is a new result.

The destruction of quantum coherence by environment-induced dissipation is of central interest in atomic physics [176], condensed matter physics [177], as well as chemical and biological reactions [178]. We discuss this environment-induced decoherence in the context of dissipative diamagnetism. Landau diamagnetism has its origin in coherent circular motion of the electron in a plane normal to the magnetic field. This coherent motion is disturbed due to interaction with the environmental degrees of freedom, e.g. defects, phonons, etc. We illustrate how the system transits from the coherent 'Landau regime' to the decoherent 'Bohr-Van Leeuwen regime' [135]. Egger et al [179] have discussed the environment induced destruction of quantum coherence for the damped harmonic oscillator and for the dissipative two-state system and have established the dependence of this transition on the initial state of preparation. Here we have extended this study of Egger et al [179] and have shown that the coherent-decoherent transition depends on the particular dynamical quantity (e.g., correlation function, occupation probability, etc.) under consideration for the case of Landau-Drude diamagnetism too.

8.2 Model, Quantum Langevin Equation and Einstein Approach

We start from the same Feynman-Vernon Hamiltonian (cf. Eq. (7.1)) for a charged particle in a magnetic field $\vec{B}$, coupled to an environment of quantum harmonic oscillators [154]. As discussed earlier, the contribution of the boundary electrons, are included through a confining harmonic trap, described by the first term on the right hand side of Eq. (7.1), the effect of which can be removed at the end of the calculation by setting $\omega_0 = 0$. Now following Ford et al [172, 173] one can write the QLE emanating from Eq. (7.1) as

$$m\ddot{\vec{x}} + \int_{-\infty}^{t} dt' \gamma(t-t')\dot{\vec{x}}(t') + m\omega_0^2 \vec{x} - \frac{e}{c}(\dot{\vec{x}} \times \vec{B}) = \vec{F}(t), \tag{8.1}$$

where the auto-correlation and the commutator of $\vec{F}(t)$ are given by

$$\Big\langle \{F_\alpha(t), F_\beta(t')\} \Big\rangle = \delta_{\alpha\beta} \frac{2}{\pi} \int_0^\infty \Re[\tilde{\gamma}(\omega + i0^+)] \hbar\omega \coth(\frac{\hbar\omega}{2k_B T}) \cos\{\omega(t-t')\} d\omega, \tag{8.2}$$

$$\Big\langle [F_\alpha(t), F_\beta(t')] \Big\rangle = \delta_{\alpha\beta} \frac{2}{i\pi} \int_0^\infty \Re[\tilde{\gamma}(\omega + i0^+)] \hbar\omega \sin\{\omega(t-t')\} d\omega, \tag{8.3}$$

where $\tilde{\gamma}(s) = \int_0^\infty dt \exp(ist)\gamma(t)$ $(Im\ s > 0)$.

At this stage we introduce the nomenclature of ohmic dissipation as well as non-ohmic dissipation. Defining the spectral density of the environmental degrees of freedom as $J(\omega) = \frac{\pi}{2} \sum_{j=1}^N m_j \omega_j^3 \delta(\omega - \omega_j)$, we can rewrite the memory kernel $\gamma(t)$ in terms of the spectral density as

$$\gamma(t) = \Theta(t) \frac{2}{m\pi} \int_0^\infty d\omega \frac{J(\omega)}{\omega} \cos(\omega t), \tag{8.4}$$

where $\Theta(t)$ is the Heaviside step function. As motivated in the previous chapter, we often deal with physical situations which can be described by such a Caldeira-Leggett model, as given in Eq. (7.1), consisting of only one or a few relevant dynamical variables in contact with a huge environment which is assumed to be a collection of harmonic oscillators [170, 180, 181]. In the ohmic case, damping is frequency-independent and the spectral density $J(\omega) = m\gamma\omega$. The memory kernel $\gamma(t-t')$ is thus replaced by $m\gamma\delta(t-t')$, so that $\Re[\tilde{\gamma}(\omega + i0^+)]$ reduces to $m\gamma$, a constant. In this limit we get an ordinary Langevin equation. It is interesting to note that the underlying stochastic process is still non-Markovian, even though there is no memory. On the other hand, the non-ohmic case can be realized when the bath consists of phonons, as appropriate for instance, in the tunneling of an atom in the bulk [170]. Recently Louis and Sethna [182] have shown that the case of tunneling between surfaces corresponds to "ohmic" dissipation in contrast to the bulk case, where the dissipation is of the "super-ohmic" variety. In the non-ohmic case, for a bath comprising aquastic phonons the spectral density is defined as $J(\omega) = m\tilde{\gamma}(\omega)$, where $\tilde{\gamma}(\omega) = \gamma\omega^3$ [177]. The damping kernel $\tilde{\gamma}(\omega)$ then brings in memory-friction effects.

8.3 Generalized Susceptibility Tensor

In this section we consider the linear response of the position coordinate to an external force $\vec{f}(t)$, assumed small. By imagining the force to have been switched on at time $t = -\infty$ all transient effects can be ignored and the nontransient response can be captured

by the frequency-dependent generalised susceptibility. The corresponding QLE now reads

$$m\ddot{\vec{x}} + \int_{-\infty}^{t} dt' \gamma(t-t')\dot{\vec{x}}(t') + m\omega_0^2 \vec{x} - \frac{e}{c}(\dot{\vec{x}} \times \vec{B}) = \vec{F}(t) + \vec{f}(t). \tag{8.5}$$

Introducing

$$\tilde{Z}_i(\omega) = \int_0^{\infty} dt e^{i\omega t} Z_i(t) \qquad (i = 1, 2, 3, 4; Z_1 = \gamma, Z_2 = q_\beta, Z_3 = F_\alpha, Z_4 = f_\alpha), \tag{8.6}$$

where $\epsilon_{\alpha\beta\rho}$ is the Levi-Civita symbol, and α, β, ρ are the three spatial directions (i.e. $\alpha, \beta, \rho =$ x, y, z), we can rewrite Eq. (8.5) in a Fourier transformed form :

$$\Big[(m(\omega_0^2 - \omega^2) - i\omega\tilde{\gamma}(\omega))\delta_{\alpha\beta} + i\omega\frac{e}{c}\epsilon_{\alpha\beta\rho}B_\rho\Big]\tilde{x}_\beta(\omega) = \tilde{F}_\alpha(\omega) + \tilde{f}_\alpha(\omega). \tag{8.7}$$

Equation (8.7) can be recast as the inverse of Eq. (8.5) in the Fourier space:

$$Y_{\alpha\beta}(\omega)\tilde{x}_\beta(\omega) = [\tilde{F}_\alpha(\omega) + \tilde{f}_\alpha(\omega)], \tag{8.8}$$

with

$$Y(\omega) = \begin{pmatrix} \Delta(\omega) & i\omega\frac{e}{c}B_z & -i\omega\frac{e}{c}B_y \\ -i\omega\frac{e}{c}B_z & \Delta(\omega) & i\omega\frac{e}{c}B_x \\ i\omega\frac{e}{c}B_y & -i\omega\frac{e}{c}B_x & \Delta(\omega) \end{pmatrix}, \tag{8.9}$$

where $\Delta(\omega) = m(\omega_0^2 - \omega^2) - i\omega\tilde{\gamma}(\omega)$. From linear response theory one can write [13]

$$x_\alpha(t) = \int_{-\infty}^{t} ds \chi_{\alpha\beta}(t-s)(F_\beta(s) + f_\beta(s)), \tag{8.10}$$

where $\chi_{\alpha\beta}$ is the generalised susceptibility tensor. In Fourier transformed form Eq. (8.10) becomes

$$\tilde{x}_\alpha(\omega) = \chi_{\alpha\beta}(\omega)[\tilde{F}_\beta(\omega) + \tilde{f}_\beta(\omega)]. \tag{8.11}$$

Comparing Eq. (8.11) with Eq. (8.8) the generalised susceptibility can be evaluated from the following equation :

$$\chi_{\alpha\beta} = [Y^{-1}(\omega)]_{\alpha\beta}, \tag{8.12}$$

Clearly

$$\chi(\omega) = \frac{1}{\det[Y(\omega)]} \begin{pmatrix} \chi_{xx} & \chi_{xy} & \chi_{xz} \\ \chi_{yx} & \chi_{yy} & \chi_{yz} \\ \chi_{zx} & \chi_{zy} & \chi_{zz} \end{pmatrix}, \tag{8.13}$$

where

$$\begin{aligned}
\det[Y(\omega)] &= \Delta(\omega)[\Delta^2(\omega) - (\omega\frac{e}{c})^2\vec{B}^2]; \\
\chi_{ii} &= \Delta^2(\omega) - (\omega\frac{e}{c})^2 B_i^2, (i = x, y, z); \\
\chi_{xy} &= \chi_{yx}^* = -(\omega\frac{e}{c})^2 B_x B_y - i\omega\frac{e}{c}B_z\Delta(\omega); \\
\chi_{xz} &= \chi_{zx}^* = -(\omega\frac{e}{c})^2 B_x B_z + i\omega\frac{e}{c}B_y\Delta(\omega); \\
\chi_{yz} &= \chi_{zy}^* = -(\omega\frac{e}{c})^2 B_y B_z - i\omega\frac{e}{c}B_\alpha\Delta(\omega),
\end{aligned} \tag{8.14}$$

where $(*)$ denotes the complex conjugate of the corresponding variable. The expression is simplified when the magnetic field is taken along z axis, thus

$$\chi(\omega) = \frac{1}{\det[Y(\omega)]}\begin{pmatrix} \Delta^2(\omega) & -i\omega\frac{e}{c}\Delta(\omega)B & 0 \\ i\omega\frac{e}{c}\Delta(\omega)B & \Delta^2(\omega) & 0 \\ 0 & 0 & \Delta^2(\omega) - (\omega\frac{e}{c})^2B^2 \end{pmatrix}. \tag{8.15}$$

For this particular case the real part of the susceptibility is

$$\chi'_{xx} = \chi'_{yy} = \frac{1}{2m^2}\Big[\frac{(\omega_0^2 - \omega^2 + \omega\omega_c/2)}{(\omega^2 - \omega_0^2 + \omega\omega_c)^2 + \frac{\omega^2\tilde{\gamma}^2(\omega)}{m^2}} + \frac{(\omega_0^2 - \omega^2 - \omega\omega_c/2)}{(\omega^2 - \omega_0^2 - \omega\omega_c)^2 + \frac{\omega^2\tilde{\gamma}^2(\omega)}{m^2}}\Big], \tag{8.16}$$

and the imaginary part is

$$\chi''_{xx} = \chi''_{yy} = \frac{\tilde{\gamma}(\omega)\omega}{2m^2}\Big[\frac{1}{(\omega^2 - \omega_0^2 + \omega\omega_c)^2 + \frac{\omega^2\tilde{\gamma}^2(\omega)}{m^2}} + \frac{1}{(\omega^2 - \omega_0^2 - \omega\omega_c)^2 + \frac{\omega^2\tilde{\gamma}^2(\omega)}{m^2}}\Big], \tag{8.17}$$

where the cyclotron frequency $\omega_c = \frac{eB}{mc}$. For the ohmic dissipation case the susceptibility has four poles at

$$\begin{aligned}
\omega = \pm\tilde{\omega}_+ &= \Big[\frac{\omega_c + i\gamma}{2} \pm \frac{\sqrt{4\omega_0^2 + \omega_c^2 - \gamma^2 + 2i\omega_c\gamma}}{2}\Big] \\
\omega = \pm\tilde{\omega}_- &= \Big[\frac{-\omega_c + i\gamma}{2} \pm \frac{\sqrt{4\omega_0^2 + \omega_c^2 - \gamma^2 - 2i\omega_c\gamma}}{2}\Big].
\end{aligned} \tag{8.18}$$

On the other hand, for the non-ohmic case these poles cannot be evaluated analytically. The numerical results for the ohmic dissipation as well as non-ohmic dissipation cases are presented below.

We plot in Fig. (8.1) the dissipative part of the x-component of susceptibility i.e. $\chi''_{xx}(\omega)$

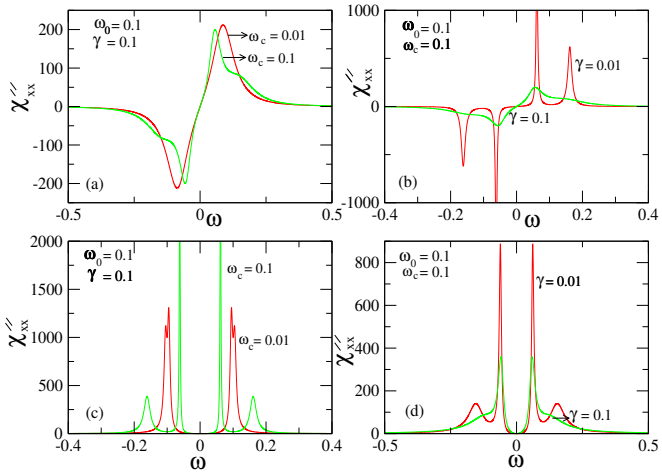

Figure 8.1: The imaginary part of susceptibility χ_{xx} (a) ohmic dissipation case ($J(\omega) \sim \omega$) for two ω_c values. (b) ohmic dissipation case for two γ values. (c) Non-ohmic dissipation case ($J(\omega) \sim \omega^3$) for two ω_c values. (d) Non-ohmic dissipation case for two γ values.

versus ω for different values of ω_c and γ in accordance with Eq. (8.16). We note that $\chi''_{xx}(\omega)$ is odd in ω for the ohmic dissipation case and has Lorentzian line shapes for finite damping values, with peaks centered at the poles. For the non-ohmic case $\chi''_{xx}(\omega)$ is even in ω. It is evident from Fig. (8.1-b) that for finite but weak damping one can obtain all the four peaks for the ohmic dissipation case whereas for high damping only two peaks are obtained. The same is true for the non-ohmic case (Fig. (8.1-d)). The only difference is that the magnitude of the peak height is higher for the non-ohmic case and is always positive. Also the peak width increases with the increase of γ for both ohmic and non-ohmic cases. On the other hand the width of the peak decreases with the increase of ω_c, as is expected on physical grounds. In the non-ohmic case the number of peaks also increases from two to four with the increase of ω_c, whereas it remains two for the ohmic case with the increase of ω_c, if γ is kept large. Thus, dissipative effects are stronger for the ohmic case.

In Fig. (8.2) we plot the reactive or the real part of the x-component of susceptibility ($\chi'_{xx}(\omega)$) versus ω for different values of ω_c and γ in accordance with Eq. (8.16). $\chi'_{xx}(\omega)$

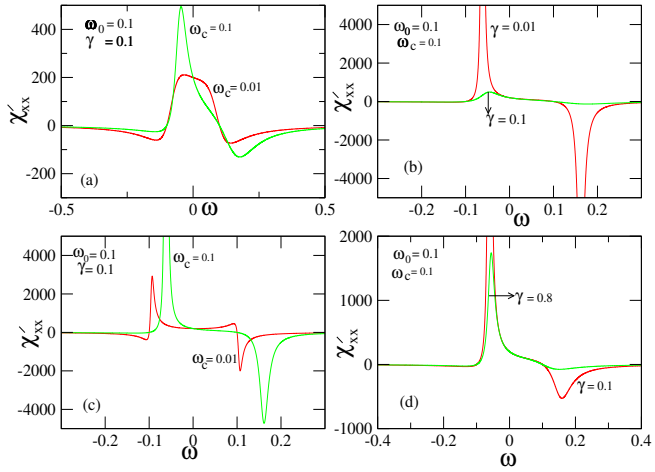

Figure 8.2: The real part of susceptibility χ_{xx} (a) ohmic dissipation case ($J(\omega) \sim \omega$) for two ω_c values. (b) ohmic dissipation case for two γ values. (c) Non-ohmic dissipation case ($J(\omega) \sim \omega^3$) for two ω_c values. (d) Non-ohmic dissipation case for two γ values.

is odd in ω for the ohmic as well as non-ohmic cases. The spreading of the peaks increases but the peak height decreases with the decrease of ω_c for the ohmic case. On the other hand both the spreading and peak height decrease with the decrease of ω_c for the non-ohmic case. But the features are the same with the variation of γ for both ohmic and non-ohmic cases —- the peak height increases but the spreading decreases with the decrease of γ. In addition the number of peaks increases from one to two with the decrease of γ in the ohmic as well as non-ohmic cases.

The z component of the susceptibility tensor is of course the same as that of a damped harmonic oscillator because it has no relation to the cyclotron frequenc ω_c.

8.4 Fluctuation - Dissipation Relationship & Equivalence of Einstein and Gibbs Approaches.

In section 8.3 we calculated the susceptibility as the asymptotic (i.e. $t \to \infty$) response from a fully time-dependent formulation of the underlying QLE. Because detailed balance

relations (viz. Eqs. (8.2) and (8.3)) are built-in within the QLE, as the heat bath is assumed to be in thermal equilibrium at a fixed temperature T, the asymptotic response is expected to be related to the equilibrium properties of the system. This expectation is at the heart of what Kadanoff calls the Einstein approach to Statistical Mechanics [145] in which equilibrium answers are sought to be obtained from the asymptotic limit of time-dependent results. It is then natural to ask whether the response obtained from the Einstein approach can be related to spontaneous or equilibrium fluctuations that can be independently calculated from the standard Gibbsian formulation of equilibrium Statistical Mechanics (derived in the chapter 7). If we can establish this relation it will not only be tantamount to establishing the fluctuation-dissipation theorem for the phenomenon at hand, but also to demonstrating the equivalence of the Einstein and the Gibbs approaches to Statistical Mechanics [92].

Now combining Eq. (8.17) with the Fourier transformed form of equilibrium position autocorrelation function i.e. Eq.(7.34) one can easily show that

$$\tilde{C}(\omega) = \frac{2\hbar}{1 - \exp(-\beta\hbar\omega)}\chi''_{xx}(\omega). \tag{8.19}$$

The equation (8.19) represents the fluctuation-dissipation theorem in the context of dissipative Landau diamagnetism. The position autocorrelation function describes the spontaneous fluctuations of the system while the imaginary part of the dynamic susceptibility χ''_{xx} determines the energy dissipation in the system due to work done by an external weak force.

We use some of the results derived in the previous chapter (*a la* Gibbs) in this chapter to show that dissipative diamagnetism provides an elegantly pedagogical toy model within which equilibrium and non-equilibrium statistical mechanics can be holistically combined. The Eq.(7.26) of the previous chapter yields the asymptotic result of Dattagupta and Singh[140], for $\nu_0 = 0$ (cf. Eq. (19) of Dattagupta and Singh [140]). We demonstrate this below, for ohmic dissipation, since only the latter case was considered in Dattagupta and Singh [140]. In the so-called ohmic dissipation model [143]

$$J(\omega) = M\gamma\omega. \tag{8.20}$$

Now Eq.(19) of Dattagupta and Singh [140], based on the Einstein approach of dissipative diamagnetism, can be recast as follows:

$$\begin{aligned}\mathcal{M}_z &= \frac{|e|\hbar}{2Mc}\Big\{\sum_{n=1}^{\infty}\frac{4n\pi\zeta\nu_c}{\left(\nu_c^2+\zeta^2-n^2\pi^2\right)^2+4n^2\pi^2\nu_c^2} \\ &\quad +\Re\Big[\frac{1}{(\nu_c-i\zeta)}-\coth(\nu_c-i\zeta)\Big]\Big\}.\end{aligned} \tag{8.21}$$

Note that the term inside the square parentheses is just the Landau contribution with however a *complex* cyclotron frequency with damping ζ as the imaginary component. Over and above this is the further contribution, solely dependent on damping, given by the first term (involving a summation over n) within the curly brackets. Using the identity

$$\coth(z)=\frac{1}{z}+\sum_{n=1}^{\infty}\frac{2z}{(z^2+n^2\pi^2)}, \tag{8.22}$$

one can rewrite Eq.(8.21) as follows:

$$\begin{aligned}\mathcal{M}_z &= \frac{|e|\hbar}{2Mc}\Big\{\sum_{n=1}^{\infty}\frac{4n\pi\zeta\nu_c}{\left(\nu_c^2+\zeta^2-n^2\pi^2\right)^2+4n^2\pi^2\nu_c^2} \\ &\quad -\Re\sum_{n=1}^{\infty}\frac{2(\nu_c-i\zeta)}{\left(\nu_c-i\zeta\right)^2+n^2\pi^2}\Big\}.\end{aligned} \tag{8.23}$$

After some algebra one can express $\mathcal{M}_z$ as

$$\mathcal{M}_z=-\frac{|e|\hbar}{Mc}\nu_c\sum_{n=1}^{\infty}\frac{1}{\nu_c^2+\left(\zeta+n\pi\right)^2}\ , \tag{8.24}$$

which equals Eq.(7.24) in the limit $\nu_0\to 0$.

Thus we are able to establish the equivalence of the Einstein approach to statistical mechanics in which the equilibrium answers are sought to be obtained from the asymptotic limit of time-dependent results and the conventional equilibrium Gibbsian ensemble approach for the phenomena of Landau dissipative diamagnetism. In establishing fluctuation-dissipation relationship, we derive the imaginary part of the dynamical susceptibility from the QLE like Eq. 8.1 (*a la* Einstein) and then connect it with that of the equilibrium position autocorrelation function (*a la* Gibbs). In the second case, we recast Eq. (19) of Dattagupta and Singh [140] in such a form that it matches with the equilibrium answer of Landau dissipative diamagnetism (Eq. 7.24) derived in the previous chapter on the basis of equilibrium Gibbsian ensemble approach.

8.5 Coherence - Decoherence Transition

In this section our discussion is focused on the destruction of quantum coherence by environment-induced dissipation in the context of Landau diamagnetism. Two questions are relevant: (i) Can we quantify the criterion for crossover from coherent to decoherent dynamics ? (ii) Is this criterion universal ? As far as some model systems are concerned, the answer to (i) is in the affirmative [179, 168]. Regarding the question (ii), there seems to be no universality in the criterion of crossover. As a matter of fact, the value of the crossover parameter depends on the particular quantity under consideration and its initial preparation. Thus, quantum memory effects play a crucial role as the system makes a transition from the coherent to the decoherent regime. To clarify this issue we focus on dissipative diamagnetism and consider its $T = 0$ behavior, wherein quantum coherence is the most prominent. Here we follow the discussion of Egger et al [179].

We start with the QLE for dissipative Landau diamagnetism subject to Ohmic damping. The motion in the x-y plane can be expressed in the compact form:

$$\ddot{Z} + \bar{\gamma}\dot{Z} + \omega_0^2 Z = \frac{\theta(t)}{m}, \tag{8.25}$$

where $Z = x + iy$, $\bar{\gamma} = \gamma + i\omega_c$, and $\theta = F_x + iF_y$. Thus, the time-dependence of the corresponding classical quantity (*a la* Ehrenfest) is governed by the following equation:

$$\langle\ddot{Z}\rangle + \bar{\gamma}\langle\dot{Z}\rangle + \omega_0^2\langle Z\rangle = \frac{\theta(t)}{m}, \tag{8.26}$$

where the angular brackets represent statistical averages over the ground state properties ($T = 0$), i.e. the expectation values. As discussed earlier the response to an external force is characterized by the generalised susceptibility $\chi_{osc}(t)$ [13]:

$$\langle Z(t)\rangle = \frac{1}{m\omega_0}\int_{-\infty}^{t} dt'\chi_{osc}(t-t')\theta(t'). \tag{8.27}$$

From Eqs. (8.26) and (8.27), we obtain the Fourier transform of $\chi_{osc}(t)$ as

$$\chi_{osc}(\omega) = \frac{\omega_0}{\omega_0^2 - \omega^2 - i\bar{\gamma}\omega}. \tag{8.28}$$

On the other hand, using the fluctuation-dissipation theorem [13], $\chi_{osc}(\omega)$ can be related to the spectral function $S_{osc}(\omega)$, which in turn determines the equilibrium correlation

function $C_{osc}(\omega)$. The functional relationship which holds at $T = 0$ is as follows:

$$\Im\chi_{osc}(\omega) = \omega S_{osc}(\omega) = \frac{\omega}{|\omega|} C_{osc}(\omega), \tag{8.29}$$

where $C_{osc}(t) = \Re\langle Z(t)Z(0)\rangle$. Using Eqs. (8.28) and (8.29), we obtain the spectral function

$$S_{osc}(\omega) = \frac{\gamma\omega_0}{(\omega_0^2 - \omega^2 + \omega\omega_c)^2 + \gamma^2\omega^2}. \tag{8.30}$$

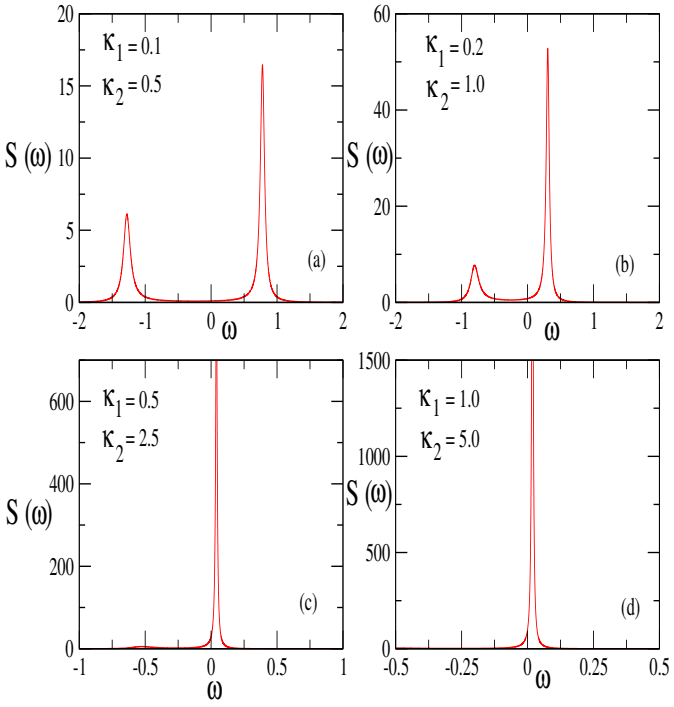

Figure 8.3: Spectral function $S_{osc}(\omega)$ vs. ω with Ohmic dissipation for dissipative Landau diamagnetism for different parameter values.

The quantity $S_{osc}(\omega)$ can be used as a signature for the transition from coherence to decoherence: $S_{osc}(\omega)$ has two inelastic peaks at $\omega_m = \frac{\omega_0}{2}\Big[-\kappa_2 \pm \sqrt{4 - \kappa_1^2 + \kappa_2^2}\Big]$ for weak

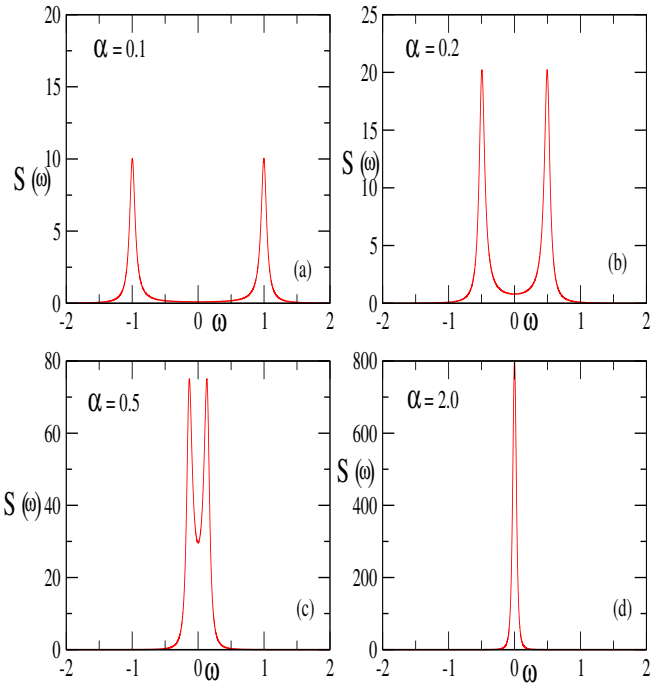

Figure 8.4: Spectral function $S_{osc}(\omega)$ vs. ω with Ohmic dissipation for a damped harmonic oscillator for different parameter values.

damping, where κ_1 and κ_2 are dimensionless parameters defined by $\kappa_1 = \frac{\gamma}{\omega_0}$ and $\kappa_2 = \frac{\omega_c}{\omega_0}$. These two quantities are employed as the crossover parameters to quantify the coherence to decoherence transition. Defining $\bar{\kappa}^2 = \kappa_1^2 + \kappa_2^2$, we can say that below the critical coherent criterium (defined below, c.f. Eq. (8.33)) i.e. $\bar{\kappa}^2 < \bar{\kappa}_c^2$, the function $S_{osc}(\omega)$ exhibits two inelastic peaks which are evident from Fig. (8.4) in which we plot $S_{osc}(\omega)$ vs. ω for different κ_1 and κ_2. At the critical coherent criterium (c.f. Eq. (8.33)) the two peaks merge into a single quasielastic peak. The latter persists for $\bar{\kappa}^2 > \bar{\kappa}_c^2$. Since the quasielastic peak is centered near $\omega \simeq 0$, we can make a small-ω expansion of $S_{osc}(\omega)$:

$$S_{osc}(\omega) \simeq \kappa_1 \chi_0^2 \Big[1 - \kappa_2 \chi_0 \omega + (2 - \kappa_1^2 - \kappa_2^2)\chi_0^2 \omega^2 + O(\omega^3)\Big], \tag{8.31}$$

where $\chi_0 = \frac{1}{\omega_0}$. The critical line is determined by inspecting the sign of the curvature of $S_{osc}(\omega)$. The latter is positive (implying coherence) if $\frac{d^2 S_{osc}(\omega)}{d\omega^2} > 0$, or

$$\bar{\kappa}^2 = \kappa_1^2 + \kappa_2^2 < 2. \tag{8.32}$$

But the curvature changes sign at the critical line:

$$\bar{\kappa}_c^2 = \kappa_1^2 + \kappa_2^2 = 2, \tag{8.33}$$

and hence the system goes to the decoherent region when

$$\bar{\kappa}^2 = \kappa_1^2 + \kappa_2^2 > 2. \tag{8.34}$$

It is illustrative to compare this behaviour with that of the damped harmonic oscillator which was discussed by Egger et al [179]. From Figs. (8.4) and (8.5) one notes that for the damped oscillator case $S_{osc}(\omega)$ has two inelastic peaks of equal height for weak damping. As the one-parameter damping strength increases these two peaks approach each other and at the critical damping strength (α_c) the two peaks merge into a single quasielastic peak at $\omega = 0$ which persists for $\alpha > \alpha_c$. On the other hand, for dissipative diamagnetism, the coherent-decoherent transition is to be examined in a two-parameter plane, defined by κ_1 and κ_2. One obtains two inelastic peaks which are not of equal height for low values of κ_1 and κ_2 because the peaks are not symmetric on either side of $\omega = 0$. As one increases κ_1 and κ_2 the peak height of the small peak decreases and eventually vanishes at the critical line to yield a single peak which is not at $\omega = 0$, but near $\omega = 0$. Above the critical line the single quasielastic peak persists.

We turn next to a different criterion for quantifying the transition from coherence to decoherence, which is based on the quantity $P_{osc}(t)$, defined as follows:

$$P_{osc}(t) = \frac{\langle Z(t) \rangle}{Z_0}. \tag{8.35}$$

We are interested in the relaxation of the expectation value $\langle Z(t) \rangle$ starting from a non-equilibrium initial state. Applying the force $F(t) = m\omega_0^2 Z_0$ for $t < 0$, the initial condition $\langle Z(0) \rangle = Z_0$ is prepared and the corresponding dynamical quantity $P_{osc}(t)$ is computed, after switching off the force $F(t)$, at $t = 0$. Following the damped quantum harmonic

oscillator case [179] we may now write

$$P_{osc}(t) = \Re\Big[\frac{\cos(\bar{\Omega}t - \bar{\phi})\exp(-\frac{\bar{\gamma}t}{2})}{\cos(\bar{\phi})}\Big], \tag{8.36}$$

where

$$\begin{aligned} \bar{\Omega} &= \sqrt{\omega_0^2 - \frac{\bar{\gamma}^2}{4}} = \Omega' + i\Omega'' \\ \bar{\phi} &= \Re[\tan^{-1}(\frac{\bar{\gamma}}{2\bar{\Omega}}]. \end{aligned} \tag{8.37}$$

Defining $a = (\omega_0^2 + \frac{\omega_c^2}{4} - \frac{\gamma^2}{4})$ and $b = \frac{\gamma\omega_c}{2}$,

$$\begin{aligned} \Omega' &= \frac{1}{\sqrt{2}}\sqrt{a + \sqrt{a^2 + b^2}}, \\ \Omega'' &= \frac{1}{\sqrt{2}}\sqrt{\sqrt{a^2 + b^2} - a}, \\ \bar{\phi} &= \tan^{-1}(X), \\ X &= \frac{\gamma\Omega' + \Omega''\omega_c}{2(\Omega'^2 + \Omega''\omega_c)}, \end{aligned} \tag{8.38}$$

we find

$$P_{osc}(t) = \Big[\frac{\cos(\Omega' t - \bar{\phi})\cos(\Omega'' t)\cos(\frac{\omega_c t}{2}) - \sin(\Omega' t - \bar{\phi})\sin(\Omega'' t)\sin(\frac{\omega_c t}{2})}{\cos(\bar{\phi})}\Big]\exp(-\frac{\gamma t}{2}). \tag{8.39}$$

The signature of coherence is now damped-oscillatory behavior if $b^2 > 0$ and $a^2 + b^2 > 0$. Thus the important inequality condition for the system to be coherent is:

$$(1 - \kappa_1^2 + \kappa_2^2)^2 + \frac{(\kappa_1\kappa_2)^2}{4} > 0. \tag{8.40}$$

The system crosses over to relaxational (decoherent) behavior at the critical line

$$(1 - \frac{\kappa_1^2}{4} + \frac{\kappa_2^2}{4})^2 + \frac{(\kappa_1\kappa_2)^2}{4} = 0, \tag{8.41}$$

which is clearly different from the criterium mentioned above (cf. Eq. (8.33)). Thus the criterion for crossover from coherence to decoherence depends on the specific physical quantity considered. This conclusion is similar to the cases of damped quantum harmonic oscillator as well as the spin-Boson model [179].

8.6 Summary and Conclusions

We have analyzed here an exact treatment of the Feynman-Vernon model of a charged Brownian particle in a magnetic field in the quantum dissipative regime. Starting from the QLE we have derived the generalised susceptibility tensor, and have discussed its real and imaginary parts for the particular case when the magnetic field $\vec{B}$ is along the z axis. In the chapter 7, we have calculated the position autocorrelation function that measures the spontaneous fluctuations of the system degrees of freedom due to coupling with the environment by following the Gibbsian ensemble approach. The latter has been shown to be related to the imaginary part of the susceptibility that measures the energy dissipation of the system due to irreversible energy transfer between the system and the environment. The aforesaid treatment then exemplifies the fluctuation-dissipation theorem in the context of dissipative diamagnetism as well as establishes the equivalence of the Einstein and the Gibbs approaches to Statistical Mechanics, for the case at hand. Environment-induced decoherence is an important issue in mesoscopic systems and quantum information processes. We have discussed this in the context of dissipative diamagnetism and have argued that the transition from the Landau to the Bohr-Van Leeuwen regime can indeed be viewed as a coherence to decoherence transition. Further it has been demonstrated that the initial preparation of a dissipative quantum system leads to abrupt changes regarding the criterion for coherent to decoherent transition. As in glassy systems characterized by hysteretic behavior, quantum systems also exhibit memory of their initial state of preparation.

In conclusion, we have presented a unified treatment of threefold response, i.e. fluctuation, dissipation and decoherence of a system due to its coupling with environment in the context of the contemporarily important topic of dissipative diamagnetism. We have established the equivalence of the equilibrium and non-equilibrium statistical physics for a phenomenon like Landau-Drude diamagnetism, which is inherently quantum and strongly dependent on boundary effects. Finally, we have demonstrated that the coherent to incoherent transition depends to a large degree on the particular dynamical quantity under consideration (e.g. correlation function, occupation probability etc.), as well as initial conditions of preparation. Our derived results should be of some interest in the presently active area of mesoscopic structures.

Chapter 9

Summary

In this concluding chapter we summarize briefly the contents of this thesis. The thesis is primarily based on the concepts of "Brownian motion". We have discussed both the classical as well as quantum Brownian motion. In most cases we are motivated by some experimental measurements. So there is a close connection between our theoretical study and the experimental measurements of ours as well as other groups.

We begin our discussion from the classical rotational "Brownian" motion of nanomagnetic particles. The single domain nanoparticle undergoes a rotational Brownian movement surmounting an anisotropic potential barrier. In Chapter 2 we have demonstrated the equilibrium magnetic and caloric properties of a collection of non-interacting single domain particles. In this context we have analyzed the differences between the progressive freezing of supermoments and spinglass phase transition. The divergence of nonlinear susceptibilities in the two cases helps us in discriminating these two processes. This work is motivated by the experimental observation of Bitoh et al [33].

In Chapter 3 we turned to different non-equilibrium phenomena observed in single domain nanoparticles. We have discussed the memory effect observed in nanomagnetic particles in the field-cool (FC) magnetization measurements under a certain heating and cooling protocol. We are motivated in this work by the experimental observation of Sun et al [20]. We further discuss the relaxation theory of the single domain nanoparticles. In this context we introduce the effect of dipole-dipole interaction on the relaxation rate. It has been observed that one can obtain a plethora of relaxation rates by varying the sizes of the particles even a tiny bit. Thus one can observe polydispersity induced slow dynamics in the non-interacting "supermoments". We have demonstrated the polydispersity induced

"memory effect" by considering a bimodal distribution in volume. In the next chapter we have discussed the memory effect observed in the field cool (FC) and zero field cool (ZFC) relaxation measurements under different field and temperature protocols. We have also differentiated between the two types of slow dynamics observed in the non-interacting and interacting single domain nanoparticles. One can easily observe a flat FC magnetization curve for the interacting system whereas one can observe an increasing FC magnetization curve for the non-interacting system. In the non-interacting case one can not find any memory in the double memory experiment in the ZFC protocol. On the other hand one can easily observe a dip in the double memory experiment in the ZFC method for the interacting system.

In Chapter 5 we have discussed the variation of coercivity with the particle size. We have introduced a stochastic model and have explained the experimental observation of Luna et al [78]. We had to consider two regimes - the single domain regime demonstrates the increasing part of the coercivity versus particle size curve. On the other hand the decreasing part of the curve is explained by assuming a multidomain regime and with the help of supersymmetry Quantum mechanics (SUSY QM).

In Chapter 6 we consider the translational Brownian motion of an underdamped particle in the presence of a space periodic potential and a high frequency space dependent time periodic force. We observe the long time behaviour of such an underdamped Brownian particle. In the Kapitza time window in which the observation time is much longer than any relevant time scales of the system, one can obtain a time-independent effective potential in which the underdamped Brownian particle moves. One can then observe "Stochastic Resonance", i.e., the enhancement of the diffusion coefficient in the presence of an external time periodic force, space-periodic potential and thermal noise. So we observe that the optimal mixing of space periodic force, time periodic external high frequency field and thermal noise is much more effective than the usual diffusion mechanism. We acronym this enhancement of diffusion as "stochastic resonance" (SR).

In the last two chapters of this thesis we turn from classical to quantum Brownian motion of a charged particle in the presence of an external magnetic field, is interacting with the environment, which is modeled as a collection of harmonic oscillators. In Chapter 7 we have discussed the dissipative diamagnetism which is inherently a quantum phe-

nomenon. We are motivated in this work by the discussion of L. P. Kadanoff on different approaches of statistical mechanics in his book [145]. In this book Kadanoff analyses about Einstein's approach in which one can derive the equilibrium answers from the non-equilibrium Langevin equations by taking the asymptotic limit ($t \to \infty$). We have shown the equivalence of the Einstein approach and the usual Gibbsian ensemble approach in the context of dissipative diamagnetism. We have shown that at large dissipation, the dissipative diamagnetism vanishes and it goes to the classical regime. In this context we have discussed the effect of boundary electrons which is essential in the study of mesoscopic structure. In addition, we have demonstrated that the appearance of dissipative parameter (γ) in the equilibrium answer is completely a quantum phenomenon.

In Chapter 8 we consider the effect of environmental coupling of the system which consists of a charged particle moving in a constant magnetic field. We have discussed the three-fold response i.e. fluctuation, dissipation and decoherence in the context of dissipative diamagnetism. Starting from a 'non-equilibrium' quantum Langevin equation (QLE), we calculate the generalized susceptibility tensor. We connect the imaginary part of this susceptibility tensor with that of the position autocorrelation function calculated from the equilibrium Gibbsian ensemble approach. Thus it not only establishes a relationship between the position autocorrelation function and the imaginary part of the susceptibility —- a statement of the fluctuation-dissipation theorem, but also unifies equilibrium Gibbsian ensemble approach and the Einstein approach in the context of Landau-Drude diamagnetism. We also provide a treatment of the environment induced coherence to decoherence transition in the context of Landau-Drude diamagnetism. In this context we have demonstrated elaborately that the initial state of preparation of a dissipative quantum systems leads to abrupt changes regarding the criterion for coherent- to - decoherent transition. Thus quantum dissipative systems exhibit memory of their initial state of preparation.

Bibliography

[1] E. Nelson, *Dynamical Theories of Brownian Motion*, (Princeton University Press, Princeton, 1967).

[2] W. T. Coffey, Yu. P. Kalmykov and J. T. Waldron, *The Langevin Equation*, (World Scientific, Singapore, 1996).

[3] A. Einstein, in R. H. Fürth Ed., *Investigations on the Theory of the Brownian Movement*, (Methuen, London, 1926).

[4] S. Chandrasekhar, *Stochastic Problems in Physics and Astronomy*, Rev. Mod. Phys. *15*, 1 (1943).

[5] A. T. Fuller, *Nonlinear Stochastic Control Systems*, (Taylor and Francis, London, 1970).

[6] R. H. Fowler, *Statistical mechanics*, (Oxford University Press, Oxford, 1938); N. G. van Kampen, *Stochastic Processes in Physics and Chemistry*, (North-Holland Physics Publishing, Amsterdam, 1981).

[7] K. S. Miller, *Complex Stochastic Processes*, (Addison Wesley, Reading, Mass. 1974).

[8] M. C. Wang and G. E. Uhlenbeck, *On the Theory of the Brownian Motion II*, Rev. Mod. Phys., *17*, 323 (1945).

[9] P. Langevin, *Comptes Rendus*, *146*, 530 (1908).

[10] P. Debye, *Polar Molecules*, (Chemical Catalog Co. New York, 1929).

[11] J. R. McConnell, *Rotational Brownian Motion and Dielectric Theory*, (Academic Press, New York, 1980).

[12] H. Risken, The Fokker-Planck Equation, Methods of Solution and Applications, Corrected reprint of the second edition, Springer, 1992.

[13] S. Dattagupta, *Relaxation Phenomena in Condensed Matter Physics, Chapter XV*, Academic Press, Orlando(1987).

[14] G. W. Ford, J. T. Lewis and R. F. O'Connell, Phys. Rev. A *37*, 4419 (1988).

[15] R. Zwanzig, J. Stat. Phys. *9*, 215 (1973).

[16] R. Zwanzig, *Nonequilibrium Statistical Mechanics* (Oxford University Press, New York 2001).

[17] J. L. Dormann, D. Fiorani, and E. Tronc, Adv. Chem. Phys. *98*, 283 (1997).

[18] V. F. Puntes, K. M. Krishnan, and A. P. Alivisatos, Science *291*, 2115 (2001).

[19] J. Frankel and J. Dorfman, Nature (London) *126*, 274 (1930); C. Kittel, Phys. Rev. *70*, 965 (1946).

[20] S. Sun, C. B. Murray, D. Weller, L. Folks, and A. Moser, Science *287*, 1989 (2000).

[21] C. P. Bean and J. D. Livingstone, J. Appl. Phys. *30*, 120s (1959); I. S. Jacobs and C. P. Bean, *in magnetism* edited by G. T. Rado and H. Suhl (Academic, New York, 1963), Vol. III.

[22] A. Aharoni, Phys. Rev. A *135*, 447 (1964); Yu. L. Raikher and M. I. Shlimis, Zh. Eksp. Teor. Fiz. *67*, 1060 (1974) [Sov. Phys. JETP *40*, 526 (1975)]; D. Kumar and S. Dattagupta, J. Phys. c *16*, 3779 (1983); W. T. Coffey, D. S. F. Crothers, Yu. P. Kalmykov, E. S. Massawe, and J. T. Waldron, Phys. Rev. E. *49*, 1869 (1994).

[23] Yu. L. Raikher and V. I. Stepanov, Phys. Rev. B *52*, 3493 (1995).

[24] L. Neel, Ann. Geophys. *5*, 99 (1949).

[25] W. F. Brown, Jr., Phys. Rev. *130*, 1677 (1963).

[26] S. F. Edwards and P. W. Anderson, J. Phys. F *5*, 965 (1975).

[27] J. L. Dormann, D. Fiorani, J. L. Tholence and C. Sella, J. Magn. Magn. Mater. *35*, 117 (1983).

[28] D. Fiorani, J. Tholence and J. L. Dormann, J. Phys. C *19* 5495 (1986).

[29] R. W. Chantrell, M. El-Hilo and K. O'Grady, IEEE Trans. Magn. *27*, 3570 (1991).

[30] M. El-Hilo and K. O'Grady, IEEE Trans. Magn. *26*, 1807 (1988).

[31] M. El-Hilo, K. O'Grady, and J. Popplewell, J. Appl. Phys. *69*, 5133 (1991).

[32] J. L. Dormann, J. Bessais and D. Fiorani, J. Phys. C *21*, 2015 (1988).

[33] T. Bitoh, K. Ohba, M. Takamatsu, T. Shirane and S. Chikazawa, J. Phys. Soc. Jpn. *62*, 2583 (1993); T. Bitoh, T. Shirane and S. Chikazawa, J. Phys. Soc. Jpn. *62*, 2837 (1993).

[34] T. Jönsson, J. Mattson, C. Djurberg, F. A. Khan, P. Nordblad, and P. Svedlindh, Phys. Rev. Lett. *75*, 4138 (1995).

[35] J. L. Garcia-Palacios and F. J. Lazaro, Phys. Rev. B *55*, 1006 1997; Phys. Rev. B *58*, 14937 (1998).

[36] Arfken and Weber *Mathematical Methods for Physicists 5th ed.* (Academic, Boston, 1997).

[37] J. W. Shih, Phys. Rev. *38*, 2051 (1931).

[38] V. Cannella and J. A. Mydosh, Phys. Rev. B *6*, 4220 (1974).

[39] O. S. Lutes and J. L. Schmit, Phys. Rev. *134*, A676 (1964).

[40] T. Bitoh, K. Ohba, M. Takamatsu, T. Shirane and S. Chikazawa, J. Magn. Magn. Mater. *154*, 59 (1996).

[41] M. Suzuki, Prog. Theor. Phys. *58*, 1151 (1977).

[42] K. Wada and H. Takayama, Prog. Theor. Phys. *64*, 327 (1980).

[43] D. Sherrington and S. Kirkpatrick, Phys. Rev. Lett. *35*, 1752 (1975).

[44] A.N. Goldstein, *Hand Book of Nanophase Materials* (New York:Marcel Dekker Inc.)(1997).

[45] *Magnetic Properties of Fine Particles*, edited by J. L. Dormann and D. Fiorani (North-Holland, Amsterdam, 1992).

[46] K. M. Unruh and C. L. Chein, *Nanomaterials: Synthesis, Properties and Applications*, eds., A .S. Edelstein and R. C. Cammarata (Bristol: Institute of Physics).

[47] *Physical Principles of Magnetism*, A.H.Morrish, John Wiley,New York,1965.

[48] Steen Mϕrup and Elisabeth Tronc, Phys. Rev. Lett. **72**,3278(1994).

[49] E. P. Wohlfarth, J.Phys.**F10**,L241(1980).

[50] R. Street and J. C. Woolley, Proc. Phys. Soc. London, Sec A **62**, 562 1949. Also reviewed in S. Dattagupta, *Relaxation Phenomena in Condensed Matter Physics, Chapter XV*, Academic Press, Orlando(1987).

[51] Y. Sun, M. B. Salamon, K. Garnier and R. S. Averback, Phys.Rev.Lett.**91**,167206(2003).

[52] M. Sasaki, P. E. Jonsson, H. Takayama and P. Nordblad, Phys. Rev. B *71*, 165314 (2005).

[53] J. D. Wright and J. M. Sommerdijk, *Sol-Gel Materials, Chemistry and Applications* (Taylor and Francis, London, 2001).

[54] J. M. Luttinger and L. Tisza Phys. Rev. **70**, 954 (1946).

[55] See, for instance, A. Abragam, *The Theory of Nuclear Magnetism* (Oxford University Press, London, 1961).

[56] A. P. Young, in *Spin Glasses and Random Fields*, World Scientific, Singapore (1987).

[57] K. H. Fischer and J. A. Hertz,*Spin Glasses*,Cambridge University Press (1991).

[58] See for instance, K. Binder and W. Kinzel in Heidelberg Colloquium on Spin Glasses (J.L.Van Hemmen and I.Morgenstern),eds.,Springer-Verlag,Berlin and New York,p279 and references therein.

[59] J. P. Bouchaud, L. Cugliandolo, J. Kurchan, and M. Mezard, in *Spin Glasses and Random fields* edited by A. P. Young (World Scientific, Singapore, 1998).

[60] M. Mezard, G. Parisi, N. Sourlas, G. Toulouse and M. Virasoro, Phys. Rev. Lett. *52*, 1156 (1984).

[61] Y. Sun, M. B. Salamon, K. Garnier and R. S. Averback, Phys. Rev. Lett. *91*, 167206 (2003); M. Sasaki, P.E. Jönsson, and P. Nordblad, Phys. Rev. Lett. *93*, 139701 (2004); R. K. Zheng, H. Gu, and X. X. Zhang, Phys. Rev. Lett. *93*, 139702 (2004); Y. Sun, M. B. Salomon, K. Garnier, and R. S. Averback, Phys. Rev. Lett. *93*, 139703 (2004).

[62] S. Chakraverty, M. Bandyopadhyay, S. Chatterjee, S. Dattagupta, A. Frydmann, S. Sengupta and P. A. Sreeram, Phys. Rev. B *71*, 054401 (2005).

[63] G. M. Tsoi, L. E. Wenger, U. Senaratne, R. J. Tackett, E. C. Buc, R. Naik, P. P. Vaishnava and V. Naik, Phys. Rev. B *72*, 014445 (2005).

[64] R. K. Zheng, Hongwei Gu, Bing Xu, and X. X. Zhang, Phys. Rev. B *72*, 014416 (2005).

[65] Xi Chen, S. bedanta, O. Petracic, W. Kleeman, S. Sahoo, and P. P. Freitas, Phys. Rev. B *72*, 214436 (2005).

[66] C. Raj Sankar and P. A. Joy, Phys. Rev. B *72*, 132407 (2005).

[67] A. K. Kundu, P. Nordblad and C. N. R. Rao, Phys. Rev. B *72*, 144423 (2005).

[68] T. Telem-Shafir and Gil Markovich, *Spin-glass Dynamics in Arrays of Strongly Interacting Magnetic Nanocrystals* (Unpublished).

[69] M. Mezard, G. Parisi and M. A. Virasoro, *Spinglass Theory and Beyond* (World Scientific, Singapore, 1987).

[70] C. Dasgupta, Pramana *64*, 679 (2005), in proceedings of the 22nd International Conference on Statistical Physics, edited by S. Dattagupta, H. R. Krishnamurthy, R. Pandit, T. V. Ramakrishnan and D. Sen.

[71] J. M. Luttinger and L. Tisza, Phys. Rev. *70*, 954 (1946).

[72] Amikam Aharoni, Phys. Rev. *177*, 793 (1969).

[73] E. Kneller and E. P. Wohlfarth, J. Appl. Phys. *37*, 4816 (1966).

[74] J. Tejada, X. X. Zhang, and E. M. Chudonovsky, Phys. Rev. B *47*, 14977 (1993).

[75] W. Luo, S. R. Nagel, T. F. Rosenbaum, and R. E. Rosensweig, Phys. Rev. Lett. *67*, 2721 (1991).

[76] H. Mamiya, I. Nakatani, and T. Furubayashi, Phys. Rev. Lett. *82*, 4332 (1999).

[77] P. Jönsson, M. F. Hansen, and P. Nordblad, Phys. Rev. B *61*, 1261 (2000).

[78] C. Luna, M. del P. Morales, C. J. Serna and M. Vazquez, Nanotechnology *14*, 268 (2003).

[79] S. Gangopadhyay, G. C. Hadjipanayis, B. Dale, C. M. Sorensen, K. J. Klabunde, V. Papaefthymiou and A. Kostikas, Phys. Rev. B *45*, 9778 (1992).

[80] A. H. Morrish *Physical Principles of Magnetism* (John Wiley, New York, 1965).

[81] E. H. Frei, S. Shtrikman and D. Treves, Phys. Rev. *106*, 446 (1959).

[82] J. R. Childress, C. L. Chen and M. Natham, appl. Phys. Lett. *56*, 95 (1996).

[83] W. T. Coffey, D. S. F. Crothers, J. L. Dormann, L. J. Geoghegan, and E. C. Kennedy, Phys. Rev. B *58*, 3249 (1998); J. Phys. : Condens. Matter *10*, 9093 (1998).

[84] I. Klik and L. Gunther, J. Stat. Phys. *60*, 473 (1990).

[85] D. A. Garanin, E. C. Kennedy, D. S. F. Crothers, and W. T. Coffey, Phys. Rev. E *60*, 6499 (1999).

[86] W. T. Coffey, D. S. F. Crothers, Yu. P. Kalmykov, and J. T. Waldron, Phys. Rev. B *51*, 15947 (1995).

[87] W. T. Coffey, D. S. F. Crothers, J. L. Dormann, L. J. Geoghegan, Yu. P. Kalmykov, J. T. Waldron, and A. W. Wickstead, Phys. Rev. B *52*, 15951 (1995).

[88] H. B. Braun, Phys. Rev. Lett. *71*, 3557 (1993).

[89] H. B. Braun, Phys. Rev. B *50*, 16485 (1994).

[90] D. Hinzke and U. Nowak, Phys. Rev. B *61*, 6734 (2000).

[91] S. Chakraverty and M. Bandyopadhyay, J. Phys. : Condens. Matter *19*, 216201 (2007).

[92] M. Bandyopadhyay, and S. Dattagupta, Phys. Rev. B *74*, 214410 (2006).

[93] L. Landau and E. Lifshitz, Physik. Zes. Sowjetunion *8*, 153 (1935).

[94] T. L. Gilbert, Phys. Rev. *100*, 1243 (1955).

[95] W. T. Coffey, D. S. F. Crothers, J. L. Dormann, L. J. Geoghegan, E. C. Kennedy, and W. Wernsdorfer, J. Phys. : Condens. Matter *10*, 9093 (1998).

[96] W. H. Meiklejohn, Rev. Mod. Phys. *25*, 302 (1953).

[97] F. E. Luborsky, J. Appl. Phys. *32*, 171S (1961).

[98] R. H. Kodama, J. Magn. Magn. Materials *200*, 359 (1999).

[99] Fred Cooper, Avinash Khare, and Uday Sukhatme *Supersymmetry in Quantum Mechanics* (World Scientific, Singapore 2001).

[100] D. Frenkel and B. Smit, *Understanding Molecular Simulations* (San Diego, CA : Academic, 1996).

[101] M. Bandyopadhyay, S. Dattagupta,and M. Sanyal, Phys. Rev. E *73*, 051108 (2006).

[102] P. Reimann, Phys. Rep. *361*, 57 (2002).

[103] P. S. Landa and P. V. E. McClintock, Phys. Rep. *323*, 1 (2000).

[104] O. M. Braun and Yu. S. Kivshar, Phys. Rep. *306*, 1 (1998).

[105] L. Gammaitoni, P. Hänggi, P. Jung and F. Marchesoni, Rev. Mod. Phys. *70*, 223 (1998).

[106] P. Hänggi and R. Bartussek, Lect. Notes Phys. *476*, 294 (1996); P. Hänggi and R. D. Astumian, Physics Today *55*, 33 (2002); P. Reimann and P. Hänggi, Appl. Phys. A *75*, 169 (2002); H. Linke, Appl. Phys. A *75*, 167 (2002); P. Hänggi, F. Marchesoni and F. Nori, Ann. Phys. (leipzig) *14*, 51 (2005).

[107] C. R. Doering and J. C. Gadoua, Phys. Rev. Lett. *69*, 2318 (1992).

[108] C. Van den Broeck, J. M. R. Parrondo and R. Toral, Phys. Rev. Lett. *73*, 3395 (1994).

[109] C. Van den Broeck, J. M. R. Parrondo, R. Toral and R. Kawai, Phys. Rev. E *55*, 4084 (1997).

[110] A. Barone and G. Paterno, *Physics and applications of the Josephson Effect* (Wiley, NewYork, 1982).

[111] D. Reguera, J. M. Rubi, and A. Perez-Madrid, Phys. Rev. E *62*, 5313 (2000).

[112] P. Fulde, L. Pietronero, W. R. Schneider, and S. Strässler, Phys. Rev. Lett. *35*, 1776 (1975).

[113] W. C. Lindsey, *Synchronization systems in Communication and Control* (Prentice-Hall, Englewood Cliffs, NJ, 1972).

[114] J. W. M. Frenken and J. F. van der Veen, Phys. Rev. Lett. *54*, 134.

[115] A. Ajdari and J. Prost, Proc. Natl. Acad. Sci, U.S.A. *88*, 4468 (1992); G. I. Nixon and G. W. Slater, Phys. Rev. E *53*, 4969 (1996).

[116] P. L. Kapitsa, Zh. Eksp. Teor. Fiz. *21*, 588 (1951).

[117] S. B. Dutta and M. Barma, Phys. Rev. E *67*, 061111 (2003).

[118] S. K. Sarkar and S. Dattagupta, Int. J. Mod. Phys. B *16*, 1247 (2002).

[119] P. Reimann, C. Van den Broeck, H. Linke, P. Hänggi, J. M. Rubi, and A. Perez-Madrid, Phys. Rev. Lett. *87*, 010602 (2001); P. Reimann,C. Van den Broeck, H. Linke, P. Hänggi, J. M. Rubi, and A. Perez-Madrid, Phys. Rev. e *65*, 031104 (2002); Hu Gang, A. Daffertshofer and H. Haken Phys. Rev. Lett. *76*, 4874 (1996).

[120] L. Machura, M. Kostur, P. Talkner, J. Luczka, F. Marchesoni and P. Hänggi, Phys. Rev. E *70*, 061105 (2004); P. Jung, J. G. Kissner and P. Hänggi, Phys. Rev. Lett. *76*, 3436 (1996).

[121] For a review, see P. Hänggi and R. Bartussek, Lect. Notes Phys. *476*, 294 (1996); R. D. Astumain Science *276*, 917 (1997); R. D. Astumian and P. Hänggi, Phys. Today *55(11)*, 33 (2002); P. Reimann and P. Hänggi, Appl. Phys. A: Mater. Sci. Process. *75*, 169 (2002); P. Reimann, Phys. Rep. *361*, 57 (2002); H. Linke, Appl. Phys. A: Mater. Sci. Process. *75*, 167 (2002).

[122] L. D. Landau and E. M. Lifshitz, *Course of Theoretical Physics, Vol. 1* (Pergamon Press, NewYork, 1976).

[123] S. Lifson and J. L. Jackson, J. Chem. Phys. *36*, 2410 (1962).

[124] R. Festa and E. Galleani d'Agliano, Physica A *90*, 229 (1978).

[125] P. Hänggi, P. Talkner, and M. Borkovec, Rev. Mod. Phys. *62*, 251 (1990).

[126] L. Gammaitoni, F. Marchesoni, E. Menichella-Saetta, and S. Santucci, Phys. Rev. Lett. *62*, 349 (1989).

[127] R. Benzi, A. Sutera, and A. Vulpiani, J. Phys. A *14*, 453 (1981).

[128] P. Jung, Phys. Rep. *234*, 175 (1993).

[129] P. Jung, J. G. Kissner and P. Hänggi, Phys. Rev. Lett. *76*, 3436 (1996).

[130] J. L. Mateos, Phys. Rev. Lett. *84*, 258 (2000);J. L. Mateos, Physica A *325*, 92 (2003).

[131] M. Barbi and M. Salerno, Phys. Rev. E *62*, 1988 (2000).

[132] M. Borromeo, G. Costantini, and F. Marchesoni, Phys. Rev. E *65*, 041110 (2002).

[133] H. A. Larrondo, F. Family and C. M. Arizmendi, Physica A *303*, 67 (2002); H. A. Larrondo, F. Family and C. M. Arizmendi, ibid. *320*, 119 (2003).

[134] G. Coupier, M. Saint Jean, and C. Guthmann, Euro. Phys. Lett. *77*, 600012007.

[135] N. Bohr, Dissertation, Copenhegen, 1911; J. H. Van Leeuwen, J. Phys. (Paris) *2*, 361 (1921).

[136] L. Landau, Z. Phys. *64*, 629 (1930).

[137] J. H. Van Vleck, *The Theory of Electric and Magnetic Susceptibilities* (Oxford University Press, London, 1932).

[138] R. Peierls, *Surprises in Theoretical Physics* (Princeton University Press, Princeton, 1979).

[139] S. Datta, *Electronic Transport in Mesoscopic Systems* (Cambridge University Press, 1995).

[140] S. Dattagupta and J. Singh, Physical Review Letters *79*, 961 (1997).

[141] See, for instance, N. Ashcroft, D. Mermin; *Solid State Physics*(Holt, Rinehart and Winston, New York, 1976).

[142] X. L. Li, G. W. Ford and R. F. O'Connell, Phys. Rev. E *53*, 3359 (1996); G. W. Ford, M. Kac, and P. Mazur, J.Math.Phys. (N.Y.) *6*, 504 (1965); G. W. Ford, J. T. Lewis, and R. F. O'Connell, Phys. Rev. A, *37*, 4419 (1988). .

[143] A. O. Caldeira, A. J. Leggett: Ann. Phys. (N.Y.) *149*, 374 (1983).

[144] M. Bandyopadhyay, and S. Dattagupta, J. Stat. Phys. *123*, 1273 (2006).

[145] L. P. Kadanoff, *Statistical Physics - Statics, Dynamics and Renormalization* (World Scientific, Singapore, 2000).

[146] W. Zwerger, Journal of Low Temp. Physics *72*, 291 (1988).

[147] M. Tinkham, *Introduction To Superconductivity* (McGraw-Hill, Singapore, 1996).

[148] D. Dalidovich and P. Philipps, Phys. Rev. Lett. *84*, 737 (2000).

[149] Y. Imry, *Introduction to Mesoscopic Physics* (Oxford University Press, 1977).

[150] R. P. Feynman and F. L. Vernon, Ann. Phys. (N. Y.) *24*, 118 (1963).

[151] C. G. Darwin, Proc. Cambridge Philos. Soc. *27*, 86 (1930).

[152] A. O. Caldeira, A. J. Leggett: Phys. Rev. Lett. *46*, 211 (1981).

[153] L. D. Chang and S. Chakravarty, Phys. Rev. B *31*, 154(1985).

[154] R. P. Feynman: Rev. Mod. Phys. *20*, 367 (1948).

[155] R. P. Feynman, A. R. Hibbs; *Quantum Mechanics and Path Integrals* (Mcgraw-Hill,1965).

[156] H. Kleinert: *Path Integrals in Quantum Mechanics, Statistics , Polymer Physics and Financial Markets* (World Scientific 2004).

[157] U. Weiss: *Quantum Dissipative Systems* (World Scientific 1999).

[158] T. Dittrich, P. Hänggi, G. -L. Ingold, B. Kramer, G. Schön, W. Zwerger *Quantum Transport and Dissipation*, (WILEY-VCH Verlag GmbH,1998).

[159] G. L. Ingold *Springer Lecture Notes in Physics* Vol. 611 (Springer : Berlin, 2002).

[160] H. Grabert, U. Weiss, and P. Talkner, Z. Phys. B *55*, 87 (1984).

[161] F. Reif *Statistical Physics; Berkley Physics Course* Vol. 5 (New York; Mcgraw-Hill, 1965).

[162] S. Dattagupta, S. Puri; *Dissipative Effects in Condensed Matter Physics* (Springer Verlag, Heidelberg, 2004).

[163] See, for instance, G. S. Agarwal, in *Quantum Optics, vol. 70 of Springer - Tracts in Modern Physics*,edited by G. Hohler (Springer Verlag, Berlin, 1974).

[164] H. Grabert, P. Schramm, G. Ingold; Phys. Rep. *168*, 115 (1988).

[165] R. Balian:*From Microphysics to Macrophysics: methods and applications of statistical physics, Vol 1*(Springer-Verlag, 1991)

[166] R. Benguria and M. Kac; Phys. Rev. Lett. *46*, 1 (1981).

[167] A. M. Jayannavar, N. Kumar; J. Phys. A *14*, 1399 (1981).

[168] M. Bandyopadhyay, and S. Dattagupta, J. Phys.: Condens. Matter *18*, 10029 (2006).

[169] A. O. Caldeira and A. J. Leggett, Physica (Amsterdam) *121A*, 587 (1993).

[170] A. J. Leggett, S. Chakravarty, A. T. Dorsey, M. P. A. Fisher, A. Garg and W. Zwerger, Rev. Mod. Phys. *59*, 1 (1987).

[171] See for instance W. H. Zurek, Physics Today, *44*(10), 36 (1991).

[172] G. W. Ford, M. Kac and P. Mazur, J. Math Phys. (N. Y.) *6*, 504 (1965); G. W. Ford, J. T. Lewis and R. F. O'Connell, Phys. Rev. A *37*, 4419 (1988).

[173] X. L. Li, G. W. Ford, R. F. O'Connell, Phys. Rev. A *41*, 5287 (1990); Phys. Rev. A *42*, 4519 (1990); Phys. Rev. E *53*, 3359(1996).

[174] R. Zwanzig, J. Stat. Phys. *1*, 215 (1973).

[175] G. W. Ford, J. T. Lewis and R. F. O'Connell, Phys. Rev. Lett. *55*, 2273 (1985).

[176] B. M. Garraway and K. A. Suominen, Rep. Prog. Phys. *58*, 365 (1995).

[177] H. Grabert and H. Wipf, *Advances in Solid State Physics* (Vieweg, Braunschweig, 1990), Vol. 30.

[178] D. Chandler, *Liquids, Freezing and the Glass Transition*, Les Houches Lectures, edited by D. Levesque et al. (Elsevier Science, Amsterdam, 1991).

[179] R. Egger, H. Grabert, and U. Weiss, Phys. Rev. E *55*, R3809 (1997); See also, S. Dattagupta and S. Puri, *Dissipative Phenomena in Condensed Matter Physics* (Springer-Verlag, Berlin-Heidelberg, 2004).

[180] R. Zwanzig, J. Chem. Phys. *33*, 1338 (1960); R. Zwanzig, in: Lectures in Theoretical Physics (Boulder), Vol. 3, ed. by W. E. Brittin, B. W. Downs, and J. Down (Interscience, New York, 1961)

[181] J. Prigogine and P. Resibois, Physica *27*, 629 (1961).

[182] A. A. Louis and J. P. Sethna, Phys. Rev. Lett. *74*, 1363 (1995).